Estimation of surface currents using optical satellite imagery of Kelvin wakes

Koen Haakman

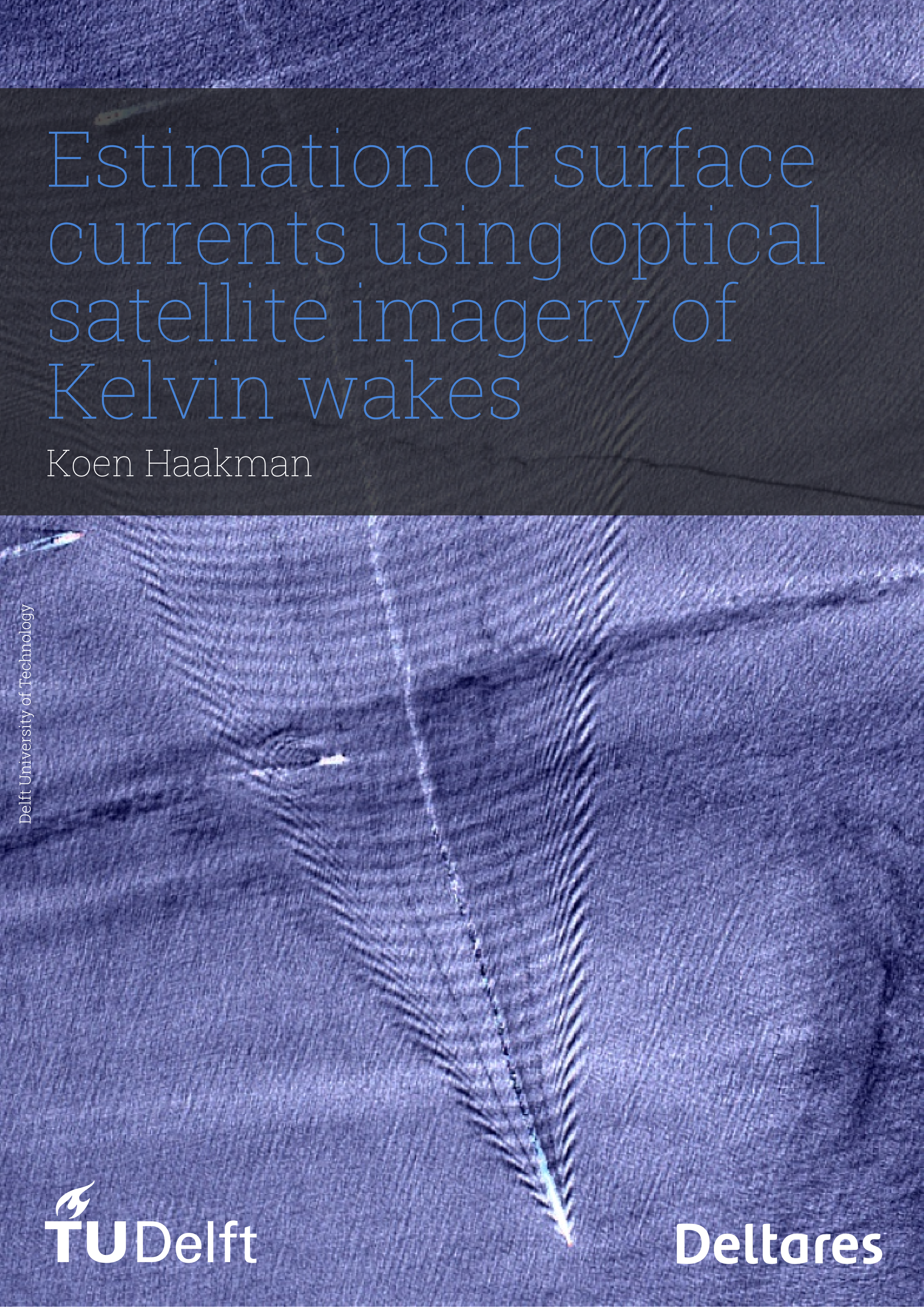

Delft University of Technology

Estimation of surface currents using optical satellite imagery of Kelvin wakes

by

Koen Haakman

Submitted in partial fulfillment of the requirements for a
double degree of Master of Science in

Applied Mathematics

and

Civil Engineering

at the Delft University of Technology,
to be defended publicly on Thursday April 13th, 2023 at 15:00.

Student number:	4467302	
Thesis committee Applied Mathematics:	Prof. dr. ir. M. Verlaan	TU Delft, Deltares, chair
	Dr. ir. D.C. Slobbe	TU Delft
	Prof. dr. ir. M.B. van Gijzen	TU Delft
Thesis committee Civil Engineering:	Dr. ir. D.C. Slobbe	TU Delft, chair
	Prof. dr. ir. M. Verlaan	TU Delft, Deltares
	Dr. M.A. Eleveld	TU Delft, Deltares
	Ir. A.J. van der Hout	TU Delft, Deltares
	A. Gerritsma, MSc	TU Delft

Cover: Modified Sentinel-2B image of a Kelvin wake in the Strait of Gibraltar under CC BY-SA 3.0 IGO

Preface

This thesis concludes my double degree in Applied Mathematics and Civil Engineering at TU Delft. During my bachelor's degree in Civil Engineering, I came to appreciate how a wide range of engineering problems could be reduced to similar mathematical models. This sparked my interest to study mathematical modelling in more detail.

Simultaneously, I got introduced to the field of Remote Sensing, in which information about the Earth is gathered from satellite data. I quickly developed a passion for this discipline, particularly in its applications to oceanography. Given the opportunity to specialize in Geoscience and Remote Sensing within the Civil Engineering master's program, pursuing a double degree in both Applied Mathematics and Civil Engineering felt like a natural choice.

The topic of this thesis has allowed me to combine the skills obtained during both programs. The relationship with the Applied Mathematics program is most clear in the first two chapters. First, a mathematical model for the propagation of ship waves is presented. Thereafter, I developed an algorithm to fit this model to satellite imagery. Though, my mathematical inclination has also influenced subsequent chapters. The connection with remote sensing is clear throughout the thesis, though it is most notable in chapter 4, where the developed algorithm is applied to real satellite imagery.

I would like to express my deep gratitude to my daily advisor, Martin Verlaan, whose guidance and support have been invaluable throughout this process. I want to thank Martin and Avelon for our weekly meetings, which kept me going even during challenging times. I am also grateful to Arne, Cornelis and Marieke, who provided feedback and guidance on this work. Furthermore, I extend my thanks to Martin van Gijzen for taking the time to join the assessment committee. Finally, I would like to thank Deltares for supporting this research as part of the Enabling Technologies program.

Koen Haakman
Hoofddorp, April 2023

Summary

Ocean currents play a crucial role in many scientific and industrial applications. Contemporary measurement techniques are limited in spatial coverage or spatial resolution. The goal of this thesis is to develop a new algorithm to measure sea surface currents. The proposed measurement principle relies on the fact that for a ship, the ship speed can be defined relative to land or water. By subtracting the two ship speed vectors, the surface current is estimated along and across the ship track. The ship speed relative to land is determined using GNSS-based data from the Automatic Identification System (AIS). The ship speed relative to water can be determined using optical satellite imagery of ship-induced wave patterns, which are called Kelvin wakes.

From linear wave theory, it is shown that the spectral signal of a Kelvin wake is controlled by three variables. The radial location of the signal in a two-dimensional spectrum is determined by the ship speed through water. The orientation of the signal in the spectrum is determined by the course of the ship through water, while the energy distribution along the spectral signal is determined by the ship hull geometry. The ship speed through water and ship course through water are recovered by applying a generalized Radon transform to the Kelvin wake spectrum.

Surface currents were computed for 97 Kelvin wakes taken from Sentinel-2 imagery in two study areas: the North Sea/Kattegat Strait and the Strait of Gibraltar. In the North Sea study area, estimated currents were compared to modelled currents from the Dutch Continental Shelf Model (DCSM). Linear fits between the two data sets explained 82 and 64% of the variance for the along- and across-ship surface currents, respectively. In the Gibraltar study area, estimated currents were validated with modelled currents from the Copernicus Marine Environmental Monitoring Service (CMEMS) and currents derived from High-Frequency Radars (HFRs). With respect to the HFR observations, linear fits explained 95 and 76% of the variance for the along- and across-ship surface currents, respectively.

Standard deviations were estimated for the surface currents using two methods. First, the errors in the two ship speed vectors were estimated individually and then propagated into the surface currents. However, the resulting uncertainties were not correlated with observed errors for the along-ship surface currents. Although the estimated uncertainties for the across-ship surface currents showed some correlation with observed errors, they were still limited. Therefore, the developed error estimation algorithm is currently not sufficiently accurate to be utilized for quality control of individual measurements.

Second, standard deviations were also estimated using a statistical technique called Triple Collocation (TC). In TC, three data sets of the same quantity collocated in space and time are compared to estimate the uncertainty per data set. In the Gibraltar study area, estimated along-ship surface currents ranged from -2.1 to $2.2\,\mathrm{m\,s^{-1}}$, with an estimated standard deviation of $0.14\,\mathrm{m\,s^{-1}}$. The estimated across-ship surface currents ranged from -1.6 to $2.1\,\mathrm{m\,s^{-1}}$, with an associated standard deviation of $0.30\,\mathrm{m\,s^{-1}}$. It was shown that the inferior accuracy of the across-ship surface currents could largely be explained by an increased sensitivity of this component to small variations in ship course. By filtering out data points with the most variation in ship course, the estimated uncertainty in the across-ship currents decreased to $0.16\,\mathrm{m\,s^{-1}}$.

To gain insight into the applicability of the developed algorithm, a specular reflection model was used to show that reflectance patterns could be reconstructed using the viewing geometry between the sun, imaging platform and sea surface. However, this model was not able to predict for an individual ship if its Kelvin wake would be visible on satellite imagery. Therefore, more research is needed to study the influence of ship geometry, oceanic and atmospheric conditions on Kelvin wake visibility.

By taking vessel density and cloud cover data into account, it has been estimated that $120\,000$ data points could be acquired annually if the algorithm would process all Sentinel-2 imagery over European open waters. This number is on the same order of magnitude as the number of current measurements obtained by Argo floats each year. Moreover, the measurement frequency could be increased by using data from other high-resolution optical satellite missions. Since cloud cover is a limitation of optical satellite imagery, it would be interesting to investigate the applicability of the algorithm to Synthetic Aperture Radar imagery. A better understanding of the spatiotemporal distribution of measurements is required to appreciate potential areas of application.

Contents

Nomenclature

Abbreviations

Abbreviation	Definition
AIS	Automatic Identification System
CMEMS	Copernicus Marine Environmental Monitoring Service
COG	Course Over Ground
CTW	Course Through Water
DCSM	Dutch Continental Shelf Model
DFT	Discrete Fourier Transform
GNSS	Global Navigation Satellite System
GRT	Generalized Radon Transform
HFR	High-Frequency Radar
MAD	Median Absolute Deviation
RMSE	Root-Mean-Square Error
S2	Sentinel-2
SAR	Synthetic Aperture Radar
SD	Standard Deviation
SOG	Speed Over Ground
STW	Speed Through Water
TC	Triple Collocation

Symbols

Symbol	Definition	Unit
$\mathscr{F}$	Fourier transform	
Fr	Hull Froude number, $Fr = V/\sqrt{gL}$	[-]
g	Gravitational acceleration	[m/s^2]
h	Local water depth	[m]
H	Hessian matrix	
I	Fisher information	
J	Jacobian matrix	
k_x	wavenumber in x-direction	[rad/m]
k_y	wavenumber in y-direction	[rad/m]
k	Magnitude of wavenumber, $k = \sqrt{k_x^2 + k_y^2}$	[rad/m]
K	Nondimensionalized wavenumber, $K = kL$	[-]
L	Characteristic length scale	[m]
l	Likelihood function	
n	Refractive index	[-]
N	Sample size	[-]
p	Pressure	[N/m^2]
$\hat{p}$	Fourier transformed pressure	[N]
$\hat{P}$	Nondimensionalized Fourier transformed pressure	[-]
$\mathscr{R}$	Generalized Radon transform	
R	Reflectance	[-]
S	Spectrum	[dB]
U_{along}	Current component parallel to sailing line	[m/s]
U_{across}	Current component perpendicular to sailing line	[m/s]
V_{SOG}	Ship speed over ground	[m/s]
V_{STW}	Ship speed through water	[m/s]
W	Wind speed	[m/s]
ζ	Nondimensionalized free surface elevation, $\zeta = \eta/\text{L}$	[-]
η	Free surface elevation	[m]
θ	Polar angle	[rad]
θ_{COG}	Ship course over ground	[rad]
θ_{CTW}	Ship course through water	[rad]
θ_n	Zenith angle of surface normal	[rad]
θ_r	Receiver zenith angle	[rad]
θ_s	Source zenith angle	[rad]
ρ	Density	[kg/m^3]
σ	Standard deviation	
Σ	Covariance matrix	
ϕ	Velocity potential	[m^2/s]
ϕ_r	Receiver azimuth angle	[rad]
ϕ_s	Source azimuth angle	[rad]
ω	Radial frequency	[rad/s^1]

1

Introduction

1.1. Motivation

Ocean currents are important for many scientific and industrial applications. They influence weather and climate, water levels, transport of energy, sediment and pollutants, shipping routes and fish distribution, among others. Therefore, measurements of ocean currents are crucial to their understanding. Currently, there exist several techniques to measure ocean currents.

First, there are in-situ measurements with current meters at a fixed location or buoy. Such instruments require maintenance and are expensive, especially when a large number of them is required. Currents can also be measured by tracking the position of so-called drifters or chemical tracers over time. Currently, there are several thousand drifters in operation worldwide [24]. Although these devices provide excellent temporal resolution, their number is too few to provide good spatial resolution.

Another technique to measure ocean currents is by using radar systems. A radar can transmit electromagnetic waves towards the sea surface. Some part of this signal will be scattered back to the radar through a mechanism called Bragg scattering [31]. The Doppler shift in this return signal is a measure of the surface current in the line of sight from the sea surface to the radar. By measuring line-of-sight surface currents from multiple radars, total surface currents may be reconstructed. Although this technique provides good spatial and temporal resolution, radars are expensive and their spatial coverage is limited to coastal areas.

Next, there are also several satellite-based techniques to measure ocean currents. In [24] four remote sensing techniques are highlighted. First, infrared imagery can be used to derive sea surface temperature fields. Since currents transfer heat, the sea surface temperature fields also reveal information about flow patterns such as the Gulf Stream. This method is hindered by the presence of cloud cover and is limited to large spatial scales.

Second, oceanographic features such as chlorophyll or sediment plumes can be tracked over successive satellite images to estimate currents. Unless the features are tracked using radar imagery, also here cloud cover is a limitation. Moreover, in [24] it is stated that "*There is a need to improve ocean feature detection and tracking techniques and to develop more reliable operational procedures*.".

The third technique is by measuring line-of-sight currents from Synthetic Aperture Radars (SAR). This works by measuring the Doppler shift introduced by the relative motion between the satellite platform and the sea surface and relating it to the line-of-sight sea surface current. Ideally, multiple satellite platforms would receive the backscattered radio waves to measure line-of-sight currents in multiple directions. This would allow the reconstruction of the total surface currents. This is one of the goals of the Harmony mission [30], which will be launched in 2029 at the earliest.

Finally, the last technique covered in [24] is the measurement of geostrophic currents from satellite altimetry. Geostrophic currents are currents arising from a balance between pressure gradients and the Coriolis effect. However, this methodology breaks down when currents are not geostrophic and in coastal regions where backscattering from land contaminates the signal. Therefore, it can be concluded that although there exist several promising remote sensing techniques, their application is still usually limited to specific cases or large spatial scales.

Recently, data from the Automatic Identification System (AIS) has also been exploited to estimate surface currents [25, 6, 51]. The AIS is a maritime collision-avoidance system in which ships transmit their position, speed over ground, course over ground and true heading. In [25] it is shown that surface currents can be estimated by aggregating data from multiple ships within a spatiotemporal interval. A validation with respect to currents measured by drifting buoys yields root-mean-square errors on the order of $0.3\,\mathrm{m\,s^{-1}}$. A limitation of their method is the fact that the ship speed through water is not broadcast through AIS. This introduces the need to combine data from multiple ships while assuming that the flow field is homogeneous within a spatiotemporal interval. This reduces the temporal and spatial resolution, depending on ship density.

In order to be able to estimate the surface current for an individual ship, the ship's speed through water needs to be known. It turns out that this variable is related to the ship-induced wave pattern behind a ship. Background information considering this wave pattern is given in the next section.

1.2. Background Kelvin ship wakes

Under the assumption that a ship can be represented by a point source moving at a uniform speed, Lord Kelvin investigated the resulting wave pattern. He concluded that the resulting V-shaped wake, now called the Kelvin wake, should be contained within an angle of 19.47° with respect to either side of the sailing line, regardless of the ship speed [46]. Furthermore, he reasoned that the waves in the wake pattern travel with the ship speed, which causes their wavelengths to depend solely on the ship speed [46]. Further research has shown that these wakes consist of two types of waves: transverse and divergent waves (see Figure 1.1a) [12]. The transverse waves propagate along the sailing line while the divergent waves travel away from the sailing line. Along the boundary of this wave system, the transverse and divergent waves interfere to form so-called cusp waves [36] [27]. Typically, these cusp waves are the most visible feature on imagery (e.g. Figure 1.1b).

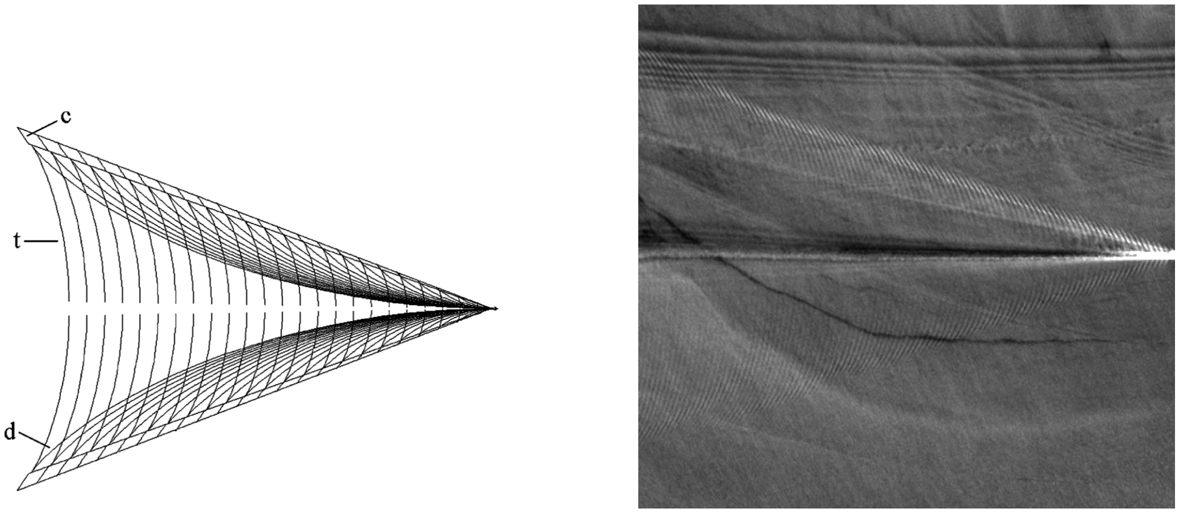

(a) Schematic of theoretical shape of a Kelvin wake. The letters *t*, *d* and *c* denote the transverse, divergent and cusp waves respectively. Figure taken from [54].

(b) Sentinel-2 image of a Kelvin wake behind a ship.

Figure 1.1: Theoretical and observed Kelvin wake.

The simplification of a ship by a point source is quite substantial. It is then no surprise that in practice, the wake angle has been observed to differ from the classical 19.47° predicted by Kelvin. In fact, it turns out that the wake angle reduces with increasing hull Froude number [37] [13]. However, Kelvin's second conclusion, that the wavelengths in the wave pattern are uniquely determined by the ship speed seems to be more accurate. This relationship has been exploited to determine ship speeds from air- and spaceborne Synthetic Aperture Radar images of ship waves.

In [54] ship speeds were estimated by taking one-dimensional Fourier transforms of the image intensity along the cusp waves in airborne SAR imagery. Subsequently, the peak wavenumber in the resulting periodogram was related to the ship speed. The accuracies ranged from 3 to 10%. The main limitation of their methodology is that the Fourier transform was only taken along the cusp lines instead of taking the full two-dimensional wave pattern into account.

A different method to retrieve ship speeds from three spaceborne SAR images was used in [47]. They used the fact that moving objects are displaced in the azimuth-direction on SAR imagery. Therefore, the ship and its Kelvin wake are not connected on a SAR image. The azimuth offset between the ship and the vertex of the cusp lines is a measure of the ship speed. The accuracy of the estimated ship speeds was within 15%.

In [19] ship speeds were estimated from 33 SAR images of ship wakes using both methods described above. Both methods produced ship speeds that showed agreement within 14%, however there was no validation with independent ship speed data. In [20] the same two methods were applied again and results were validated with respect to data from the Automatic Identification System (AIS). Relative ship speed errors were found to be within 12%.

With a typical ship speed of $10\,\mathrm{m\,s^{-1}}$, errors from 3-12% are already between 0.3 and $1.2\,\mathrm{m\,s^{-1}}$. Hence, the errors are relatively large with respect to the order of magnitude of surface currents. Therefore, it appears that the existing methods do not measure ship speeds with sufficient accuracy to estimate surface currents. However, in all studies, SAR imagery was used. Since SAR images contain more noise than optical imagery, estimation may have been less reliable.

The full two-dimensional spectrum of a Kelvin wake was analyzed in [18] [45]. In [27] 32 optical satellite images were analyzed to count the number of visible Kelvin wakes. A probability of Kelvin wake visibility of about 25% was found, depending on satellite resolution and ship type. In [29] and [42] a simple reflectance model is used to study the appearance of Kelvin wakes on optical satellite imagery. Finally, there is a significant amount of literature on ship detection for marine surveillance by looking for Kelvin wakes (e.g. [39], [9]). A thorough search of the relevant literature returned no papers covering the estimation of surface currents using either optical or radar imagery of Kelvin ship wakes. In the next section, the new concept to measure surface currents through Kelvin wake imagery is presented.

1.3. Measurement principle

In this section, the new measurement principle for estimation of surface currents is presented. The measurement principle relies on the fact that the movement of a ship can be described by two different ship speed vectors. First, the speed of the ship can be described relative to land. The corresponding magnitude and direction are called the Speed Over Ground (SOG) and Course Over Ground (COG) respectively. Second, the vessel movement can also be represented with respect to the surrounding water. The corresponding magnitude and direction are now given by the Speed Through Water (STW) and Course Through Water (CTW) respectively. In Figure 1.2 the vectors are visualized.

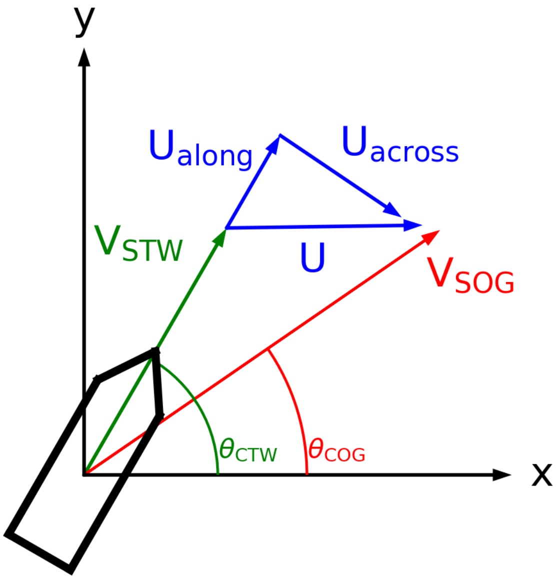

Figure 1.2: Geometrical relation between the ship speed vectors and the surface current components.

In the presence of a current, the two ship speed vectors will not coincide. The difference between the two vectors will be the current vector. Independent estimation of the two ship speed vectors will thus allow estimation of the underlying current. From Figure 1.2, an equation for each component of the current can be derived:

$$U_{\text{along}} = V_{\text{SOG}} \cos\left(\theta_{\text{CTW}} - \theta_{\text{COG}}\right) - V_{\text{STW}}, \tag{1.1}$$

$$U_{\text{across}} = V_{\text{SOG}} \sin\left(\theta_{\text{CTW}} - \theta_{\text{COG}}\right). \tag{1.2}$$

It should be noted that currents act on a ship over its entire draft. Hence, the estimated currents are related to the average current along the ship draft. Therefore, the representative depth of the surface currents is likely several meters below the surface and will vary from ship to ship. Hereafter, it will be assumed that the estimated currents are representative of the conditions at the surface. Therefore, the currents derived from Equations 1.1 and 1.2 will be referred to as surface currents.
Equations 1.1 and 1.2 contain four unknowns. V_{SOG} and θ_{COG} are variables that are transmitted through the Automatic Identification System (AIS). The AIS is primarily a collision-avoidance system based on satellite navigation. More information on the AIS is given in Section 4.1.2.
Now, only two unknowns remain. The ship course through water could be approximated using the True Heading, which is the direction that the ship is pointing to. This variable is also contained in the AIS data, however it is also influenced by crosswinds. Alternatively, the orientation of a ship's Kelvin wake can be considered. The Kelvin wake follows the course through water of a ship and is expected to be less influenced by crosswinds on the ship. The orientation can be estimated from optical imagery.
Finally, V_{STW} is related to the wavelengths in the ship's Kelvin wake. The faster the ship sails, the longer the waves in the Kelvin wake. In Section 2.2 the governing relationship is derived. The derivation is a consequence of the linear dispersion relation for surface gravity waves, which is first derived in Section 2.1.

1.4. Research question

The main goal of this thesis is to examine to what extent the measurement principle from the previous section can actually be used to estimate surface currents. This leads to the following main research question:

- Is it possible to estimate sea surface currents by combining optical satellite imagery of Kelvin wakes with data from the Automatic Identification System?

In order to answer this research question, some theory concerning ocean waves is presented in Chapter 2. There, a model for the two-dimensional Fourier transform of a Kelvin wake will be derived. Moreover, it will be shown that the spectral shape of the Kelvin wake is not sensitive to the geometry of the ship hull. Thereafter, an algorithm to match an observed spectral Kelvin wake signal to the theoretical model will be developed in Chapter 3. Using this algorithm, surface currents will be estimated from Sentinel-2 imagery in Chapter 4. The estimated currents will be compared to independent datasets of modelled and observed currents to validate the measurement principle, which allows the main research question to be answered.

From a favorable answer to the main research question naturally yields a follow-up question, i.e., how accurate are the estimated surface currents? To answer this question, an error analysis is conducted in Chapter 5. First, two potential sources of modelling error will be studied. Thereafter, two different statistical approaches are undertaken to estimate the uncertainty in the surface currents.

Subsequently, it is interesting to study how applicable the proposed measurement concept is. To that end, in Chapter 6 it will be studied to what extent the viewing geometry and ship direction determine whether a Kelvin wake will be visible on optical satellite imagery. Finally, the expected number of data points that the measurement principle could yield in a given year is estimated in Chapter 7. Concluding remarks are given in Chapter 8.

2

Modelling

In this chapter, the models used throughout the remainder of this thesis are derived. In Section 2.1, it is shown how the linear dispersion relation for surface gravity waves can be derived. This dispersion relation is the starting point for the derivation of a model for the spectral shape of a Kelvin wake, which is derived in Section 2.2. This spectral model is used to retrieve one of the ship speed vectors from optical imagery, using the algorithm presented in Chapter 3. Finally, in Section 2.3 a model for the surface elevations in a Kelvin wake is derived. This model is used to study the influence of the Froude number and hull geometry on the spectrum of a Kelvin wake. Moreover, in Chapter 6, this model is used to study the influence of the viewing geometry on the reflectance of a Kelvin wake.

2.1. Linear wave theory

The goal of this section is to derive the linear dispersion relation for surface gravity waves, which will be used in Section 2.2 to derive a model for the spectral shape of a Kelvin wake. To that end, the basics from linear wave theory are presented. The derivation here follows [23]. The following assumptions are made:

- The fluid is incompressible, inviscid and irrotational.
- Surface tension effects are negligible.
- Wave amplitudes are small with respect to the wavelength.

The principle of conservation of mass leads to the continuity equation:

$$\frac{\partial \rho}{\partial t} + \nabla \cdot (\rho u) = 0, \tag{2.1}$$

where ρ is the fluid density and $u = (u_x, u_y, u_z)^T$ represents the velocity vector. The fluid density is constant in case of incompressible flow, hence $\frac{\partial \rho}{\partial t} = 0$. Furthermore, ρ can be factored out of the divergence term. Hence, the continuity equation reduces to

$$\nabla \cdot u = 0. \tag{2.2}$$

Moreover, a curl-free vector field can be represented by the gradient of a scalar function. Let $u = \nabla \phi$, where ϕ is called the velocity potential. Substitution of the velocity potential into Equation 2.2 yields

$$\nabla^2 \phi = 0. \tag{2.3}$$

Hence, the flow problem is reduced to the Laplace equation. Three boundary conditions will be imposed in order to provide a well-posed problem. The first two are of kinematic nature, i.e., they relate to motion of the fluid. The last boundary condition is dynamic, which means that it is related to forces acting on the fluid. First, it is assumed that water particles do not cross the air-sea interface. To that end, the speed of a water particle normal to the surface of the water is required to be equal to the speed of the fluid surface in that direction. After linearization, this leads to

$$u_z = \frac{\partial \eta}{\partial t} \qquad \text{at } z = 0, \tag{2.4}$$

where $\eta = \eta(x, y, t)$ denotes the free surface elevation. The second boundary condition states that no fluid is flowing through the bottom. This yields

$$u_z = 0 \qquad \text{at } z = -h, \tag{2.5}$$

where h is the water depth. The dynamic boundary condition results from the assumption that the waves are not forced by atmospheric pressure, i.e., it is assumed that atmospheric pressure is constant. Without loss of generality, the pressure can be set to 0 at the free surface. Hence, the dynamic boundary condition reads

$$p = 0 \qquad \text{at } z = 0. \tag{2.6}$$

The three boundary conditions are now transformed into a form which expresses them in terms of the velocity potential. For the kinematic boundary conditions, substitution of $u = \nabla\phi$ directly leads to

$$\frac{\partial \phi}{\partial z} = \frac{\partial \eta}{\partial t}, \qquad \text{at } z = 0, \tag{2.7}$$

$$\frac{\partial \phi}{\partial z} = 0 \qquad \text{at } z = -h. \tag{2.8}$$

The transformation of the dynamic boundary condition follows from conservation of momentum. For an inviscid fluid, the linearized momentum equations are:

$$\frac{\partial u_x}{\partial t} = -\frac{1}{\rho}\frac{\partial p}{\partial x}, \tag{2.9}$$

$$\frac{\partial u_y}{\partial t} = -\frac{1}{\rho}\frac{\partial p}{\partial y}, \tag{2.10}$$

$$\frac{\partial u_z}{\partial t} = -\frac{1}{\rho}\frac{\partial p}{\partial z} - g, \tag{2.11}$$

where g is the gravitational constant. Substitution of the velocity potential, changing the order of differentiation and reordering yields

$$\frac{\partial}{\partial x}\left(\frac{\partial \phi}{\partial t} + \frac{p}{\rho}\right) = 0, \tag{2.12}$$

$$\frac{\partial}{\partial y}\left(\frac{\partial \phi}{\partial t} + \frac{p}{\rho}\right) = 0, \tag{2.13}$$

$$\frac{\partial}{\partial z}\left(\frac{\partial \phi}{\partial t} + \frac{p}{\rho} + gz\right) = 0. \tag{2.14}$$

The expression $\frac{\partial \phi}{\partial t} + \frac{p}{\rho} + gz$ is invariant with respect to x, y and z. It can therefore only be a function of time, i.e., $\frac{\partial \phi}{\partial t} + \frac{p}{\rho} + gz = f(t)$. Since the velocity potential is non-unique, it can be redefined to incorporate $f(t)$. Then, the linearized Bernoulli equation for unsteady flow remains:

$$\frac{\partial \phi}{\partial t} + \frac{p}{\rho} + gz = 0. \tag{2.15}$$

Evaluation of Equation 2.15 at the free surface $z = \eta$, along with the dynamic boundary condition $p = 0$ yields the transformed dynamic boundary condition:

$$\frac{\partial \phi}{\partial t} + g\eta = 0 \qquad \text{at } z = 0. \tag{2.16}$$

Now, the two boundary conditions at the free surface can be combined to eliminate the surface elevation as an unknown function from the boundary value problem. Temporal differentiation of Equation 2.16 and substitution of the kinematic free surface condition $\frac{\partial \phi}{\partial z} = \frac{\partial \eta}{\partial t}$ yields

$$\frac{\partial^2 \phi}{\partial t^2} + g\frac{\partial \phi}{\partial z} = 0 \qquad \text{at } z = 0. \tag{2.17}$$

Hence, linear wave theory leads to the following boundary value problem:

$$\nabla^2\phi = 0, \tag{2.18}$$

$$\frac{\partial\phi}{\partial z} = 0 \qquad \text{at } z = -h, \tag{2.19}$$

$$\frac{\partial^2\phi}{\partial t^2} + g\frac{\partial\phi}{\partial z} = 0 \qquad \text{at } z = 0. \tag{2.20}$$

An analytical solution to the above problem is given by a harmonic wave propagating in the positive x-direction

$$\eta(x, y, t) = a\,\mathsf{sin}(\omega t - kx), \tag{2.21}$$

where a is the wave amplitude, $\omega = 2\pi/T$ is the angular frequency corresponding to a wave period T and $k = 2\pi/L$ is the wavenumber, or spatial frequency, corresponding to wavelength L. The corresponding velocity potential is given by

$$\phi = \frac{\omega a}{k}\frac{\mathsf{cosh}[k(h+z)]}{\mathsf{sinh}(kh)}\mathsf{cos}(\omega t - kx). \tag{2.22}$$

Substitution of Equations 2.21 and 2.22 into the dynamic boundary condition Equation 2.16 leads to the linear dispersion relation:

$$-\frac{\omega^2 a}{k}\frac{\mathsf{cosh}(kh)}{\mathsf{sinh}(kh)}\mathsf{sin}(\omega t - kx) + ga\,\mathsf{sin}(\omega t - kx) = 0, \tag{2.23}$$

$$\left(ga - \frac{\omega^2 a}{k}\mathsf{coth}(kh)\right)\mathsf{sin}(\omega t - kx) = 0, \tag{2.24}$$

$$ga - \frac{\omega^2 a}{k}\mathsf{coth}(kh) = 0, \tag{2.25}$$

$$\omega^2 = gk\,\mathsf{tanh}(kh). \tag{2.26}$$

The dispersion relation associates a wavenumber k with an angular frequency ω. It can be interpreted as the connection between spatial and temporal frequency. In the next section, the dispersion relation will be used to derive a forward model for the spectral shape of a Kelvin wake.

2.2. Derivation spectral model Kelvin wake

In this section, a model that relates a ship's Speed Through Water (STW) to the wavelengths in its Kelvin wake will be derived. To that end, the following assumptions are made:

- The ship is sailing with constant speed V_{STW} in the positive x-direction.
- The Kelvin wake is stationary with respect to the moving ship.
- Linear wave theory is appropriate for describing the propagation of the Kelvin waves.

Uncertainties introduced by violation of the first assumption are part of the uncertainty quantification in Section 5.2.2. Furthermore, in Section 5.1.2 the model presented here will be extended to include nonlinear effects due to wave steepness. The derivation in this section is based on [18]. Assuming linear wave theory, the dispersion relation for surface gravity waves is given by

$$\omega^2 = gk \tanh(kh), \tag{2.27}$$

Now suppose that the reference frame is fixed to the ship, with the x-axis aligning with the sailing line. Then, the reference frame moves with a constant speed V_{STW}. This introduces a Doppler shift which yields an apparent frequency in the moving frame of reference given by (see Section A)

$$\omega' = \omega - V_{\text{STW}} k_x, \tag{2.28}$$

where ω' is the apparent angular frequency in the moving frame of reference. Substitution of Equation 2.28 into Equation 2.27 gives

$$(\omega' + V_{\text{STW}} k_x)^2 = gk \tanh(kh). \tag{2.29}$$

Since the Kelvin waves are assumed to be stationary with respect to the ship, $\omega' = 0$. Hence, the above equation reduces to

$$V_{\text{STW}} = \pm \frac{\sqrt{gk \tanh(kh)}}{k_x}. \tag{2.30}$$

As the Kelvin waves are travelling in the same direction as the ship, the negative solution can be ignored. The above equation indicates that a ship's speed through water depends only on the local water depth and the wavelengths in the Kelvin wake. However, often the wavelengths in the Kelvin wake are small with respect to the water depth. In particular, often it is the case that $h \geq \frac{\lambda}{2}$, hence $kh = 2\pi \frac{h}{\lambda} \geq \pi$. Since $\tanh(x) \approx 1$ for $x \geq \pi$, $\tanh(kh) \approx 1$. In that case, Equation 2.30 reduces to

$$V_{\text{STW}} = \frac{\sqrt{gk}}{k_x}. \tag{2.31}$$

Hence, in this deep-water regime, a ship's speed through water depends only on the wavenumbers in the Kelvin wave pattern. Section 5.1.1 covers the case where the deep-water approximation is not strictly applicable. The above equation can also be reordered such that $k_y = f(k_x; V_{\text{STW}})$. This gives

$$k_y = \pm k_x \sqrt{\frac{V_{\text{STW}}^4}{g^2} k_x^2 - 1}. \tag{2.32}$$

The above formulation is useful for visualizing the Kelvin wave pattern in the spectral domain and will be used to fit the model to observed data. In Figure 2.1 the model is plotted for three different values of a ship's STW. The origin corresponds to zero wavenumbers, i.e., infinitely long waves. By moving away from the origin radially, the wavelength decreases.

Consider the solid black line corresponding to a ship moving at 10 m/s through the water. Each point on this curve corresponds to a direction in which the Kelvin waves could propagate. Hence, the interpretation of the curve is that it gives the wavenumbers that a wave in a particular direction needs to have to stay stationary with respect to the ship. It can be seen that the waves travelling in the same direction as the ship (along positive x-axis), will have the smallest wavenumber, i.e., longest wavelength. As the angle with respect to the sailing line increases, the wavelengths of the Kelvin waves decrease.

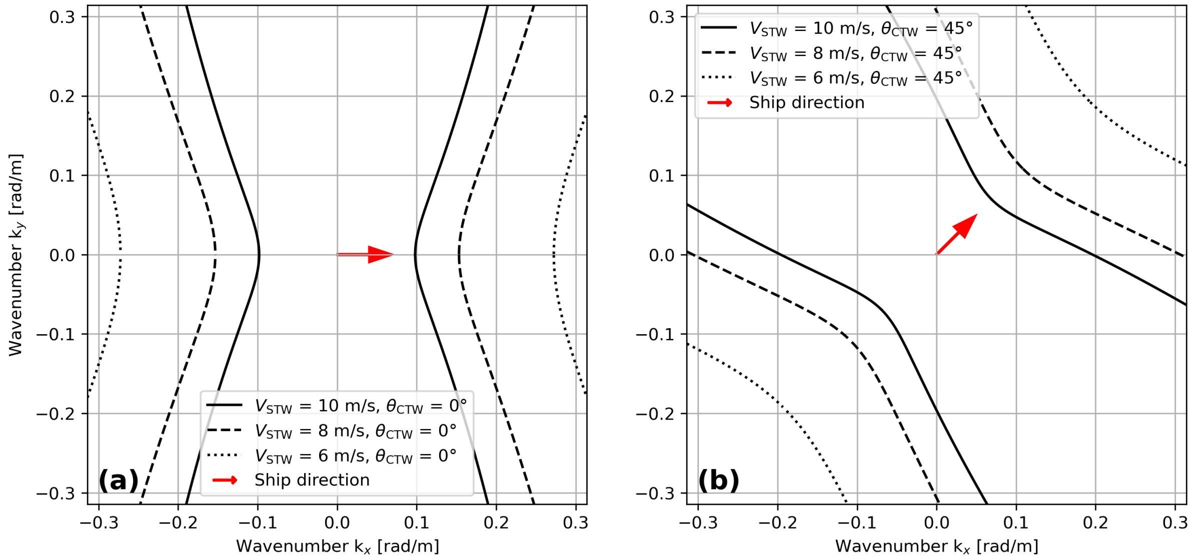

Figure 2.1: a) Theoretical shape of the Kelvin wave patterns in the spectral domain if the deep-water approximation is applicable. The dotted, dashed and solid lines correspond to a ship Speed Through Water (STW) of 6, 8 and 10 m/s respectively. Ship is assumed to be moving in positive x-direction, as indicated by the red arrow. b) As in a), but now for a ship with a heading of 45° counter-clockwise with respect to the positive x-axis.

So far, only the case that a ship is sailing along the positive x-axis has been considered. However, when this is not the case, the curves can simply be rotated numerically by the direction that the ship is moving in. Figure 2.1b shows the model for a ship with a heading of 45° with respect to the positive x-axis.

2.2.1. Lower bound ship speed through water

In Figure 2.1 it can be seen that as the ship speed decreases, the model moves radially outward. At some point, the model is no longer visible on the spectrum. The boundaries of the spectrum are chosen such that they correspond to the maximum wavenumber distinguishable on Sentinel-2 imagery. By the Nyquist criterion, a wave needs to be sampled with at least 2 samples per wavelength in order to be reconstructed. For an image, this comes down to having at least two pixels per wavelength. In the case of Sentinel-2 imagery, with a ground sampling distance of $10\,\mathrm{m}$, the wavelengths must be at least $20\,\mathrm{m}$. This gives a wavenumber of $2\pi/20 \approx 0.314\,\mathrm{rad/m}$.

The last part of the Kelvin wake that remains in the spectrum corresponds to its smallest wavenumber, thus, its largest wavelength. From Equation 2.31 an equation for the longest wavelength present in the Kelvin wake can be derived. The longest waves are found along the sailing line, hence they have $k_y = 0$. This gives $k = k_x$, such that Equation 2.31 reduces to

$$V_{\text{STW}} = \sqrt{\frac{g}{k_x}}. \tag{2.33}$$

Reordering the above equation gives

$$L_{\text{max}} = 2\pi \frac{V_{\text{STW}}^2}{g}, \tag{2.34}$$

where L_{max} denotes the longest wavelength present in the Kelvin wake. In Figure 2.2 this relationship between V_{STW} and the longest wavelength in the Kelvin wake is shown. By substituting $L_{\text{max}} = 20\,\mathrm{m}$, it can be shown that the minimum STW required for detection on Sentinel-2 imagery is about $5.6\,\mathrm{ms}^{-1}$. However, since the waves in the rest of the Kelvin wake are even shorter, the ship speed should be slightly larger in practice. It has been observed that a ship speed through water of about $6\,\mathrm{ms}^{-1}$ suffices. For higher resolution satellite imagery, such as WorldView or SPOT, a lower ship speed will be sufficient.

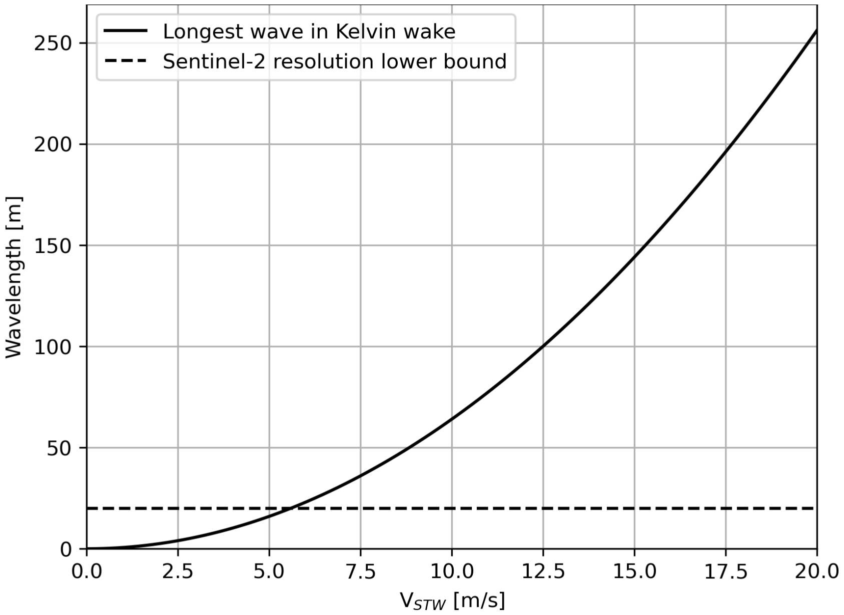

Figure 2.2: Longest wavelength in the Kelvin wake as a function of the ship Speed Through Water (STW) (Equation 2.34).

2.3. Derivation spatial model Kelvin wake

In this section, an analytical model for the surface elevation pattern in a Kelvin wake is derived. This model is used to reveal the influence of the Froude number on the spectrum of a Kelvin wake. Moreover, in Chapter 6, a reflectance model is used to study the influence of the viewing geometry on the visibility of a Kelvin wake on satellite imagery. The basis for this reflectance model is provided by the spatial Kelvin wake model presented here.

The Kelvin wake model is originally presented in [13]. Part of the derivation here follows [38]. Classical linear wave theory is adjusted to include an external source term which represents a ship. Let $p_{\text{ext}}(x, y, t)$ denote an external pressure term. Suppose it is steady and moves with a speed V in the $-x$ direction. Then, $p_{\text{ext}}(x, y, t) = p_0(x + Vt, y)$, where $p_0(x, y)$ denotes the initial pressure distribution. In order to include the pressure term in the boundary value problem, it is introduced into the linearized unsteady Bernoulli equation (Equation 2.15):

$$\frac{\partial \phi}{\partial t} + \frac{p_{\text{ext}}(x, y, t)}{\rho} + g\eta = 0. \tag{2.35}$$

The two free surface boundary conditions can again be combined into one boundary condition by differentiating Equation 2.35 with respect to time and substituting the kinematic free surface boundary condition $\frac{\partial \phi}{\partial z} = \frac{\partial \eta}{\partial t}$. This yields

$$\frac{\partial^2 \phi}{\partial t^2} + g\frac{\partial \phi}{\partial z} = -\frac{1}{\rho}\frac{\partial p_{\text{ext}}}{\partial t} \qquad \text{at } z = 0. \tag{2.36}$$

Moreover, deep water will be assumed as opposed to the finite depth from Section 2.1. Hence, the boundary value problem in presence of an external pressure distribution becomes:

$$\nabla^2 \phi = 0, \tag{2.37}$$

$$\frac{\partial \phi}{\partial z} = 0 \qquad \text{as } z \to \infty, \tag{2.38}$$

$$\frac{\partial^2 \phi}{\partial t^2} + g\frac{\partial \phi}{\partial z} = -\frac{1}{\rho}\frac{\partial p_{\text{ext}}}{\partial t} \qquad \text{at } z = 0. \tag{2.39}$$

A general solution to Equation 2.37 is given by

$$\phi_h(x, y, z, t) = Ae^{i(\omega t + k_x x + k_y y)}e^{kz}, \tag{2.40}$$

where A is a constant depending on the boundary conditions. If the reference frame is fixed to the moving pressure distribution, the waves are stationary. In that case, $\omega = k_x V$ (see Appendix A). Substitution of ω into Equation 2.40 yields

$$\phi_h(x, y, z, t) = Ae^{i(k_x Vt + k_x x + k_y y)}e^{kz}, \tag{2.41}$$

$$= Ae^{i(k_x(x+Vt) + k_y y)}e^{kz}. \tag{2.42}$$

Since the PDE is linear and homogeneous, any linear combination of such solutions is also a solution. Therefore, the velocity potential may be expressed by

$$\phi(x, y, z, t) = \int_{-\infty}^{\infty}\int_{-\infty}^{\infty} A(k_x, k_y)e^{i(k_x(x+Vt)+k_y y)}e^{kz}\mathrm{d}k_x\mathrm{d}k_y \tag{2.43}$$

The amplitudes $A(k_x, k_y)$ are found by substituting Equation 2.43 into Equation 2.36. Note that by evaluating the derivatives of the velocity potential at $z = 0$, the exp(kz) term disappears. Let $\bar{x} = x + Vt$. Then, ϕ is defined by an inverse Fourier transformation of $A(k_x, k_y)$ from the (k_x, k_y) domain to the $(\bar{x}, y)$ domain. Evaluation of the derivatives of ϕ at $z = 0$ yields

$$\phi_z(x, y, z = 0, t) = \int_{-\infty}^{\infty}\int_{-\infty}^{\infty} kA(k_x, k_y)e^{i(k_x(x+Vt)+k_y y)}\mathrm{d}k_x\mathrm{d}k_y, \tag{2.44}$$

$$\phi_{tt}(x, y, z = 0, t) = \int_{-\infty}^{\infty}\int_{-\infty}^{\infty} -V^2k_x^2 A(k_x, k_y)e^{i(k_x(x+Vt)+k_y y)}\mathrm{d}k_x\mathrm{d}k_y. \tag{2.45}$$

Here, note that $\phi_z(x, y, z = 0, t)$ is the inverse Fourier Transform of $kA(k_x, k_y)$ and $\phi_{tt}(x, y, z = 0, t)$ is the inverse Fourier transform of $-V^2 k_x^2 A(k_x, k_y)$. Hence, substitution of the above two identities into Equation 2.36 yields

$$\mathcal{F}^{-1}\left[-V^2 k_x^2 A(k_x, k_y)\right] + g\mathcal{F}^{-1}\left[kA(k_x, k_y)\right] = -\frac{1}{\rho}\frac{\partial p_{\text{ext}}}{\partial t}, \tag{2.46}$$

where $\mathcal{F}^{-1}$ denotes inverse Fourier transformation. Now, the rhs can also be linked to its Fourier transform. Since $p_{\text{ext}}(x, y, t) = p_0(x + Vt, y)$, it follows by the chain rule that

$$\frac{\partial p_{\text{ext}}}{\partial t} = \frac{\partial p_0}{\partial t} \tag{2.47}$$

$$= \frac{\partial p_0}{\partial x'}\frac{\partial x'}{\partial t} + \frac{\partial p_0}{\partial y}\frac{\partial y}{\partial t} \tag{2.48}$$

$$= V\frac{\partial p_0}{\partial x'}. \tag{2.49}$$

By the differentiation property of the Fourier transform, it follows that

$$\mathcal{F}\left[\frac{\partial p_0}{\partial x'}\right] = ik_x\hat{p}_0(k_x, k_y), \tag{2.50}$$

where $\hat{p}_0(k_x, k_y)$ is the Fourier transform of the function $p_0(x, y)$. By combining Equation 2.49 and Equation 2.50, it follows that

$$\frac{\partial p_{\text{ext}}}{\partial t} = \mathcal{F}^{-1}\left[ik_x V\hat{p}_0(k_x, k_y)\right]. \tag{2.51}$$

Substituting Equation 2.51 back into Equation 2.46 yields

$$\mathcal{F}^{-1}\left[-V^2 k_x^2 A(k_x, k_y)\right] + g\mathcal{F}^{-1}\left[kA(k_x, k_y)\right] = -\frac{1}{\rho}\mathcal{F}^{-1}\left[ik_x V p_0(k_x, k_y)\right]. \tag{2.52}$$

By taking the Fourier transform over Equation 2.52 and reordering the amplitudes $A(k_x, k_y)$ are found:

$$A(k_x, k_y) = -\frac{ik_x V\hat{p}_0(k_x, k_y)}{\rho(gk - V^2 k_x^2)}. \tag{2.53}$$

An equation for the surface elevation can now be found by substitution of Equation 2.43 and Equation 2.53 into Equation 2.7. This gives

$$\eta(x, y, t) = \int_{-\infty}^{\infty}\int_{-\infty}^{\infty} \frac{kA(k_x, k_y)}{ik_x V} e^{i(k_x(x+Vt)+k_y y)}\mathrm{d}k_x\mathrm{d}k_y, \tag{2.54}$$

$$= \int_{-\infty}^{\infty}\int_{-\infty}^{\infty} -\frac{k\hat{p}_0(k_x, k_y)}{\rho(gk - V^2 k_x^2)} e^{i(k_x(x+Vt)+k_y y)}\mathrm{d}k_x\mathrm{d}k_y. \tag{2.55}$$

Since the moving pressure distribution is assumed to be steady, the equation above can be evaluated at any time t. Hence, let $t = 0$. The equation simplifies to

$$\eta(x, y) = \int_{-\infty}^{\infty}\int_{-\infty}^{\infty} -\frac{k\hat{p}_0(k_x, k_y)}{\rho(gk - V^2 k_x^2)} e^{i(k_x x+k_y y)}\mathrm{d}k_x\mathrm{d}k_y. \tag{2.56}$$

Note that the denominator of the integrand is zero for values of k_x, k_y such that $gk - V^2 k_x^2 = 0$. Since these values are located on the real plane, there are poles on the domain of integration. In contour integration, multiple contours could be chosen to avoid the poles. However, these contours may lead to different answers. Therefore, the integral is not well defined. To circumvent this problem, a radiation condition is imposed on the problem. The radiation condition states that no energy has been generated at infinity. In [26, p. 267] this is done by imposing that $\omega = k_x V - i\varepsilon$. Subsequently, the limit of $\varepsilon \to 0$ is considered. The surface elevation integral becomes

$$\eta(x, y) = \lim_{\varepsilon\to 0}\int_{-\infty}^{\infty}\int_{-\infty}^{\infty} -\frac{k\hat{p}_0(k_x, k_y)}{\rho(gk - (k_x V - i\varepsilon)^2)} e^{i(k_x x+k_y y)}\mathrm{d}k_x\mathrm{d}k_y. \tag{2.57}$$

Note that the effect of the ε-term is that the poles have shifted onto the imaginary axis. Therefore, the poles are no longer on the path of integration. Now a change of variables from k_x, k_y to k, θ is introduced following

$$k_x = k\cos\theta, \tag{2.58}$$

$$k_y = k\sin\theta, \tag{2.59}$$

where k is the magnitude of the wavenumber vector and θ denotes the wave direction. The determinant of the Jacobian of this transformation is given by k. Using the change of variables the surface elevation may be expressed as

$$\eta(x,y) = \lim_{\varepsilon\to 0}\int_{-\infty}^{\infty}\int_{-\pi/2}^{\pi/2} -\frac{k^2\hat{p}_0(k\cos\theta, k\sin\theta)}{\rho(gk-(k\cos\theta V - i\varepsilon)^2)} e^{ik(x\cos\theta + y\sin\theta)}\mathrm{d}\theta\mathrm{d}k. \tag{2.60}$$

After reordering and neglecting the $\mathcal{O}(\varepsilon^2)$ term, the form as presented in [13] is found:

$$\eta(x,y) = \lim_{\varepsilon\to 0}\int_{-\infty}^{\infty}\int_{-\pi/2}^{\pi/2} -\frac{\hat{p}_0(k\cos\theta, k\sin\theta)}{\rho(g/k - V^2\cos^2\theta + 2i\varepsilon V\cos\theta/k)} e^{ik(x\cos\theta + y\sin\theta)}\mathrm{d}\theta\mathrm{d}k. \tag{2.61}$$

Thereafter, in [13] the equation is non-dimensionalized to emphasize the influence of the Froude number on the Kelvin wake pattern. The Froude number is given by $Fr = V/\sqrt{gL}$, where L is a characteristic length scale. Subsequently, the other variables can be normalized using this characteristic length, i.e.,

$$\zeta = \frac{\eta}{L} \qquad X = \frac{x}{L} \qquad Y = \frac{y}{L} \qquad K = kL \qquad \hat{P}_0 = \frac{\hat{p}_0}{\rho g L^3} \qquad \tilde{\varepsilon} = \frac{\varepsilon}{\sqrt{g/L}}. \tag{2.62}$$

Note that $\hat{p}_0$ is the Fourier transformed version of $p_0(x,y)$. Hence, it has units of N as opposed to N/m^2. Moreover, ε is related to the angular frequency ω, hence it has units s^{-1}. Substitution of the nondimensional quantities yields

$$\zeta(X,Y) = \lim_{\tilde{\varepsilon}\to 0}\int_{-\infty}^{\infty}\int_{-\pi/2}^{\pi/2} -K\frac{\hat{P}_0(k\cos\theta, k\sin\theta)}{1 - KFr^2\cos^2\theta + 2iFr\tilde{\varepsilon}\cos\theta} e^{iK(X\cos\theta + Y\sin\theta)}\mathrm{d}\theta\mathrm{d}k. \tag{2.63}$$

Equation 2.63 still depends on $\tilde{\varepsilon}$. It is therefore not yet suitable for numerical approximation. In order to get rid of the ε-dependence, a result from complex analysis is used. The Sokhotski-Plemelj formula is given by [3, p. 226]

$$\lim_{\varepsilon\to 0}\int_{-\infty}^{\infty}\frac{f(x)}{x - x_0 - i\varepsilon}\mathrm{d}x = p.v.\int_{-\infty}^{\infty}\frac{f(x)}{x - x_0}\mathrm{d}x + i\pi f(x_0), \tag{2.64}$$

where $p.v.$ denotes the Cauchy principal value. In order to apply this formula to Equation 2.63, the order of integration in Equation 2.63 is interchanged. Subsequently, a factor of $Fr^2\cos^2\theta$ is factored out of the denominator. This gives

$$\zeta(X,Y) = \int_{-\pi/2}^{\pi/2}\lim_{\tilde{\varepsilon}\to 0}\int_{-\infty}^{\infty} -K\frac{\hat{P}_0(k\cos\theta, k\sin\theta)/(Fr^2\cos^2\theta)}{1/(Fr^2\cos^2\theta) - K + 2i\tilde{\varepsilon}/(Fr\cos\theta)} e^{iK(X\cos\theta + Y\sin\theta)}\mathrm{d}k\mathrm{d}\theta. \tag{2.65}$$

Let $f(K) = K\hat{P}_0 e^{iK(X\cos\theta + Y\sin\theta)}/(Fr^2\cos^2\theta)$, $\varepsilon' = 2\tilde{\varepsilon}/(Fr\cos\theta)$ and $K_0 = 1/(Fr^2\cos^2\theta)$. Then, Equation 2.65 becomes

$$\zeta(X,Y) = \int_{-\pi/2}^{\pi/2}\lim_{\varepsilon'\to 0}\int_{-\infty}^{\infty}\frac{f(K)}{K - K_0 - i\varepsilon'}\mathrm{d}K\mathrm{d}\theta. \tag{2.66}$$

In this form, the Sokhotski-Plemelj formula can be applied. This gives

$$\zeta(X,Y) = \int_{-\pi/2}^{\pi/2} i\pi f(K_0) + p.v.\int_{-\infty}^{\infty}\frac{f(K)}{K - K_0}\mathrm{d}K\mathrm{d}\theta, \tag{2.67}$$

$$= i\pi\int_{-\pi/2}^{\pi/2} f(K_0)\mathrm{d}\theta + \int_{-\pi/2}^{\pi/2} p.v.\int_{-\infty}^{\infty}\frac{f(K)}{K - K_0}\mathrm{d}K\mathrm{d}\theta. \tag{2.68}$$

It turns out that the second term is rapidly decreasing with distance from the pressure source. To see this, let

$$I(X,Y) = \int_{-\pi/2}^{\pi/2} p.v. \int_{-\infty}^{\infty} \frac{f(K)}{K-K_0} \mathrm{d}K\mathrm{d}\theta \tag{2.69}$$

By transforming back from polar to Cartesian coordinates, the integral becomes

$$I(X,Y) = \int_{-\infty}^{\infty} p.v. \int_{-\infty}^{\infty} \frac{K_0\hat{P}_0(K)}{K-K_0} \exp(i(K_xX + K_yY))\mathrm{d}K_x\mathrm{d}K_y. \tag{2.70}$$

Here, note that $I(X,Y)$ is the inverse Fourier Transform of $\frac{K_0\hat{P}_0(K)}{K-K_0}$. If the external pressure distribution $\hat{P}_0(K)$ is chosen to be a rapidly decreasing function in K, $\frac{K_0\hat{P}_0(K)}{K-K_0}$ is also rapidly decreasing in K. The Schwartz space of rapidly decreasing functions is closed under Fourier transformation. Therefore, $I(X,Y)$ is also rapidly decreasing in X and Y. Thus, at a distance sufficiently far from the pressure distribution, $I(X,Y)$ may be neglected. Then, the surface elevation due to a moving pressure distribution can finally be approximated by

$$\zeta(X,Y) \approx i\pi \int_{-\pi/2}^{\pi/2} f(K_0)\mathrm{d}\theta, \tag{2.71}$$

where

$$f(K_0) = K_0^2\hat{P}_0(K_0,\theta)\exp\left(iK_0\left(X\cos\theta + Y\sin\theta\right)\right), \tag{2.72}$$

$$K_0 = 1/(Fr^2\cos^2\theta). \tag{2.73}$$

2.3.1. Numerical evaluation

In this section, Equation 2.71 is evaluated numerically for different values of the hull Froude number. The Froude number was defined as $Fr = V/\sqrt{gL}$, where L is a characteristic length scale. Let the ship speed V be constant. Then, only L can be changed to vary the Froude number. This aims to capture the effect of different hull geometries on the produced surface elevation pattern.

In order to evaluate Equation 2.71, an initial pressure distribution needs to be chosen. A simple choice is a two-dimensional isotropic Gaussian function, i.e.,

$$p_0(x,y) = \exp\left(-\frac{1}{2}\left(\frac{x^2+y^2}{\sigma^2}\right)\right), \tag{2.74}$$

where σ needs to be chosen to represent an appropriate length scale. To that end, it will be related to the length scale defining the Froude number. In many marine applications, the length scale is taken as the length of the ship at the waterline. Therefore, L can be interpreted as such. Then, L needs to be related to σ from the Gaussian distribution. Here, L is chosen such that it equates the width of 95% of probability density of the Gaussian. This yields that $\sigma = L/4$. Hence, the initial pressure distribution becomes

$$p_0(x,y) = \exp\left(-8\left(\frac{x^2+y^2}{L^2}\right)\right). \tag{2.75}$$

Up to a constant, the Fourier transform of the above function is given by

$$\hat{p}_0(k_x,k_y) \propto \exp\left(-\frac{L^2}{32}\left(k_x^2+k_y^2\right)\right). \tag{2.76}$$

Substitution of $K = kL$ yields the nondimensionalized Fourier transform of the pressure distribution:

$$\hat{P}_0(K) \propto \exp\left(-\frac{K^2}{32}\right). \tag{2.77}$$

To compare the resulting surface elevation fields for different Froude numbers, it should be noted that the wavelengths in the field scale with the Froude number squared. To produce the same number of wavelengths for different Froude numbers, the coordinates X and Y are scaled by the Froude number according to

$$\tilde{X} = \frac{X}{\Lambda} \qquad \tilde{Y} = \frac{Y}{\Lambda}, \tag{2.78}$$

where $\Lambda = 2\pi Fr^2$.
Subsequently, Equation 2.71 is approximated using the trapezoidal rule over a uniform grid over θ consisting of 500 cells. The spatial coordinates $\tilde{X}, \tilde{Y}$ are discretized on a uniform rectangular grid of 600×600 cells.
In Figure 2.3 the resulting surface elevations are shown for Froude numbers of 0.4, 0.7 and 1 respectively. In the top three panels, the corresponding generating pressure distributions are given. Note that the pressure distributions are given on a different spatial scale compared to the surface elevation plots. Lastly, in the final row, the discrete Fourier transforms of the surface elevation fields are given. In these spectra, the red lines show one side of the curves predicted by Equation 2.32.

Clearly, the surface elevation patterns resemble Kelvin wakes. At a Froude number of 0.4, the transverse waves dominate the pattern. The transverse waves are those waves which travel more or less parallel to the sailing line. At increasing Froude number, the divergent waves are also introduced. These are the waves moving at an angle away from the sailing line. Consequently, a larger variety in wave direction is found at larger Froude number.

In the wavenumber spectra, the energy is clearly distributed over the shape of the forward model derived in Section 2.2. Moreover, at increasing Froude number, the energy is more spread out over the curves produced by the forward model. This represents the increased variety in wave direction at increased Froude numbers. A practical consequence of this is that ships sailing at higher Froude number generate a Kelvin wake with a more defined spectral signal. This might make the signal more distinguishable from the noise in spectra derived from real imagery. Therefore, it is expected that a more robust fit of the forward Kelvin wake model is possible at higher Froude number.

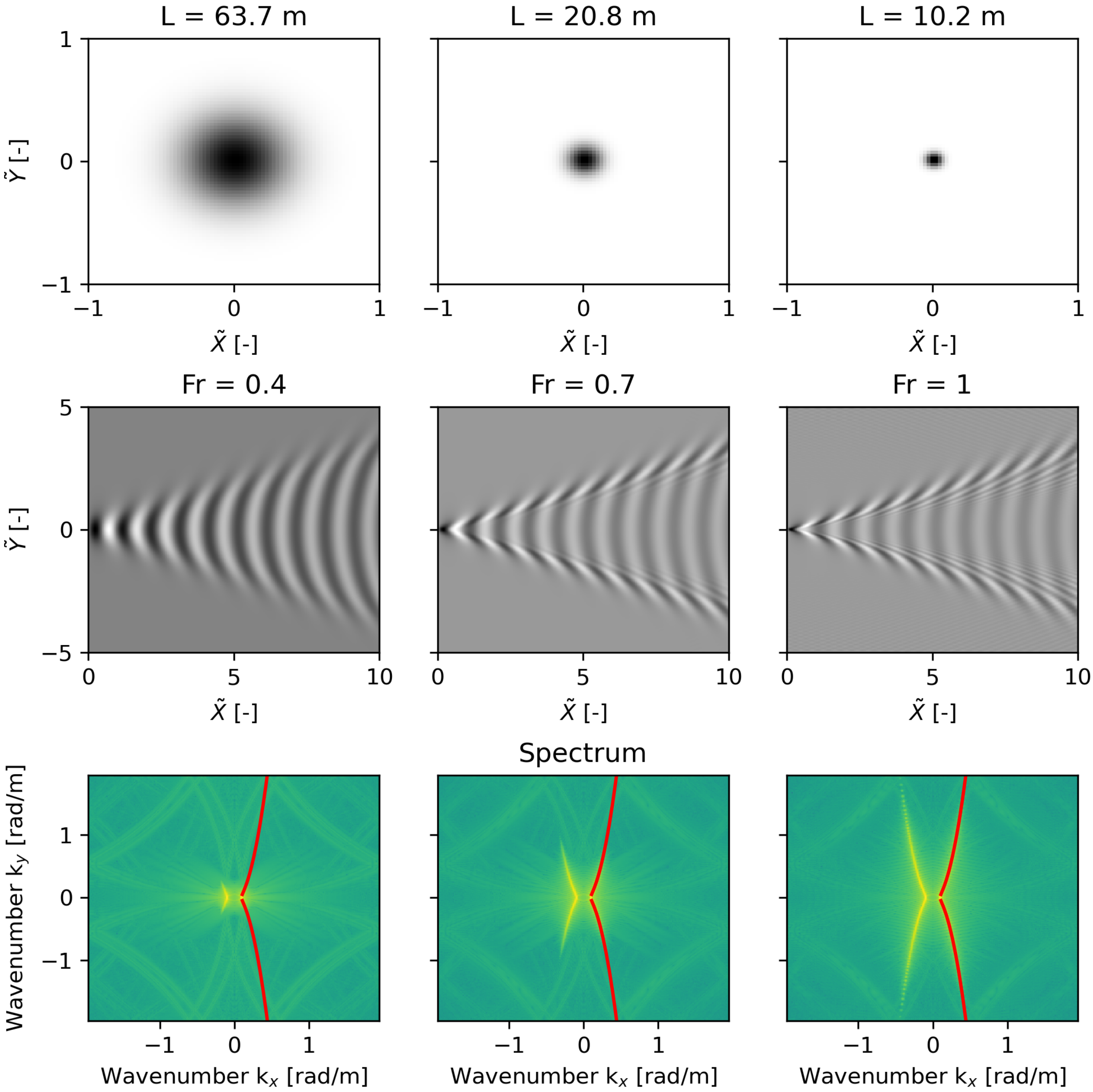

Figure 2.3: First row: assumed pressure distributions given by Equation 2.75. Second row: simulated surface elevation patterns for three different Froude numbers, produced by numerical approximation of Equation 2.71. Third row: Discrete Fourier Transforms of the surface elevation plots. The red lines visualize the forward model from Equation 2.32.

Evidently, the shape of a ship is not well approximated by an isotropic Gaussian as in Figure 2.3. A first step towards a more realistic pressure distribution can be achieved by choosing an anisotropic Gaussian. An uncorrelated bivariate Gaussian is given by

$$p_0(x, y) = \exp\left(-\frac{1}{2}\left(\frac{x^2}{\sigma_x^2} + \frac{y^2}{\sigma_y^2}\right)\right), \tag{2.79}$$

where σ_x and σ_y control the width of the Gaussian in x and y-direction respectively. The corresponding Fourier transform is given by

$$\hat{p}_0(k_x, k_y) \propto \exp\left(-\frac{1}{2}\left(\sigma_x^2 k_x^2 + \sigma_y^2 k_y^2\right)\right). \tag{2.80}$$

Suppose the width of a ship is a quarter of its length. Then, $\sigma_y = \sigma_x/4$. Let $\sigma_x = L/4$ as before. After non-dimensionalization, the Fourier transform of the pressure distribution becomes

$$\hat{P}_0(K,\theta) \propto \exp\left(-\left(\frac{K^2\cos^2(\theta)}{32}+\frac{K^2\sin^2(\theta)}{512}\right)\right). \tag{2.81}$$

Now, numerical evaluation of Equation 2.71 yields the results in Figure 2.4. As can be seen, the pressure distributions already become more reminiscent of the shape of a ship. It can be seen that the divergent waves now start to become important at a lower Froude number than before. This can also be seen in the wavenumber spectra, where the spectrum for a Froude number of 0.4 resembles the spectrum for a Froude number of 0.7 from the previous simulations.

In practice, the hull shape of a ship will not be known from satellite imagery. However, here it is shown that for different pressure distributions, the energy in the spectrum is still contained along the curve given by Equation 2.32. Hence, although the hull geometry influences the distribution of energy over the curves, it does not influence the location of the curves in the spectrum. This indicates that the current retrieval algorithm should not be sensitive to the ship hull geometry.

Although a much more accurate pressure distribution could be constructed, the simulated surface elevation patterns are realistic enough for their use in this thesis. In Chapter 6, the spatial Kelvin wake model is used with a reflectance model to study the influence of the viewing geometry on the visibility of a Kelvin wake on satellite imagery.

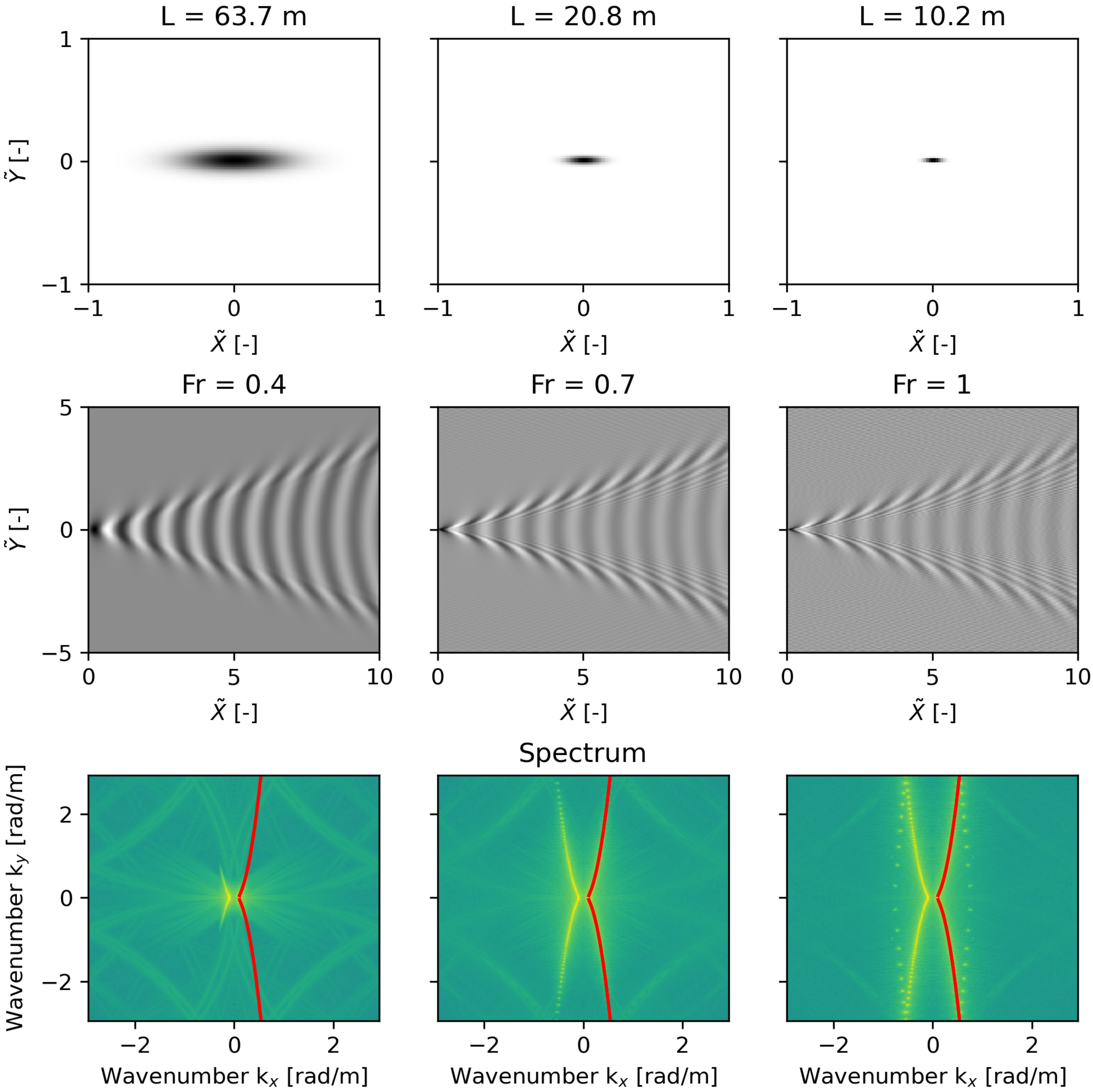

Figure 2.4: First row: assumed pressure distributions given by Equation 2.79 with $\sigma_x = L/4$ and $\sigma_y = L/16$. Second row: simulated surface elevation patterns for three different Froude numbers, produced by numerical approximation of Equation 2.71. Third row: Discrete Fourier Transforms of the surface elevation plots. The red lines visualize the forward model from Equation 2.32.

3

Model fitting

This chapter will show how a ship's Speed Through Water (STW) and Course Through Water (CTW) can be retrieved from an image of its Kelvin wake. First, Section 3.1 will outline how the spectral signal corresponding to the Kelvin wake is extracted from a satellite image. Thereafter, in Section 3.2 an algorithm is presented to fit the forward model derived in Section 2.2 to an observed Kelvin wake signal. A correction to the estimated CTW due to a conversion between map projections is given in Section 3.3. Finally, Section 3.4 covers some examples.

3.1. From spatial to spectral domain

In Section 2.2 a model for the spectral signature of a Kelvin wake was derived. Satellite imagery naturally shows Kelvin wakes in the spatial domain. Thus, to compare the data with the model, a satellite image needs to be mapped from the spatial to the spectral domain. To that end, the Discrete Fourier Transform (DFT) is used. In 2 dimensions, the DFT of a digital image is given by [14]

$$S[k,l] = \frac{1}{MN}\sum_{m=0}^{M-1}\sum_{n=0}^{N-1} x[m,n]e^{-2\pi i\left(\frac{mk}{M}+\frac{nl}{N}\right)} \qquad k=0,\dots,M-1; \quad l=0,\dots,N-1, \tag{3.1}$$

where

- M is the number of rows in the image,
- N is the number of columns in the image,
- $x[m,n]$ is the value of the image at the mth row and nth column,
- $S[k,l]$ is the complex Fourier coefficient.

An example of applying the DFT to a satellite image of a Kelvin wake is given in Figure 3.1. The shape of the forward model (Figure 2.1b) can already be recognized. However, the spectrum still contains much energy at frequencies that do not correspond to the Kelvin wake signal. A part of this energy comes from the ship having a much larger intensity than the water. This introduces large intensity gradients in the optical image, which require many different frequencies to represent in the spectral domain. Another part of the undesired energy in the spectrum comes from spectral leakage. Spectral leakage is the phenomenon that energy at a frequency that is not exactly one of the DFT analysis frequencies will spread out over all other frequency bins.

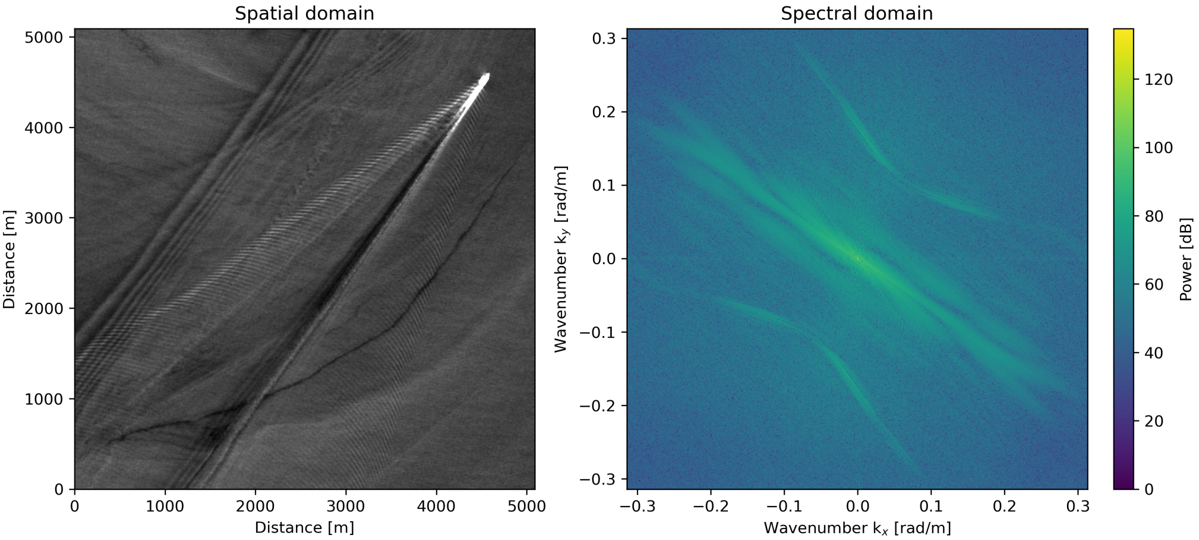

Figure 3.1: a) Example of a Sentinel-2 image of a Kelvin wake. b) Discrete Fourier transform of a).

To mitigate these problems, the optical image is multiplied with a window function before Fourier transformation. A window function is typically a bell-shaped function which smooths the underlying data. Generally, this reduces the amount of spectral leakage at frequencies far away from the true frequency. The disadvantage of a window function is that it reduces spectral resolution. Spectral resolution is important for this application as the location of the Kelvin wake signal in the spectrum determines the ship speed through water. Thus, for an accurate retrieval, good spectral resolution is desired. Therefore, the choice of a window function is a trade-off between reducing spectral leakage and not decreasing spectral resolution too much. The Hann-window function was found to provide a good balance between these issues. In Figure 3.2a, the Hann-windowed satellite image is shown. In Figure 3.2b the resulting Fourier transform is shown. Clearly, undesirable energy has been suppressed while the Kelvin wake signal remains well defined.

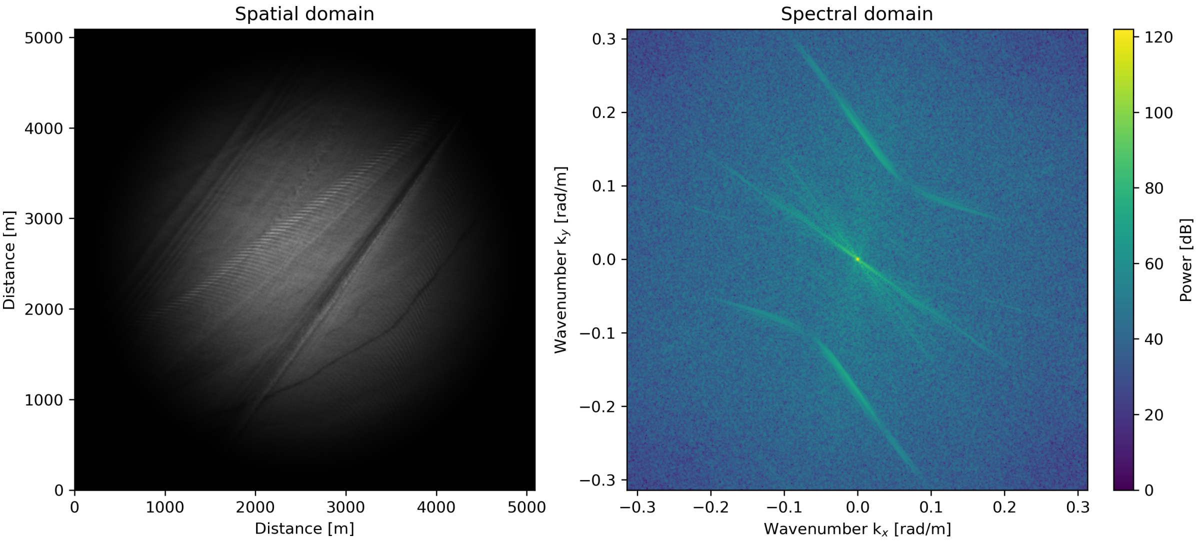

Figure 3.2: a) Same Sentinel-2 image as in Figure 3.1a, however now multiplied by a Hann window. b) Discrete Fourier transform of a).

Next, two more steps are taken to further isolate the Kelvin wake signal from the spectrum. In the spectrum, there is more energy at the low frequencies (near the origin) than at the high frequencies (near the corners). Thus, there exists a radial trend in the spectrum. Therefore, the following equation is fitted to the spectrum using least squares:

$$S(k_x, k_y) = a\sqrt{k_x^2 + k_y^2} + b, \tag{3.2}$$

where a and b are constants to be fitted. In Figure 3.3a the fitted trend corresponding to Figure 3.2b is given. After subtracting this radial trend from the spectrum, all pixels with a value below 0 are removed. The remaining spectrum is shown in Figure 3.3b. In this form, the spectrum is ready to be fit to the model.

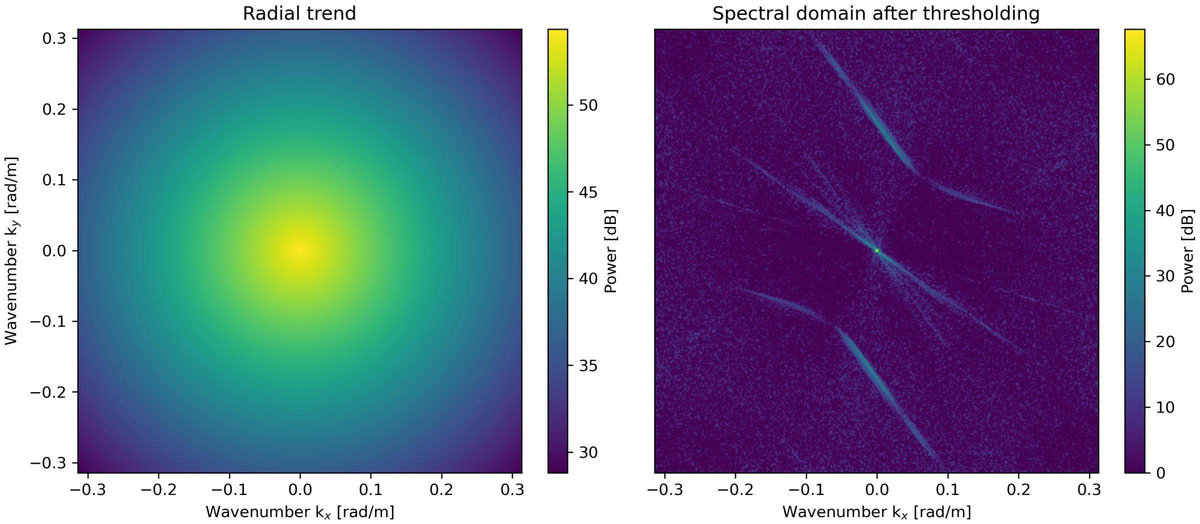

Figure 3.3: a) Least squares fit of a radial trend to Figure 3.2b. b) Remaining signal after subtracting radial trend and rejecting pixels with a value below 0.

3.2. From spectral to parameter domain

The previous section showed how the spectral Kelvin wake signal is extracted from a satellite image. In Section 2.2, a forward model for this signal was derived. Therefore, an algorithm that fits the forward model to the observed spectrum is needed. This inverse problem can be interpreted as a curve-detection problem, i.e., finding where a curve is located within the spectrum. It will here be solved using a modification of the Generalized Radon Transform (GRT).

The GRT of a spectrum S with coordinates $k = (k_x, k_y)$ is given by [32]

$$\mathscr{R}\{S\}(p) = \int_{C_p} S(k)\mathrm{d}k, \tag{3.3}$$

where C_p denotes the curve corresponding to the forward model with parameters $p = (V_{\mathsf{STW}}, \theta_{\mathsf{CTW}})$.

The goal of the GRT is to find the set of parameters p such that the curve C_p aligns with the Kelvin wake signal present in S. To that end, initial guesses of p are first defined. Subsequently, for each candidate set p, a line integral along C_p over $S(k)$ is computed. In Figure 3.4a, the curves C_p for three inaccurate guesses of p are shown. As can be seen, the curves do not align with the Kelvin wake signal. Therefore, the value of the line integral will be small. On the other hand, Figure 3.4b shows a curve C_p for an accurate guess of p. Now, the model overlaps with the Kelvin wake signal. Therefore, the value of the line integral is large. The GRT computes the line integral over all prescribed initial guesses for p. Finally, the best fit is given by the set of parameters that maximizes the line integral.

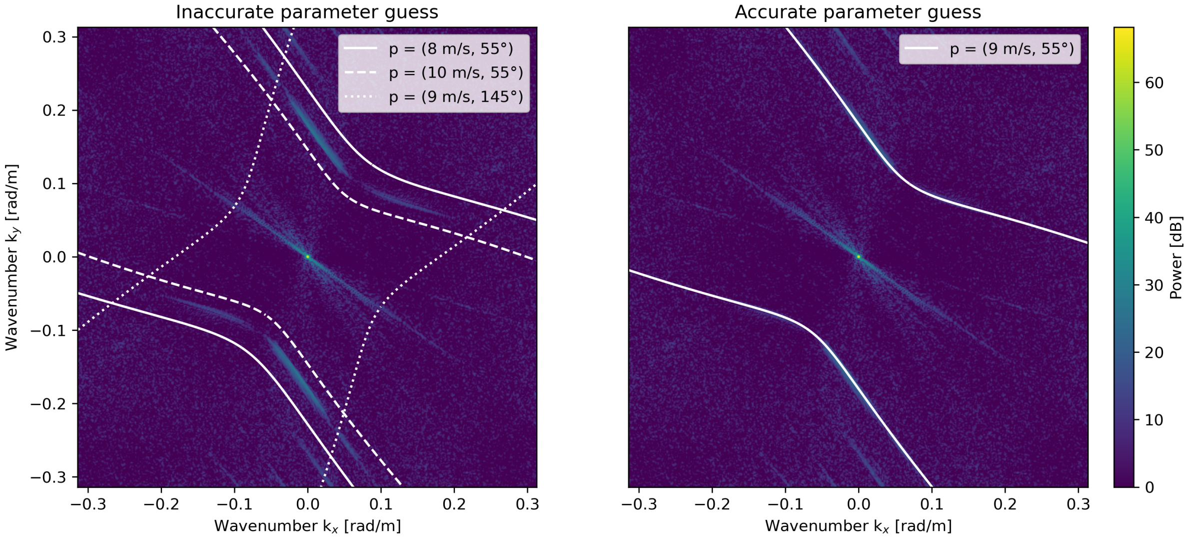

Figure 3.4: a) Examples of inaccurate guesses of the parameter set p that yield a model curve C_p that does not align with the Kelvin wake signal. b) Example of accurate guess of the parameter set p yielding a model curve that lines up with the observed curve.

In practice, there are only a finite number of pixels in an image. Hence, the line integral in Equation 3.3 is discretized which gives

$$\mathscr{R}\{S\}(p) = \sum_{i=0}^{N-1} S(k_i), \tag{3.4}$$

where k_i for $i \in \{0, N-1\}$ represent the image coordinates of the pixels located along curve C_p. However, in this application, the curves produced by the forward model have different lengths for different combinations of parameters. Hence, a bias towards longer curves may be introduced. Therefore, the GRT is modified to take the average along a curve instead of only summing the relevant pixels. This gives

$$\mathscr{R}\{S\}(p) = \frac{1}{N}\sum_{i=0}^{N-1} S(k_i). \tag{3.5}$$

The GRT defines a mapping from the spectral domain to a parameter domain. The parameter domain, also called the Radon domain, is spanned by V_{STW} and θ_{CTW}. Hence, the result of the GRT can also be shown as a 2D image. An example of this is shown in Figure 3.5. Every point in this parameter domain corresponds to a combination of V_{STW} and θ_{CTW}. The intensity at this point is equal to the average power in the spectrum over the curve produced by this combination of parameters. Hence, a large intensity means that the model curve is overlapping with a signal in the spectral domain. Therefore, the location of the maximum in the parameter domain gives the fitted parameters, i.e.,

$$\hat{p} = (\hat{V}_{\text{STW}}, \hat{\theta}_{\text{CTW}}) = \underset{p}{\text{argmax}}\, \mathscr{R}\{S\}(p). \tag{3.6}$$

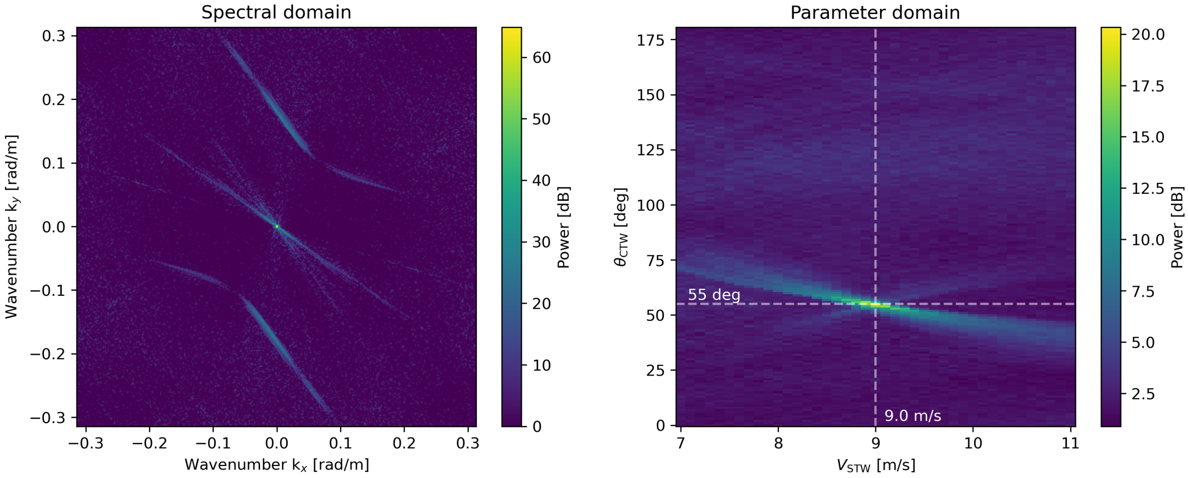

Figure 3.5: a) Filtered Fourier spectrum of windowed Sentinel-2 Kelvin wake image. b) Generalized Radon Transform of a).

3.3. Convergence angle correction

The algorithm presented in the previous section yields an estimate for the ship Course Through Water (θ_{CTW}). However, this angle is measured in the coordinate system corresponding to the Kelvin wake image. For example, Sentinel-2 imagery is given in a local Universal Transverse Mercator (UTM) projection. The importance of this is that a measured direction in the local projection is generally not equal to the direction in a global projection. Since the Course Over Ground (θ_{COG}) reported by the AIS is given with respect to the WGS84 ellipsoidal coordinate reference system, it is necessary to transform the estimated θ_{CTW} from the local to a global projection.

A line of constant x in a local projection points to the grid north. Similarly, a line of equal longitude, i.e., a meridian, points to the true north. Along the central meridian in a UTM projection, grid north and true north coincide. The difference between the grid north and true north increases as the distance from a point to the central meridian increases. The angle between the true north and the grid north is called the grid convergence [35]. For the spherical transverse Mercator projection, the convergence angle is given by [35]

$$\gamma(\lambda, \phi) = \tan^{-1}(\tan(\lambda - \lambda_0) \sin \phi), \tag{3.7}$$

where λ and ϕ denote longitude and latitude respectively. The longitude of the central meridian in the local projection is represented by λ_0. For example, Sentinel-2 imagery over the Strait of Gibraltar is given in UTM zone 30N. This zone has the central meridian at -3°, hence $\lambda_0 = -3^\circ$. By substituting the ship's location into Equation 3.7, the relevant convergence angle is found. Subsequently, the Course Through Water can be corrected following

$$\theta_{\text{CTW,global}} = \theta_{\text{CTW,local}} - \gamma(\lambda, \phi). \tag{3.8}$$

For all data points considered in this thesis, the magnitudes of the convergence angles ranged between 1.25° and 2.42°. Note that the formula for the convergence angle given above holds for a spherical transverse Mercator projection, not an ellipsoidal transverse Mercator projection. Since UTM zones are based on an ellipsoidal transverse Mercator projection, a small error is introduced. However, implementation of the formulae for the ellipsoidal grid convergence up to 7th order given in [35] has shown that the convergence angles between the two projections differed by approximately $10^{-5\circ}$. Such an error has no effect on the estimated surface currents. Since the expression for the ellipsoidal case is much more tedious, the spherical formulae were used.

3.4. Examples

3.4.1. Fast ships

Ships that sail faster generate longer waves. Longer wavelengths correspond to smaller wavenumbers. Therefore, the spectral Kelvin wake signal corresponding to a fast-moving ship will be closer to the origin than for a slow-moving ship. This effect is clearly visible in the spectral domain of Figure 3.6. The radial location of the Kelvin wake signal is much closer to the origin than in Figure 3.5a.

A consequence of this high ship speed can be seen in Figure 3.7c. The signal in the parameter domain is more stretched out compared to Figure 3.5b. This is explained by the relationship between wavenumber and ship speed. Reordering Equation 2.34 gives

$$k = \frac{g}{V_{\text{STW}}^2}. \tag{3.9}$$

In the spectral domain, each pixel is separated by a constant amount of wavenumber. However, since the equation above is non-linear, a constant spacing in wavenumber does not yield a constant spacing in ship speed.

To illustrate the effect of this, suppose that the spectral signal in Figure 3.7 would be displaced by one pixel towards the origin. The vessel speed of $14.8\,\mathrm{m\,s^{-1}}$ corresponds to a wavenumber of about $0.045\,\mathrm{rad\,m^{-1}}$. Suppose that the wavenumber resolution of the spectrum is $0.001\,\mathrm{rad\,m^{-1}}$. If the signal would be moved by one pixel towards the origin, the corresponding wavenumber would become $0.044\,\mathrm{rad\,m^{-1}}$. This wavenumbers belongs to a ship speed of $14.97\,\mathrm{m\,s^{-1}}$. Hence, a displacement of one pixel in the spectrum caused a change in ship speed of $0.17\,\mathrm{m\,s^{-1}}$.

The above calculations can be repeated for a ship that is sailing much slower, say at a speed of $7\,\mathrm{m\,s^{-1}}$. Then, a shift of one pixel would only lead to a change in ship speed of $0.02\,\mathrm{m\,s^{-1}}$. Hence, at higher ship speeds, the fitted ship speed is more sensitive to a small displacement of the Kelvin wake signal in the spectrum. This can be interpreted by noting that near the origin, one pixel in the spectrum corresponds to a larger range of ship speeds than a pixel near the corners. Therefore, a wider range of candidate ship speeds provide a good fit, which explains the more diffuse shape of the parameter domain in Figure 3.7c compared to Figure 3.5b. As a consequence, the resulting fitted parameters at higher ship speeds might be less reliable than those fitted at lower ship speeds. The uncertainty introduced by this effect is taken into account in Section 5.2.2.

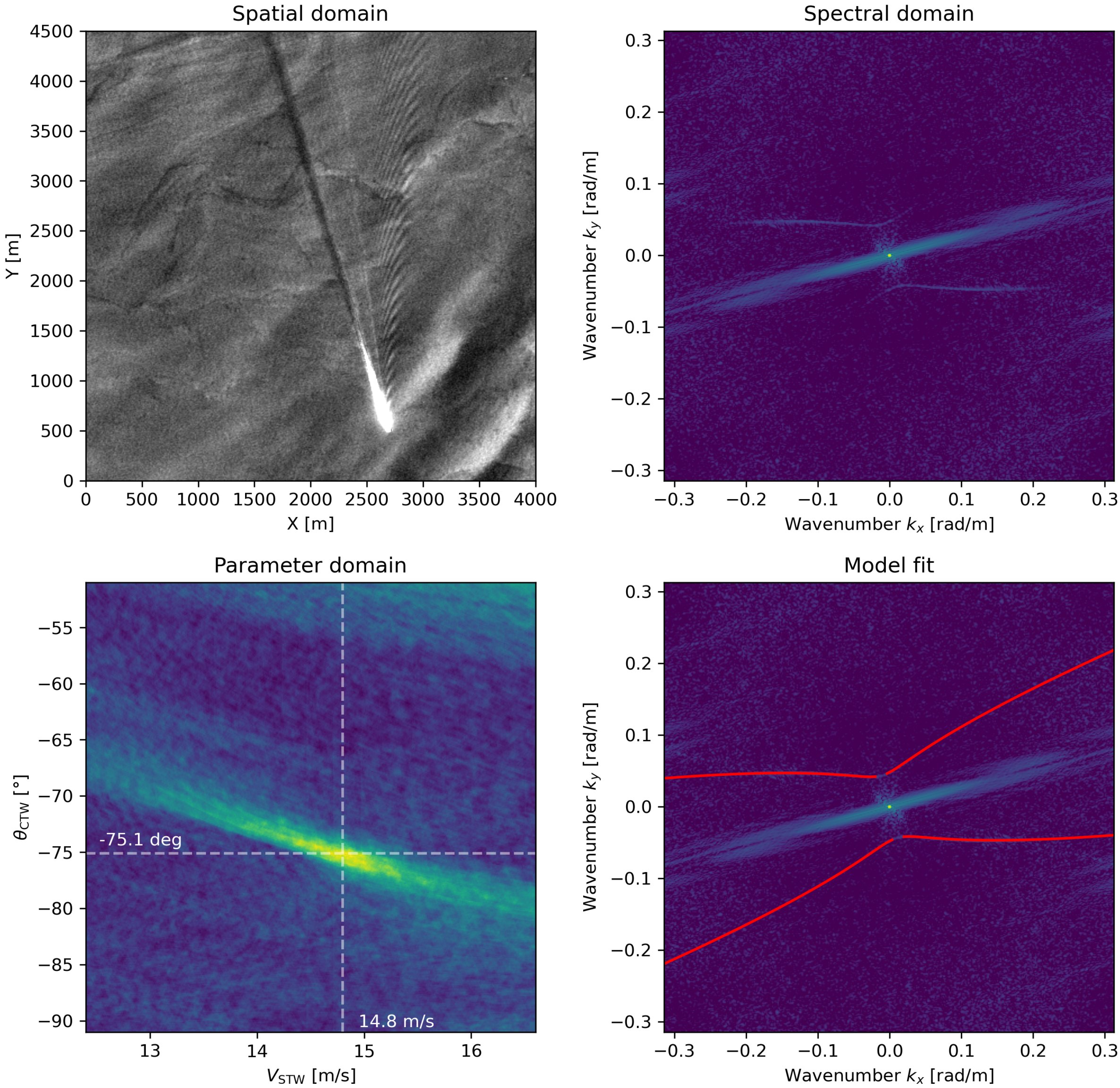

Figure 3.6: a) Sentinel-2 image of a Kelvin wake of a fast-sailing ship. b) Filtered Fourier Transform of a). c) Generalized Radon Transform of b). d) Fitted spectral Kelvin wake model.

3.4.2. Asymmetrical visibility

In some cases, the Kelvin wake is only visible on one side of the ship. In Figure 3.7d, the Kelvin waves are only visible behind the right-side of the ship. In the spectral domains, only half of the curve of the forward model can be recognized. In the parameter domain, this is characterized by a single diagonal line as opposed to two intersecting diagonal lines. The algorithm is still able to detect the signals, though the fitted parameters might be less robust compared to cases where the entire Kelvin wake is visible.

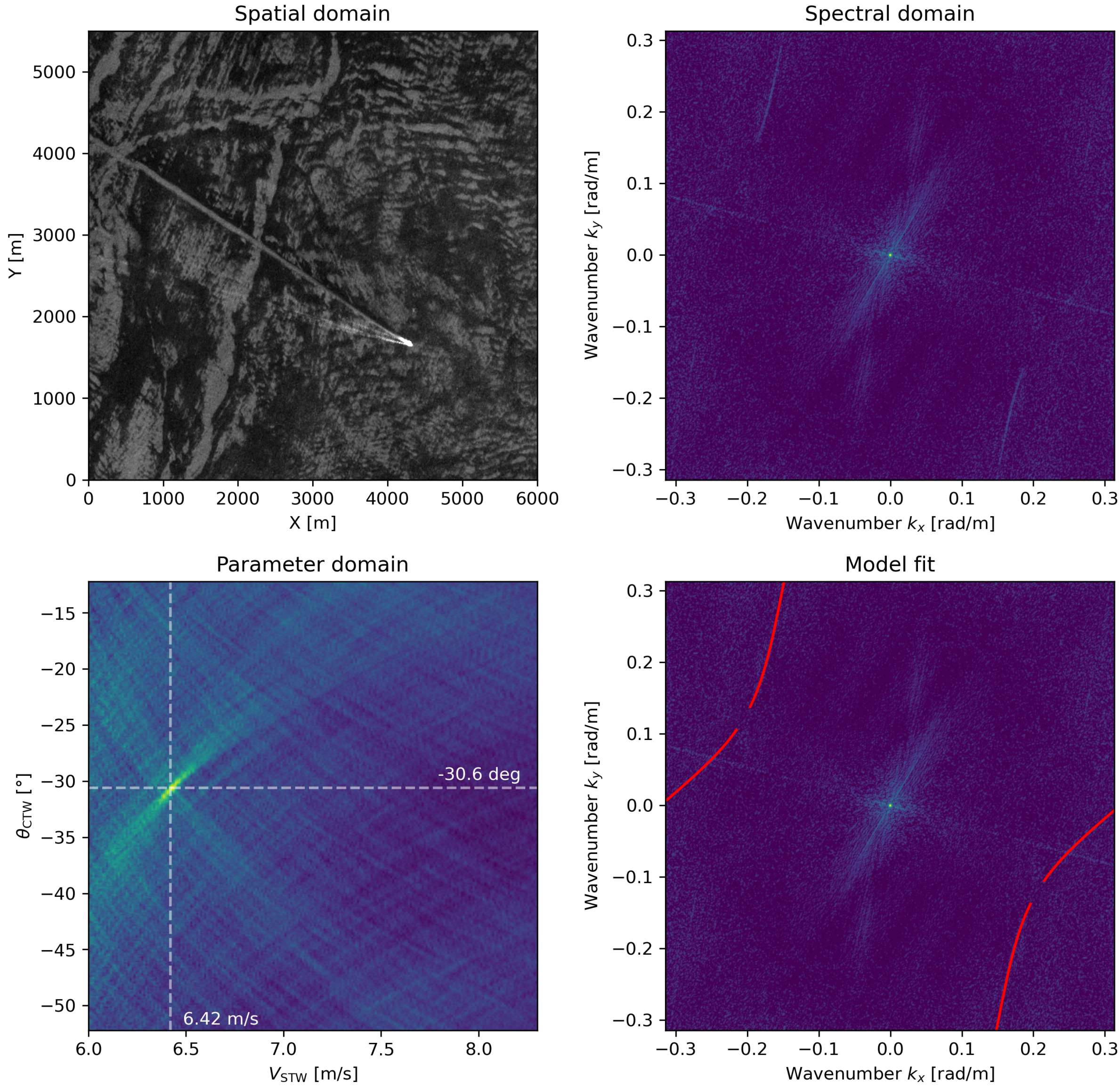

Figure 3.7: a) Sentinel-2 image where the Kelvin wake is only visible behind the right-side of the ship. b) Filtered Fourier Transform of a). c) Generalized Radon Transform of b). d) Fitted spectral Kelvin wake model.

3.4.3. Multiple Kelvin wakes in one image

In Figure 3.8a an image that contains two intersecting Kelvin wakes is given. The Kelvin wake from north to south is most clear. It is generated by a ship that is headed south, just outside of the image frame. Moreover, upon close inspection, it becomes clear that also the bottom ship that is travelling eastwards is leaving a partially visible Kelvin wake. The top eastwards-sailing ship is not generating a visible Kelvin wake. Moreover, its ship speed is too low to correspond to the observed west-to-east spectral signal. In Figure 3.8b the filtered spectral domain is given. There, signals corresponding to both Kelvin wakes can indeed be distinguished. The spectral signal corresponding to the eastwards-sailing ship is smeared out in the radial direction. Although this could generally be indicative of variations in ship speed, this was not observed in this case. Therefore, it is not clear what has caused this radial smearing.

The model fit shown in Figure 3.8c is found for the bottom ship travelling eastwards. Similarly, the fit in Figure 3.8d is found for the ship travelling southwards. Both fits yield an estimate for the surface current. By reprojecting the estimated along- and across-ship currents to east and north components, the two estimated vectors can be more easily compared. The first fit yields east and north currents of $1.62\,\mathrm{m\,s^{-1}}$ and $0.29\,\mathrm{m\,s^{-1}}$ respectively. The second fit yields east and north currents of $1.91\,\mathrm{m\,s^{-1}}$ and $0.15\,\mathrm{m\,s^{-1}}$ respectively. Clearly, the estimates show reasonable agreement.

It should be noted that the two estimates do not correspond to the exact same location. The estimated currents reflect the average conditions along the length of the respective Kelvin wake. Since the ship paths are different, also the encountered flow conditions are different. Therefore, this may explain part of the observed discrepancy. To conclude, this example shows that even if two Kelvin wakes are intersecting, an accurate retrieval of surface currents from both Kelvin wakes may be possible.

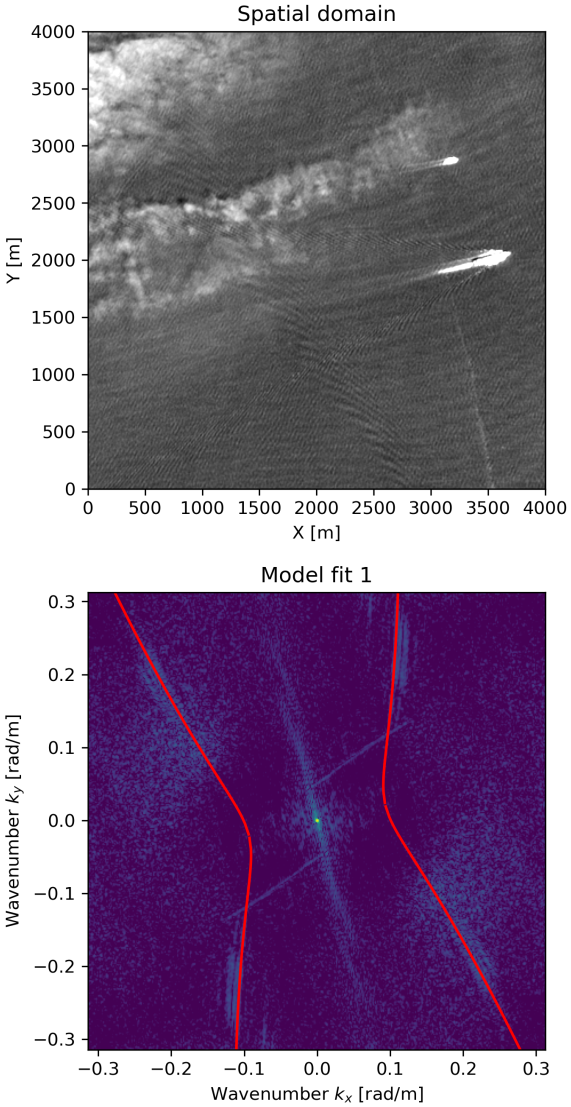

Figure 3.8: a) Sentinel-2 image where two Kelvin wakes are intersecting. b) Filtered Fourier Transform of a). c) Fitted spectral Kelvin wake model for the Kelvin wake oriented east-west. d) Fitted spectral Kelvin wake model for the Kelvin wake oriented north-south.

3.4.4. Background waves

In Figure 3.9a a Sentinel-2 image is shown that contains a visible Kelvin wake along with clear background ocean waves. Interference of background waves with Kelvin waves may lead to reduced visibility of a Kelvin wake. In this case however, the Kelvin wake is still clearly visible in the spectral domain. Furthermore, in the spectral domain the near-triangular patterns correspond to the background waves. Here, the signals from the Kelvin wake and the background waves only show a small spectral overlap. Therefore, the Kelvin wake model is fitted well. However, if there would be more spectral overlap between the two signals, the algorithm may not be able to accurately fit the spectral Kelvin wake model.

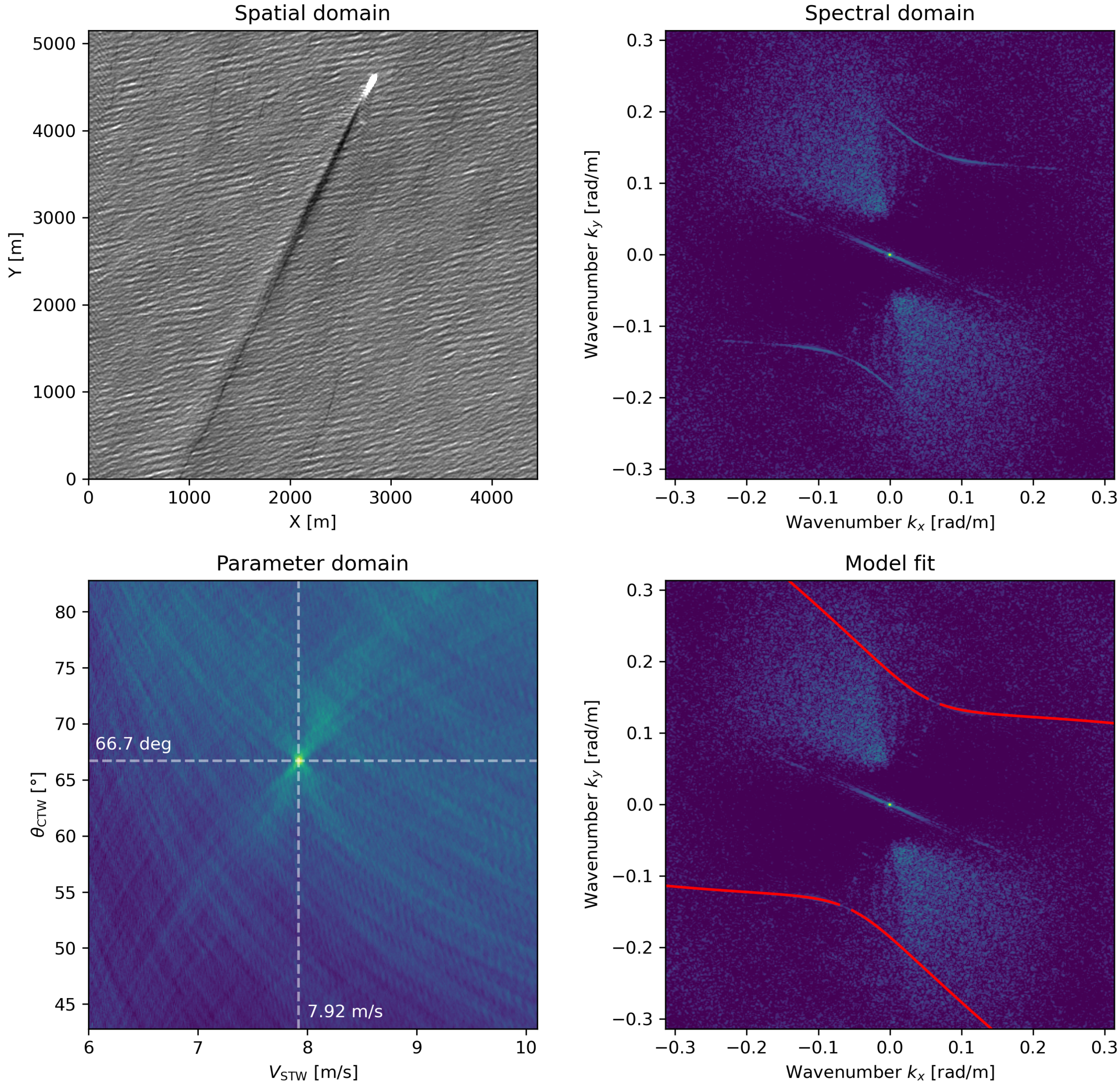

Figure 3.9: a) Sentinel-2 image where a Kelvin wake is visible along with background ocean waves. b) Filtered Fourier Transform of a). c) Generalized Radon Transform of b). d) Fitted spectral Kelvin wake model.

3.4.5. Unsuccessful fit

In some cases, the spectral Kelvin wake signal may be too weak compared to the noise. In Figure 3.10a a small Kelvin wake can be seen behind the ship sailing southwards. In the spectral domain, the corresponding signal is weakly visible. However, after applying the Generalized Radon Transform, the model is fit to noisy pixels in the spectrum. The final model fit is visualized by the red lines in Figure 3.10c. Clearly, the model fit does not align with the Kelvin wake signal. Hence, in this case no surface current retrieval is possible. In total, there were about 10 cases in which the algorithm was not able to provide a good model fit.

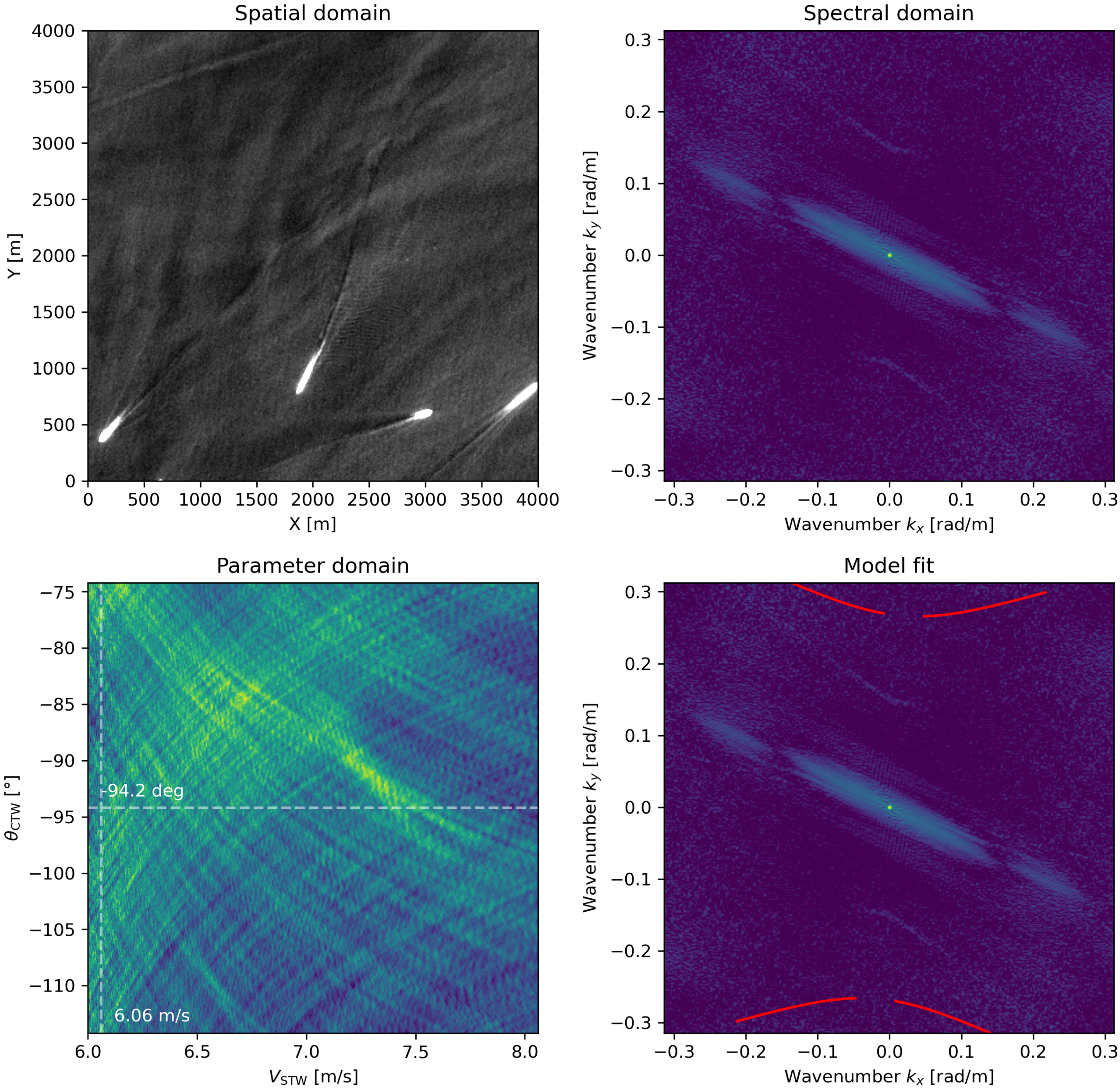

Figure 3.10: a) Sentinel-2 image where a Kelvin wake is partially visible behind the ship sailing south. b) Filtered Fourier Transform of a). c) Generalized Radon Transform of b). d) Fitted spectral Kelvin wake model.

4

Validation

In this chapter, the developed algorithm for estimating surface currents from Kelvin wake imagery is validated. In Section 4.1, the used datasets are given. Subsequently, the methodology is outlined in Section 4.2. Section 4.3.1 and Section 4.3.2 contain the validation for the along- and across-ship components of the surface currents respectively. In Section 4.3.3, the estimated vectors are compared spatially with vector fields derived from validation datasets. Section 4.3.4 discusses the effect of the convergence angle correction on the estimated surface currents.

4.1. Data

4.1.1. Sentinel-2 imagery

Sentinel-2 is a satellite mission that is part of the Copernicus program of the European Space Agency (ESA). The mission currently consists of two nearly identical satellites, Sentinel-2A and Sentinel-2B, flying in an almost identical polar and sun-synchronous orbit [1]. The main instrument aboard each of the satellites is the MultiSpectral Instrument (MSI). The MSI is a passive imager, which means that it measures sunlight reflected by the Earth and its atmosphere. It measures in 13 different wavelength bands, with varying spatial resolutions [1]. The instrument is a pushbroom scanner with a swath width of 290 km [1]. At the equator, the two satellites each have a revisit time of about 10 days [1]. Hence, combined a revisit time of 5 days is reached. However, at higher latitudes, the revisit times decrease due to the convergence of meridians.

In this thesis, only three of the bands in the visible range of the electromagnetic spectrum are used: the red, green and blue bands. This is mainly due to the high spatial resolution of these bands at 10m ground sampling distance, in contrast to the 20 and 60m spatial resolutions at other wavelengths [1]. The Very-Near Infrared (VNIR) band, centered around 833 nm, also has 10 meter spatial resolution. However, the reflectance of water is small in this wavelength range (see Figure 4.1). For further analysis, the three remaining bands are averaged by taking the arithmetic mean to produce a one-dimensional intensity image. Level 2A imagery was downloaded from [10].

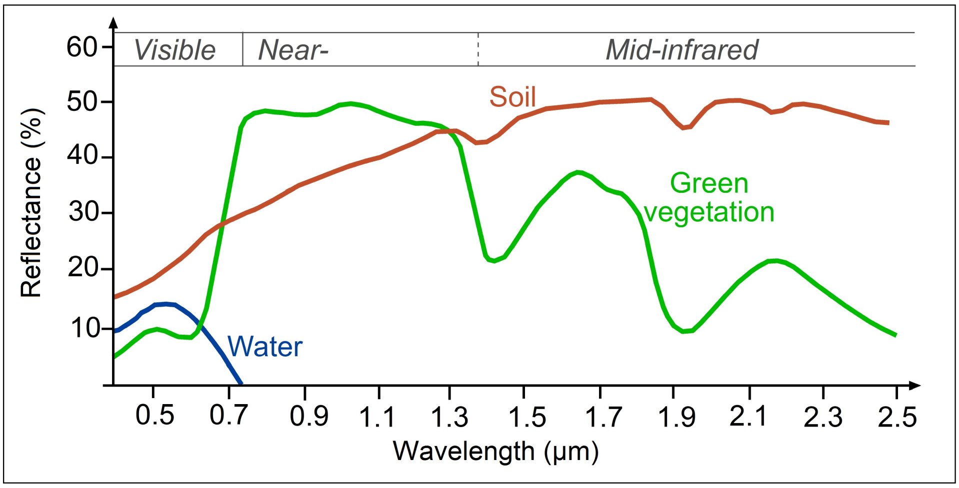

Figure 4.1: Schematic reflectance spectrum of water, soil and vegetation. Image from [41].

North Sea & Kattegat

Several Sentinel-2 level 2A images covering the waters around Denmark during June 2021 were downloaded. A manual scan through these images returned 16 visible Kelvin wakes. Their locations are shown in Figure 4.2. The Sentinel-2 images were manually cropped around the Kelvin wakes, so that a dataset of 16 images of Kelvin wakes resulted.

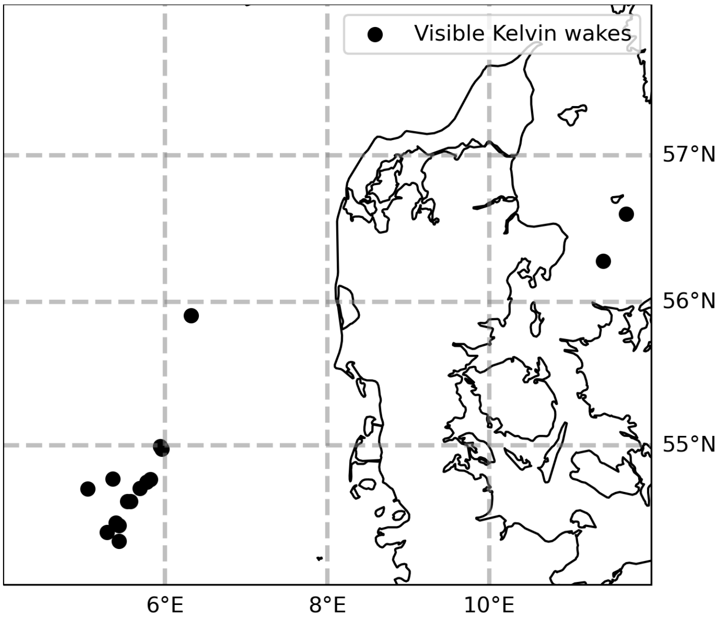

Figure 4.2: Locations of the 16 Kelvin wakes around Denmark that were visible on Sentinel-2 imagery.

Strait of Gibraltar

All Sentinel-2 level 2A imagery covering the Strait of Gibraltar during July and August of 2021 was downloaded. This returned a collection of 25 images. The AIS data covering the same time period was filtered for ships sailing faster than $5.6\,\mathrm{m\,s^{-1}}$. Subsequently, the ships were manually looked up on the corresponding Sentinel-2 image. In 5 images, no visible Kelvin wake was found. In the remaining 20 images, 81 visible Kelvin wakes were distinguished. Their locations are shown in Figure 4.3. The Sentinel-2 images were cropped around the Kelvin wakes for further processing.

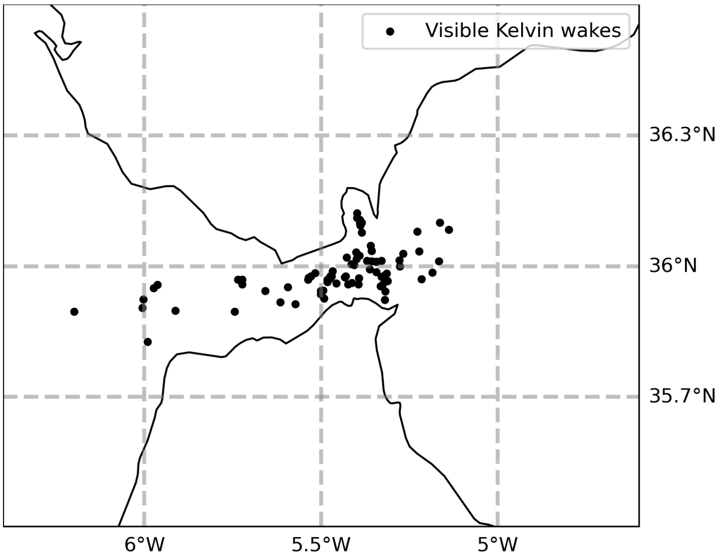

Figure 4.3: Locations of the 81 Kelvin wakes in the Strait of Gibraltar that were visible on Sentinel-2 imagery during July and August 2021.

4.1.2. AIS data

Since January 2005, the International Maritime Organization (IMO) requires most ships to carry transponders that automatically communicate ship information to surrounding ships and coastal authorities [33]. The system is called the Automatic Identification System (AIS). The primary objective of AIS is to increase safety in the marine environment [33]. However, some of the information broadcast by AIS may be relevant for other scientific applications.

The variables broadcast through AIS that are used in this thesis are:

- Longitude
- Latitude
- Speed Over Ground (SOG), given in increments of 0.1 knots
- Course Over Ground (COG), given in increments of 0.1°

The temporal resolution of the system depends on the vessel speed and whether or not the ship is changing course [34]. Open access historical AIS data covering the waters surrounding Denmark is provided by the Danish Maritime Authority [4]. Historical AIS data covering the Strait of Gibraltar is provided by Made Smart Group [21]. It should be noted that in general, AIS data is not open access. Hence, this introduces a limitation to the proposed measurement principle.

4.1.3. High-frequency radar

To validate estimated surface currents in the Strait of Gibraltar, currents derived from High-Frequency Radar (HFR) are used. An HFR transmits electromagnetic waves towards the sea surface. Some part of this signal will be scattered back to the radar through a mechanism called Bragg scattering [31]. The Doppler shift in this return signal is a measure of the surface current in the radar's line-of-sight. By measuring line-of-sight surface currents from multiple HFRs, total surface currents may be reconstructed. In the Strait of Gibraltar, three HFRs are operated by Puertos del Estado. Together, they provide hourly estimates of east- and northward components of surface currents in the Strait of Gibraltar, with a spatial resolution of approximately 1×1 km [31]. Data from July and August of 2021 is downloaded from [16]. In Figure 4.4 an example of the spatial coverage of the HFR data is given.

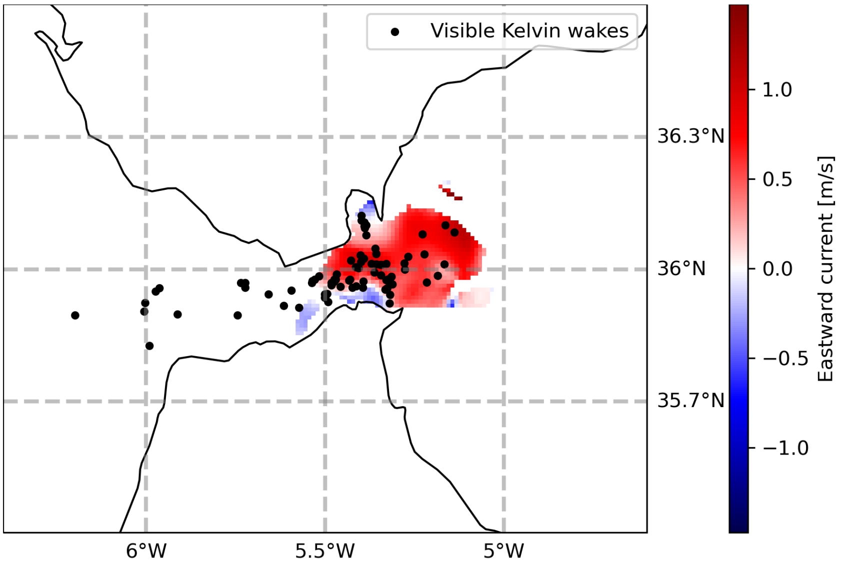

Figure 4.4: Map of eastward currents derived from High-Frequency Radar in the Strait of Gibraltar on 19th of August 2021 10:00 AM.

4.1.4. Modelled currents

DCSM

In order to validate the estimated surface currents in the North Sea and Kattegat strait, modelled currents derived from the Dutch Continental Shelf Model (DCSM) are used. The DCSMv6 is a 2D hydrodynamic model covering the North Sea and adjacent waters with a structured uniform grid [53]. Since the model is 2-dimensional, it only provides depth-averaged currents. The spatial resolution in east-west direction is 1/40°, while it is 1/60° in north-south direction. For the North Sea part of the model, the temporal resolution was 10 minutes. For the Kattegat strait, the temporal resolution was 1 hour.

CMEMS

A second source of validation data in the Strait of Gibraltar is provided by modelled currents from the Copernicus Marine Environment Monitoring Service (CMEMS). They provide a hydrodynamic model for the Mediterranean basin with a spatial resolution of $4\,\mathrm{km} \times 4\,\mathrm{km}$, temporal resolution of 15 minutes and 141 vertical levels [7]. Data were acquired from [8].

4.2. Methods

To compute the along- and across-ship surface currents using Equations 1.1 and 1.2, four variables need to be determined: V_{SOG}, θ_{COG}, V_{STW} and θ_{CTW}. The first two are derived from a ship's AIS transponder, while the last two are derived from an image of a ship's Kelvin wake. First, each Kelvin wake image was manually matched to the corresponding ship's AIS data. Figure 4.5 shows an example of a ship track according to its AIS transponder. The red arrow represents the ship's location on the Sentinel-2 image. The green dots highlight the AIS data points that are spatially contained within the Kelvin wake. The ship's V_{SOG} and θ_{COG} were computed by taking their median over these green points. The reason for this is discussed in Section 5.2.1.

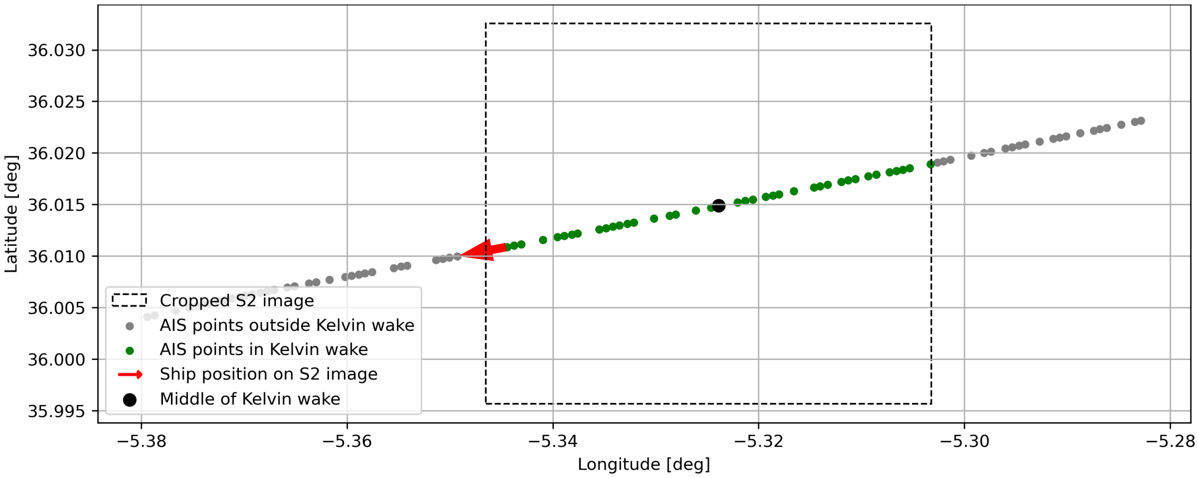

Figure 4.5: Example of a ship track derived from AIS data. Gray and green dots correspond to AIS data points, with the green points overlapping with the Kelvin wake. The red arrow represents the ship position on the Sentinel-2 (S2) image. The black dot denotes the middle of the Kelvin wake, which is used for spatial interpolation of validation data sets. The dashed box represents the boundaries of the cropped S2 image.

To find the last two unknowns, V_{STW} and θ_{CTW}, the algorithm from Chapter 3 was run for each Kelvin wake image. To run the algorithm, candidate parameter sets for V_{STW} and θ_{CTW} had to be defined. In order to save computation time, the V_{SOG} and θ_{COG} derived from AIS data were used to narrow the parameter set that had to be considered. This resulted in the following settings:

$$\begin{aligned} \theta_{\text{CTW,min}} &= \theta_{\text{COG}} - 20, & V_{\text{STW,min}} &= \max(6, V_{\text{SOG}} - 2), \\ \theta_{\text{CTW,max}} &= \theta_{\text{COG}} + 20, & V_{\text{STW,max}} &= V_{\text{SOG}} + 2, \\ \Delta\theta_{\text{CTW}} &= 0.1^\circ, & \Delta V_{\text{STW}} &= 0.01\,\text{m}\,\text{s}^{-1}. \end{aligned} \tag{4.1}$$

The fitting algorithm presented in Chapter 3 returns estimates for V_{STW} and θ_{CTW}. Evaluation of Equations 1.1 and 1.2 yields estimates of the along- and across-ship components of the surface current.

Subsequently, the estimated surface currents were compared to validation data sets. These validation data sets provide east and north currents that need to be interpolated in time and space to an appropriate location and timestamp. The black point in Figure 4.5 approximates the center of the Kelvin wake. This point was chosen as the representative location of the estimated surface current. Hence, this point is used for spatial interpolation of the validation data sets. Similarly, the average timestamp between the first and last green point in Figure 4.5 was taken as the appropriate timestamp to which validation data sets were temporally interpolated. For the data points in the North Sea and Kattegat, the only validation data set consisted of modelled currents from the Dutch Continental Shelf Model (DCSM). Those currents were bilinearly interpolated in space. In the Strait of Gibraltar, two validation data sets were used: observations derived from High-Frequency Radar (HFR) and modelled currents from the Copernicus Marine Environment Monitoring Service (CMEMS). Since the HFR dataset contains some missing data in space, nearest-neighbour interpolation was used in space for both datasets to avoid exceptions that would be introduced in more accurate interpolation methods. In all cases, temporal interpolation was performed linearly. Finally, the interpolated east and north currents were reprojected into each ship's frame of reference using

$$U_{\text{along}} = U_{\text{east}} \cos(\theta_{\text{COG}}) + U_{\text{north}} \sin(\theta_{\text{COG}}), \tag{4.2}$$

$$U_{\text{across}} = U_{\text{east}} \sin(\theta_{\text{COG}}) - U_{\text{north}} \cos(\theta_{\text{COG}}). \tag{4.3}$$

4.3. Results

4.3.1. Along-ship component

For the datapoints in the North Sea and Kattegat strait, the computed surface currents were compared with depth-averaged currents from the DCSM. In Figure 4.6 the resulting comparison is shown for the along-ship component of the currents. There is excellent agreement, with 82% of variance explained by the linear fit. Furthermore, the Root-Mean-Square-Error (RMSE) is only $0.05\,\mathrm{m\,s^{-1}}$. This is especially remarkable considering the fact that surface currents are being correlated with depth-averaged currents.

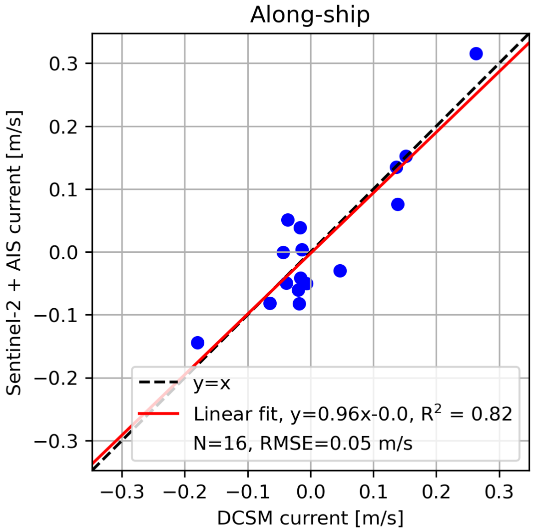

Figure 4.6: Correlation of estimated along-ship surface currents with depth-averaged currents from the DCSM for data points in the North Sea and Kattegat Strait.

However, the comparison with DCSM is only a validation with respect to modelled data. It is desirable to validate the methodology with observations instead. In the Strait of Gibraltar, a pair of High-Frequency Radars (HFR) provides indirect observations of surface currents. In two months of Sentinel-2 imagery, 81 visible Kelvin wakes were found. In 4 cases, no HFR data was available on that particular day. In another 24 cases, the ships did not spatially overlap with the HFR data (see Figure 4.4). Hence, only 53 data points could be compared to the HFR currents. Moreover, the data points were also compared with modelled surface currents from CMEMS. There was no missing CMEMS data, hence all 81 data points could be compared to the modelled currents.

In Figure 4.7 the three datasets are correlated against each other for the along-ship component of the surface current. The red lines correspond to least-squares fits of the data points. In general, there is good agreement between the three datasets. The correlation between the Sentinel-2+AIS currents and HFR observations is largest, with 95% of variance explained by the least squares fit. The fit between Sentinel-2+AIS currents and CMEMS currents explains 88% of variance while 87% of variance is explained in the fit between CMEMS and HFR. Some of the datapoints in the top right of Figure 4.7b do not show up in the other 2 panels. This is because of the missing HFR data.

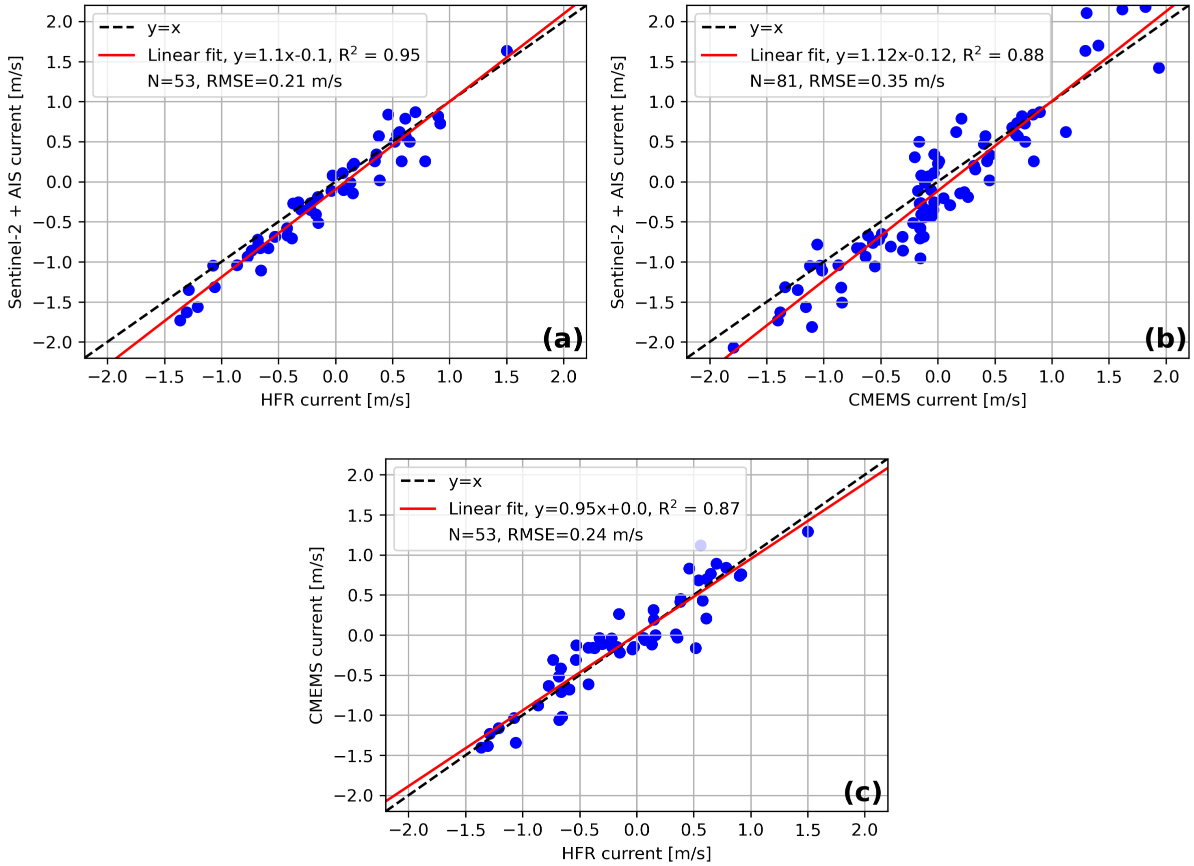

Figure 4.7: Correlation between three datasets of along-ship surface currents in the Strait of Gibraltar. a) Sentinel-2+AIS vs. High-Frequency Radar (HFR). b) Sentinel-2+AIS vs. numerical model CMEMS. c) CMEMS vs. HFR.

The RMSE of the S2+AIS currents with respect to the HFR is $0.21\,\mathrm{m\,s^{-1}}$. This is considerably larger than for the data points in the North Sea. This may partially be explained by the fact that the ships in the Strait of Gibraltar are undergoing more variations in speed and course than the ships in the North Sea and Kattegat. This effect is analyzed in Section 5.2.1. Figure 5.5 shows boxplots of standard deviations in V_{SOG} and θ_{COG}. The median standard deviation in V_{SOG} increases from $0.05\,\mathrm{m\,s^{-1}}$ in the North Sea/Kattegat to $0.13\,\mathrm{m\,s^{-1}}$ in the Strait of Gibraltar. Since the along-ship currents depend linearly on V_{SOG}, the same magnitude of uncertainty is introduced into the surface current. Another factor that may explain the difference in accuracy between the study areas is the difference in accuracy between DCSM and HFR-derived currents. In Table 4.1 some statistics on the errors of the Sentinel-2+AIS dataset with respect to the validation datasets are summarized.

Table 4.1: Error statistics of the estimated along-ship surface currents with respect to validation datasets.

Study area	Validation dataset	N	Bias [$\mathrm{m\,s^{-1}}$]	SD [$\mathrm{m\,s^{-1}}$]	RMSE [$\mathrm{m\,s^{-1}}$]	max [$\mathrm{m\,s^{-1}}$]
North Sea/Kattegat	DCSM	16	0	0.05	0.05	0.09
Strait of Gibraltar	HFR	53	-0.11	0.18	0.21	0.38
Strait of Gibraltar	CMEMS	81	-0.12	0.33	0.35	0.80

4.3.2. Across-ship component

In Figure 4.8 the across-ship currents for data points in the North Sea/Kattegat study area are compared with depth-averaged currents from DCSM. Although there is still some agreement, the correlation has decreased with respect to the along-ship component of the surface current. This can be seen by the R^2 value that has decreased from 0.82 to 0.64. Furthermore, the RMSE has increased from $0.05\,\mathrm{m\,s^{-1}}$ to $0.10\,\mathrm{m\,s^{-1}}$.

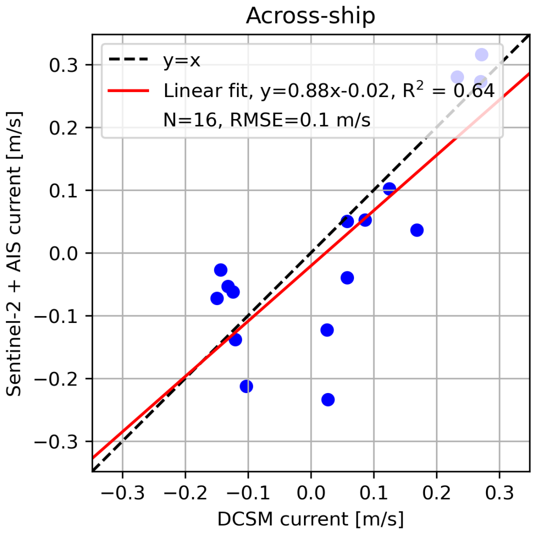

Figure 4.8: Correlation of Sentinel-2+AIS across-ship surface currents with depth-averaged currents from the DCSM for data points in the North Sea and Kattegat Strait.

Considering the second study area, in Figure 4.9 the three datasets are correlated against each other for the across-ship component of the surface current. Although there is a clear correlation between all three datasets, there are large outliers and the correlation is generally worse than for the along-ship currents. Note that the sample size is larger in Figure 4.9b, since this comparison does not suffer from missing data in the HFR dataset.

The worse quality of the across-ship currents may be explained by the fact that their estimation is more sensitive to the angular difference between the two ship speed vectors, i.e., $\theta_{\text{COG}} - \theta_{\text{CTW}}$, than the along-ship component. This can be seen mathematically by differentiating Equations 1.1 and 1.2 with respect to the angular difference. Let $\gamma = \theta_{\text{COG}} - \theta_{\text{CTW}}$. Differentiation of both equations with respect to γ yields

$$\frac{\partial U_{\text{along}}}{\partial \gamma} = -V_{\text{SOG}} \sin(\gamma), \tag{4.4}$$

$$\frac{\partial U_{\text{across}}}{\partial \gamma} = V_{\text{SOG}} \cos(\gamma). \tag{4.5}$$

Since $\gamma << 1$, $\sin(\gamma) \approx \gamma$ and $\cos(\gamma) \approx 1 - \frac{\gamma^2}{2}$. Substitution of these approximations leads to

$$\frac{\partial U_{\text{along}}}{\partial \gamma} \approx -V_{\text{SOG}}\gamma, \tag{4.6}$$

$$\frac{\partial U_{\text{across}}}{\partial \gamma} \approx V_{\text{SOG}} \left(1 - \frac{\gamma^2}{2}\right). \tag{4.7}$$

Clearly, $V_{\text{SOG}}(1 - \frac{\gamma^2}{2}) > V_{\text{SOG}}|\gamma|$ for small γ. Therefore, the across-ship component of the surface current is more sensitive to the angular difference between the ship speed vectors than the along-ship component. In Figure 5.5 it is shown that the median standard deviation in θ_{COG} is $0.7°$ for ships in the Strait of Gibraltar. According to Equation 4.7, at a ship speed of $10\,\mathrm{m\,s^{-1}}$, a change of $0.7°$ in the angular difference between the ship speed vectors already leads to a change of $0.12\,\mathrm{m\,s^{-1}}$ in the across-ship surface current. In Figure 4.9 the datapoints corresponding to a $\sigma_{\theta_{\text{COG}}}$ of more than 2 degrees have been highlighted in red. In the first two figures, the red dots clearly correspond to some of the largest outliers. In Figure 4.9c, which contains no S2+AIS currents, the red dots no longer correspond to the largest outliers. Hence, the variability in θ_{COG} indeed plays a role in the accuracy of the estimated across-ship surface current.

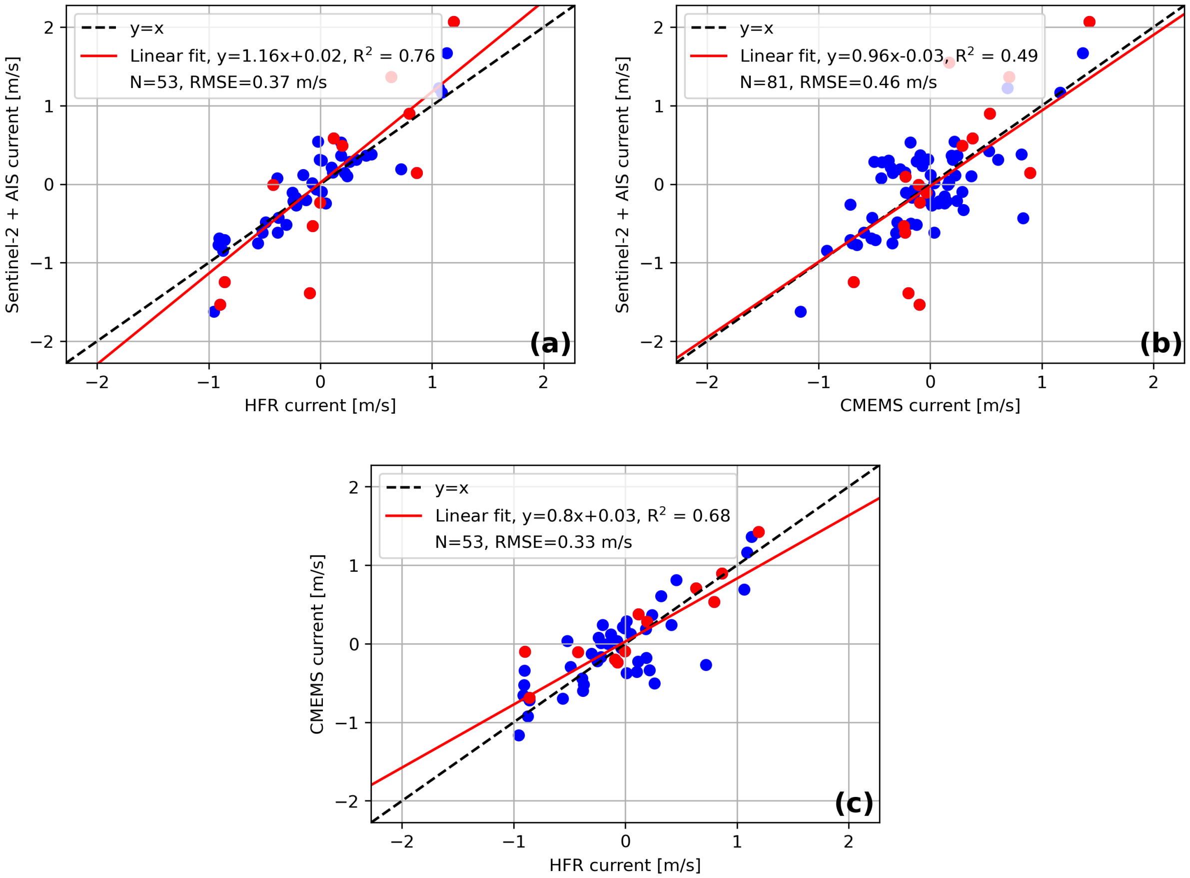

Figure 4.9: Correlation between three datasets of across-ship surface currents in the Strait of Gibraltar. a) Sentinel-2+AIS vs. High-Frequency Radar (HFR). b) Sentinel-2+AIS vs. numerical model CMEMS. c) CMEMS vs. HFR. In all figures, the red dots correspond to datapoints where $\sigma_{\theta_{\text{COG}}} > 2°$.

For quality control purposes, ships can be filtered by the standard deviation in θ_{COG}. In Figure 4.10, only data points where the ship's $\sigma_{\theta_{\text{COG}}}$ was less than $2°$ are included. The RMSE for the top two panels has now lowered with respect to Figure 4.9, while it remains similar for the bottom panel. This makes sense as the bottom panel does not contain S2+AIS data, which is the only dataset that is sensitive to $\sigma_{\theta_{\text{COG}}}$. The RMSE of the S2+AIS across-ship currents with respect to HFR now becomes $0.24\,\mathrm{m\,s^{-1}}$, which is only $0.03\,\mathrm{m\,s^{-1}}$ larger than the RMSE for the along-ship surface current. However, the disadvantage of filtering is that the sample size has decreased from 53 to 41 datapoints. In Table 4.2 some statistics on the errors of the Sentinel-2+AIS dataset with respect to the validation datasets are summarized.

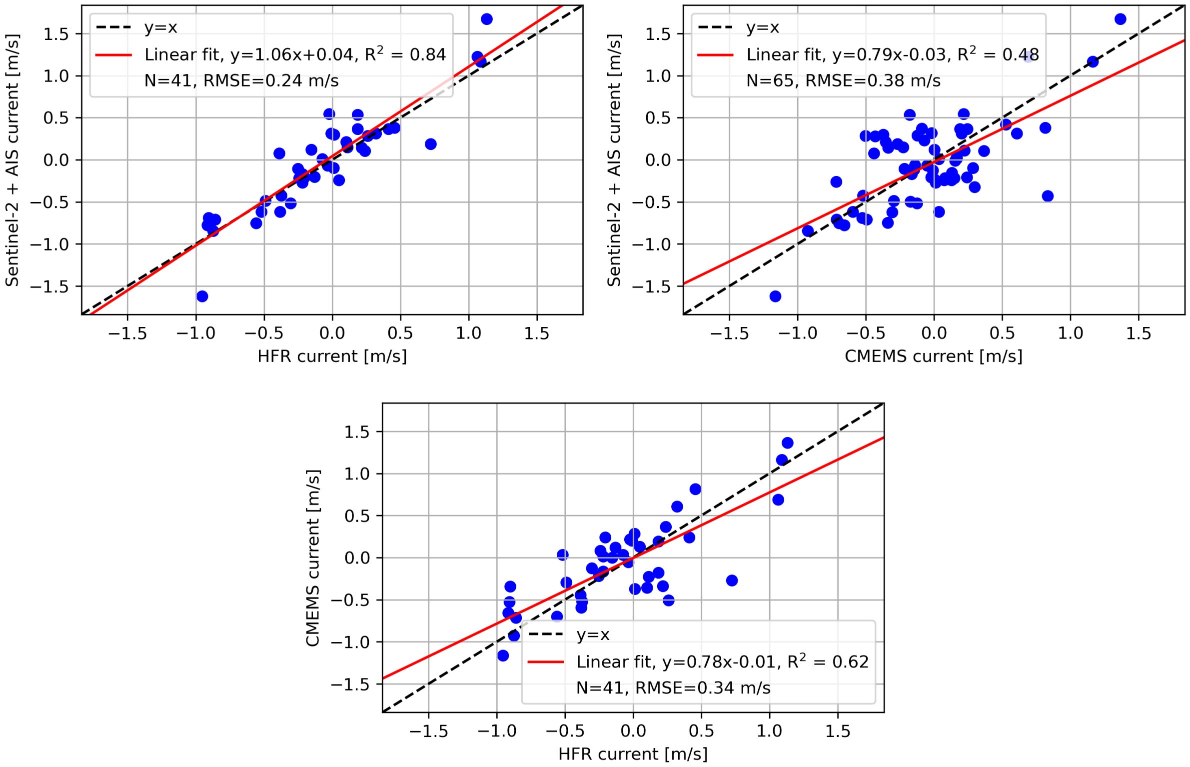

Figure 4.10: Correlation between three datasets of across-ship surface currents in the Strait of Gibraltar after filtering for ships with $\sigma_{\theta_{\mathrm{COG}}}$. a) Sentinel-2+AIS vs. High-Frequency Radar (HFR). b) Sentinel-2+AIS vs. numerical model CMEMS. c) CMEMS vs. HFR.

Table 4.2: Error statistics of the estimated across-ship surface currents with respect to validation datasets.

Study area	Validation dataset	Filter	N	Bias [$\mathrm{m\,s^{-1}}$]	SD [$\mathrm{m\,s^{-1}}$]	RMSE [$\mathrm{m\,s^{-1}}$]	max [$\mathrm{m\,s^{-1}}$]
North Sea	DCSM	-	16	-0.02	0.10	0.10	0.12
Gibraltar	HFR	-	53	0.01	0.37	0.37	0.88
Gibraltar	HFR	$\sigma_{\theta_{\mathrm{COG}}} < 2^\circ$	41	0.04	0.24	0.24	0.57
Gibraltar	CMEMS	-	81	-0.03	0.46	0.46	1.38
Gibraltar	CMEMS	$\sigma_{\theta_{\mathrm{COG}}} < 2^\circ$	65	-0.02	0.38	0.38	0.79

4.3.3. Vector representation

In this section, the estimated surface currents are compared in the spatial domain. Figure 4.11 visualizes the surface currents in the Strait of Gibraltar on 4 different days. The red vectors correspond to the Sentinel-2+AIS estimates. The black vectors denote the currents derived from High-Frequency Radar (HFR), while the CMEMS modelled vector field is visualized by the blue vectors. In general, the agreement between Sentinel-2+AIS and HFR is excellent in magnitude and direction. The largest deviation is seen at the rightmost red vector in Figure 4.11d, where the direction disagrees by about 60°. The modelled currents from CMEMS deviate substantially from the other two datasets. This is especially clear in the eastern half of Figure 4.11d, where some blue and black vectors are orthogonal to each other.

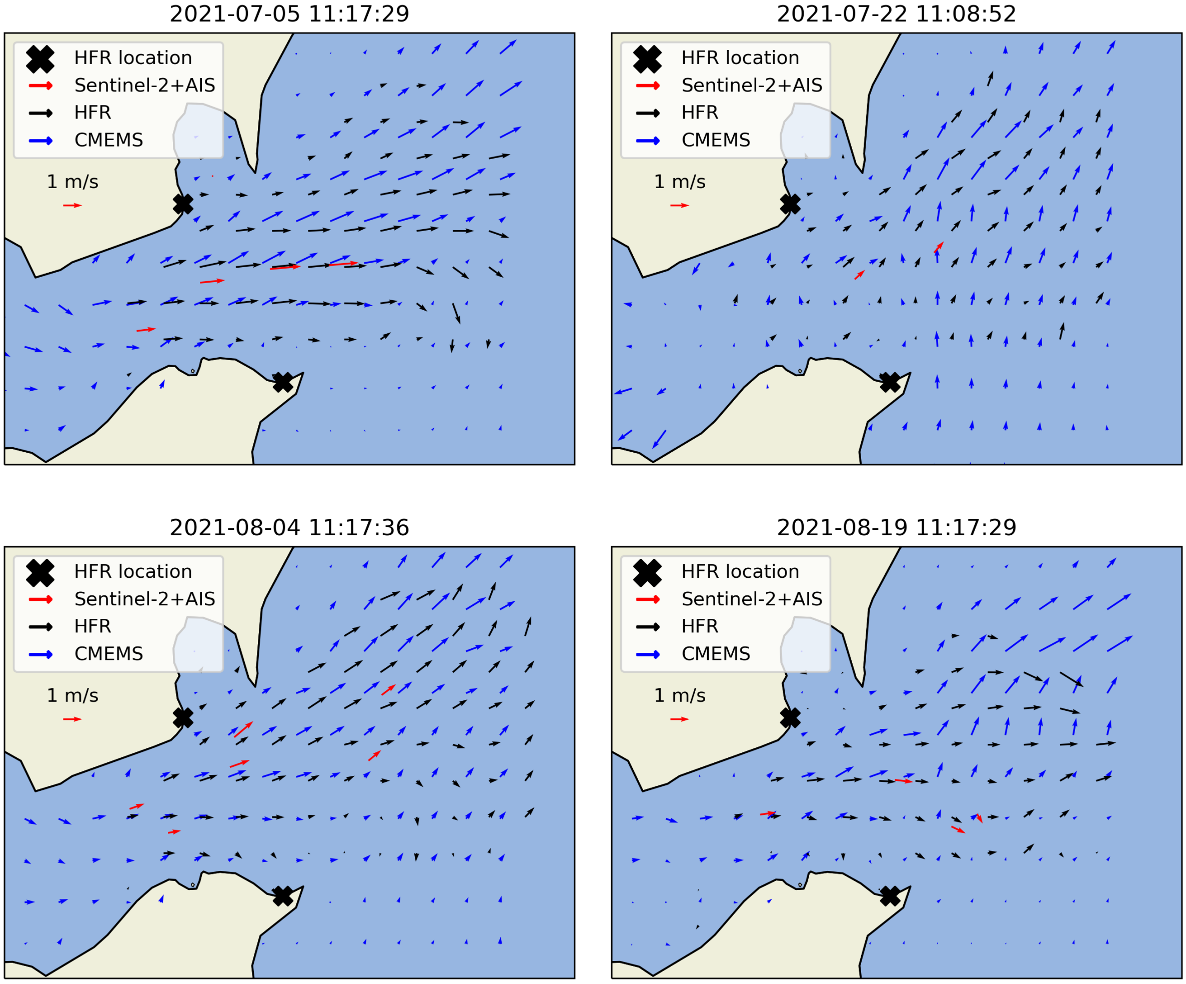
2021-07-05 11:17:29

2021-07-22 11:08:52

2021-08-04 11:17:36

2021-08-19 11:17:29

Figure 4.11: Surface currents in the Strait of Gibraltar. The red arrows visualize the estimated Sentinel-2+AIS surface currents, while the black arrows represent the vector field derived from High-Frequency Radar (HFR). The modelled currents from CMEMS are given by the blue vectors. The black crosses denote the locations of the HF radars.

4.3.4. Convergence angle correction

In Section 3.3, a correction to θ_{CTW} was introduced to correct for the difference between grid and true north. This correction has been applied to obtain the results from the previous sections, however the actual effect of the correction is discussed here. According to Equation 4.6, the along-ship component of the surface current is not sensitive to the angular difference $\theta_{\text{COG}} - \theta_{\text{CTW}}$. Thus, a small correction in θ_{CTW} alone should not have a large effect on this component. In Figure 4.12 it can indeed be seen that the convergence angle correction has negligible effect on the quality of the estimated along-ship surface currents.

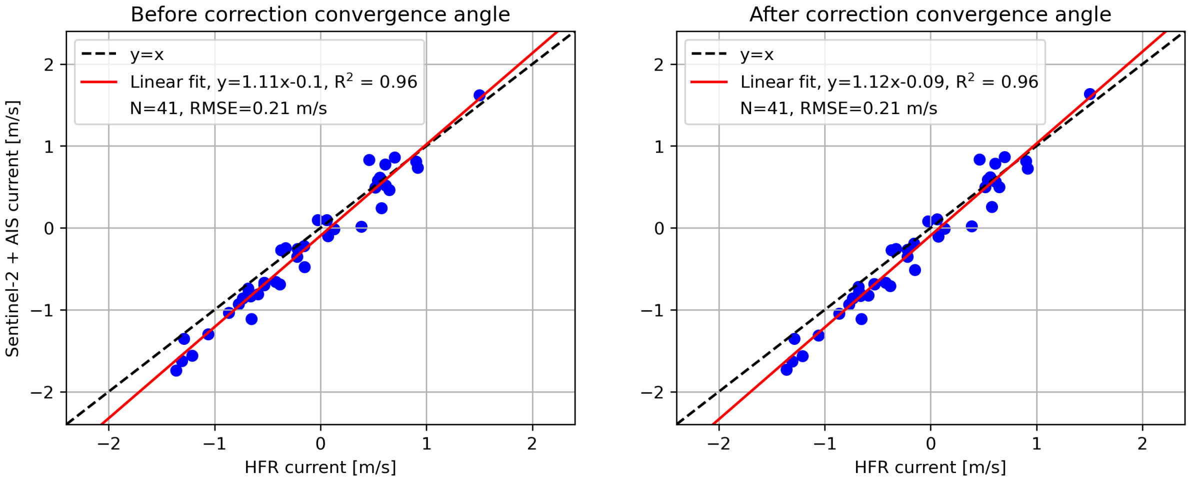

Figure 4.12: a) Correlation of Sentinel-2+AIS along-ship components of surface currents with High-Frequency Radar (HFR) observations, without correcting the estimated θ_{CTW} for the convergence angle between grid and true north. b) Same as a), after correcting for the convergence angle.

However, since the across-component of the surface current is more sensitive to the angular difference $\theta_{\text{COG}} - \theta_{\text{CTW}}$, the convergence angle correction becomes relevant. In Figure 4.13a, a bias of $0.27\,\mathrm{m\,s^{-1}}$ is observed before applying the convergence angle correction. In Figure 4.13b, the bias has reduced to $0.04\,\mathrm{m\,s^{-1}}$. Therefore, it is indeed necessary to apply the convergence angle correction to accurately estimate the across-ship surface currents.

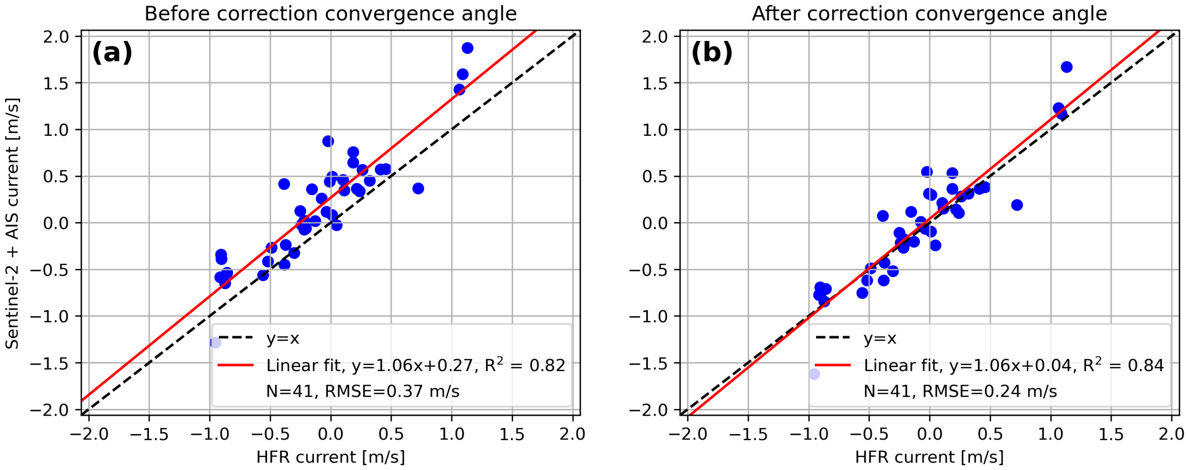

Figure 4.13: a) Correlation of Sentinel-2+AIS across-ship components of surface currents with High-Frequency Radar (HFR) observations, without correcting the estimated θ_{CTW} for the convergence angle between grid and true north. b) Same as a), after correcting for the convergence angle.

5

Error analysis

This chapter covers the quantification of errors introduced in the surface current retrieval algorithm. First, Section 5.1 will assess the validity of two assumptions made in the derivation of the spectral Kelvin wake model. Thereafter, in Section 5.2 the errors in the four ship speed and direction variables are estimated individually. Then, they are propagated into the estimated surface currents using a first-order Taylor series expansion. Finally, an alternative method to quantify the uncertainty in the estimated surface currents by comparing them with two independent surface current datasets is given in Section 5.3.

5.1. Model error

5.1.1. Intermediate depth

The results obtained in Chapter 4 all depend on the use of the deep water approximation to derive the forward model for the spectral Kelvin wake signal. In this section, the applicability of this approximation will be verified using bathymetry data. Thereafter, the Kelvin wake model will be extended to include depth effects. It will then be assessed if application of this more general model leads to better results for those ships where the deep water approximation was not strictly applicable.

For each Kelvin wake image in both study areas, the depth-to-wavelength ratio was computed. The depth was computed using bilinear interpolation of the bathymetry data. The wavelength was computed following Equation 2.34. For all datapoints in the Strait of Gibraltar, the depth-to-wavelength ratio was larger than 0.5, justifying the use of the deep water approximation. However, for one datapoint in the Kattegat strait, a depth-to-wavelength ratio of 0.40 was computed, hence the deep water approximation may not be appropriate in that case.

The spectral model from Section 2.2 will now be extended to include depth effects. To find the spectral shape, we would like to reorder Equation 2.30 to a form such that $k_y = f(k_x; V_{\text{STW}}, h)$. However, due to the $\tanh(\cdot)$ term, it is not possible to derive an explicit formula for k_y. Therefore, the equation will be reordered to an implicit equation after which a solution will be estimated using an iterative approach. An implicit reordering of Equation 2.30 is given by

$$k_y = \pm k_x \sqrt{\frac{V_{\text{STW}}^4}{g^2 \tanh(kh)} k_x^2 - 1}. \tag{5.1}$$

Subsequently, the solution to the above equation is approached using Algorithm 1, where the superscript for k_y denotes the iteration number.

Algorithm 1 Iterative estimation solution Equation 5.1

```
$k_y^0 = 0$
while $||k_y^i - k_y^{i-1}||_2 > 1 \times 10^{-3}$ do
    $k_y^{i+1} = k_x \left( V_{\text{STW}}^4 k_x^2 \left( g^2 \tanh\left( \sqrt{(k_x^2 + (k_y^i)^2)h} \right) \right)^{-1} - 1 \right)^{\frac{1}{2}}$
end while
```

In Figure 5.1 the estimated solutions to Equation 5.1 are shown, alongside with the solutions obtained after deep water approximation. In these figures, the wavelength of the Kelvin wake is fixed and corresponds to a ship with $V_{\text{STW}} = 9\,\text{m}\,\text{s}^{-1}$. The local water depth is varied to explore the sensitivity of the spectral shape to the depth-to-wavelength ratio. For depth-to-wavelength ratios of 0.4 and 0.3, the difference between the two models is small and manifests itself in waves travelling in a similar direction as the ship. At smaller depth-to-wavelength ratios, the difference between the two models becomes significant, indicating that incorrect usage of the deep water approximation could lead to large errors in estimating a ship's speed through water from its Kelvin wake spectrum.

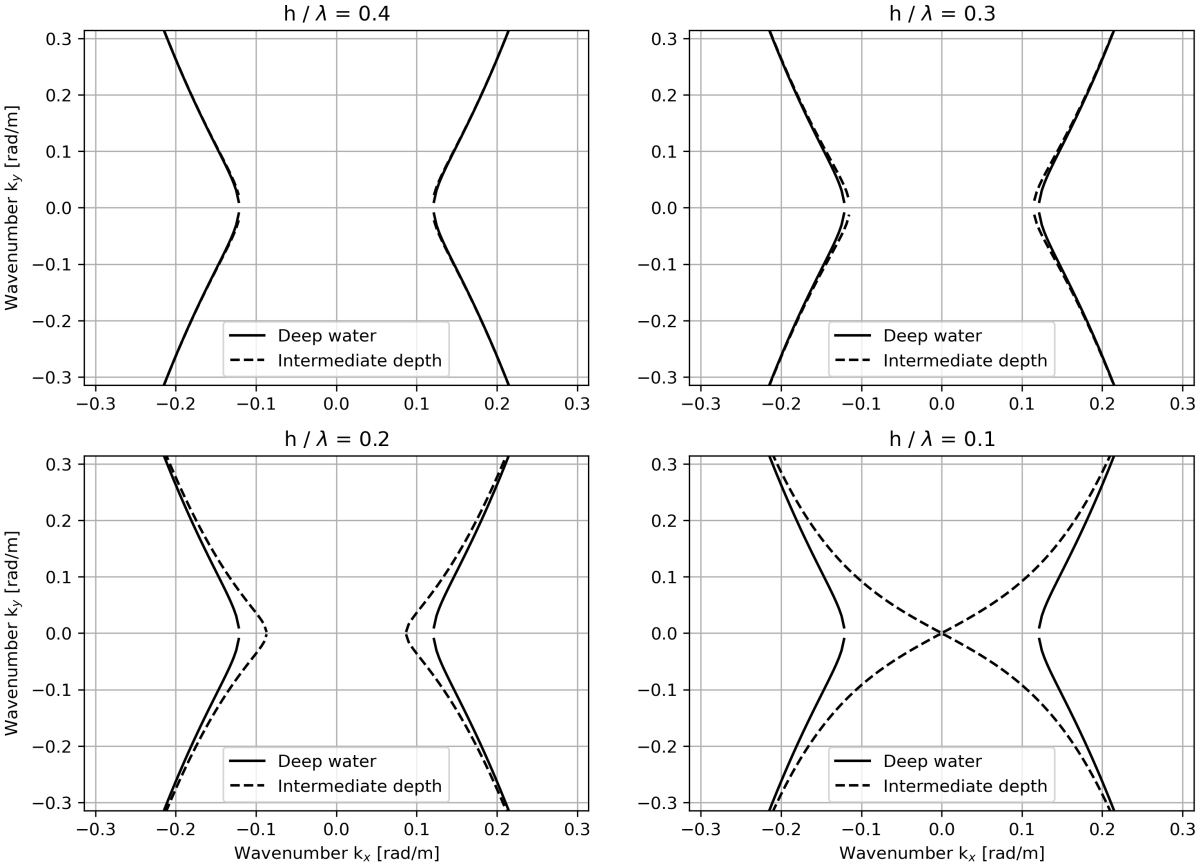

Figure 5.1: Comparison between theoretical spectrum Kelvin wake with and without deep water approximation, for different water depth-to-wavelength ratios ($\frac{h}{\lambda}$). Solid lines correspond to the solution of Equation 2.32, while the dashed lines correspond to an estimated solution of Equation 5.1.

For the data point with a depth-to-wavelength ratio of 0.4, the algorithm from Chapter 3 was ran with the extended forward model using the local water depth derived from the bathymetry dataset. The resulting fits for V_{STW} and θ_{CTW} did not change, which indicates that for this application, the deep water approximation can still be used at a depth-to-wavelength ratio of 0.4. However, if the methodology is implemented into an operational system, one should be aware of the implications of a small depth-to-wavelength ratio.

In Figure 5.2 the implications of combinations of ship speed and water depth are visualized. The shaded green area shows all combinations of ship speed and water depth for which surface current retrieval is possible with Sentinel-2 imagery. The shaded yellow area shows the combinations for which surface current retrieval may be possible if the local bathymetry is taken into account. Furthermore, if higher resolution imagery were to be used, the dashed red line would be lowered. This would increase the shaded green area.

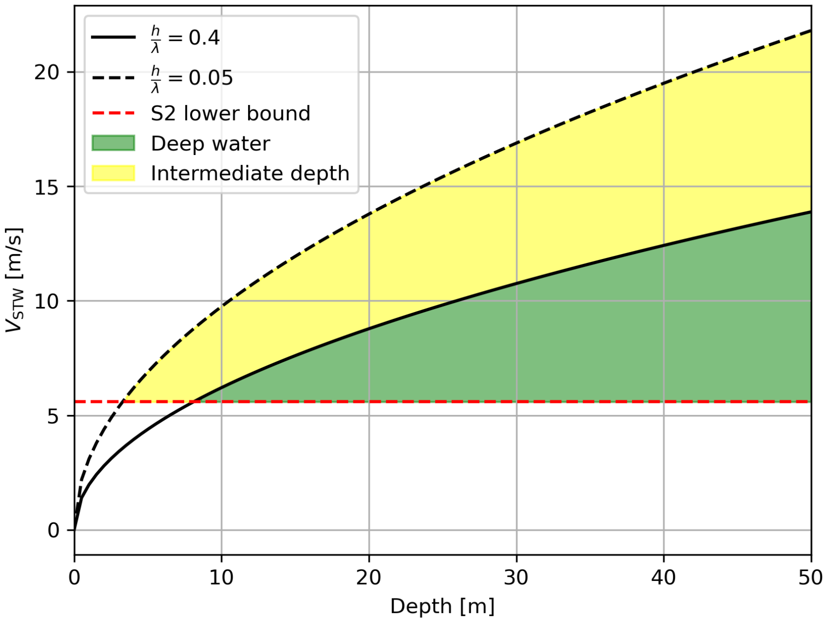

Figure 5.2: Relationship between ship speed through water (V_{STW}) and local water depth at two different depth-to-wavelength ratios. The shaded green area indicates where the deep-water approximation is valid, while the local water depth needs to be taken into account in the shaded yellow area. The dashed red line gives a lower bound for the ship speed through water due to the spatial resolution of Sentinel-2.

5.1.2. Stokes waves

Another assumption that was made in Section 2.2 was that linear wave theory is appropriate to describe the propagation of Kelvin waves. Linear wave theory is applicable if the wave steepness is small, i.e., if the ratio between the wave amplitude and wavelength is small [48]. Stokes developed an approach to derive higher-order corrections to the linear wave theory which are useful if wave steepness increases. At third order, the deep water dispersion relation becomes [48]

$$\omega^2 = gk(1 + k^2a^2), \tag{5.2}$$

where a represents the wave amplitude. Compared to the linear case (Equation 2.27), the k^2a^2 term is introduced. It is precisely this term that represents the steepness of a wave. For a small amplitude long wave, this term approaches zero and the linear case is recovered. By introducing the apparent frequency shift due to a moving frame of reference as in Section 2.2 and reordering, an explicit equation of the form $k_y = f(k_x, V_{\text{STW}}, a)$ can be derived. In Figure 5.3 the resulting spectral shape is compared to the spectral shape in the deep water case. It can be seen that differences are small until wave amplitudes exceed $0.5\,$m.

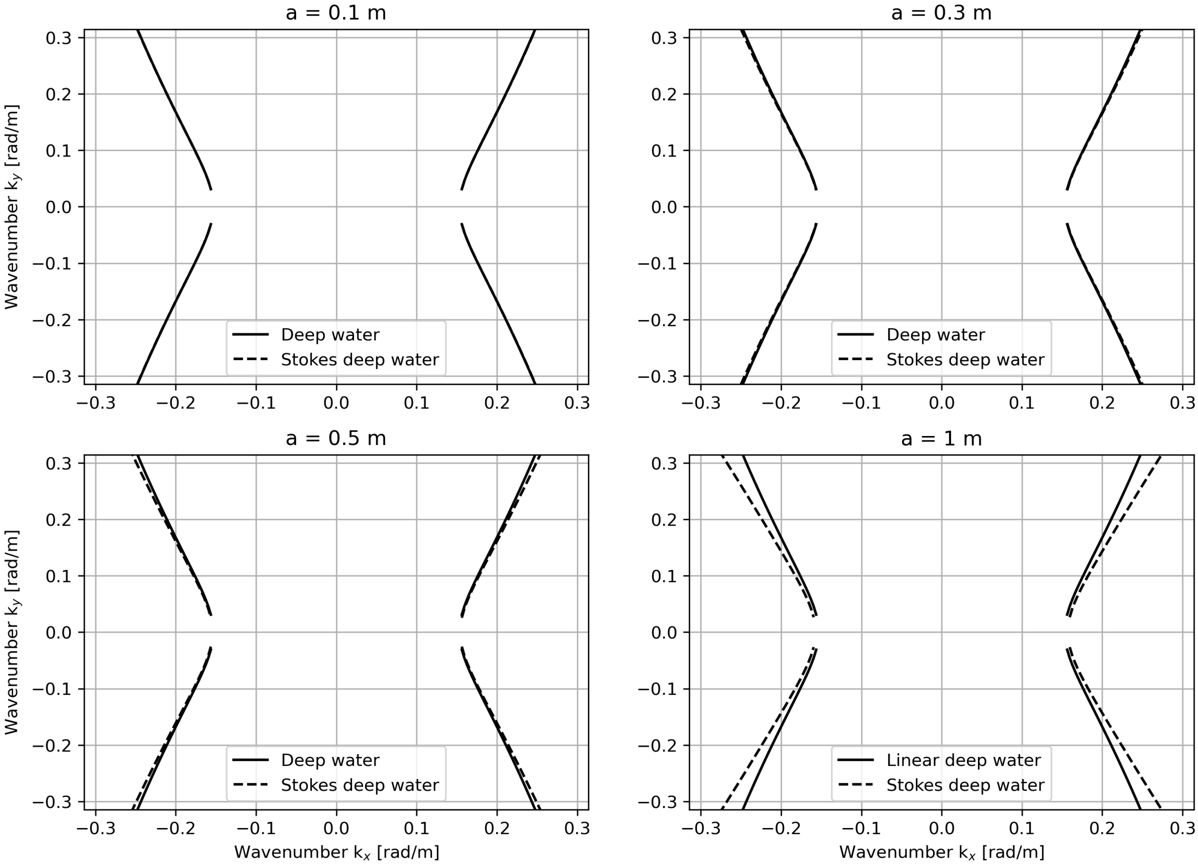

Figure 5.3: Comparison between theoretical spectrum Kelvin wake using linear wave theory and a third order Stokes wave, both in deep water. Solid lines correspond to the solution of Equation 2.32, while the dashed lines correspond to the solution of Equation 5.2 with amplitudes of 0.1, 0.3, 0.5 and $1\,$m.

The wave height of Kelvin waves depends on many factors including the vessel speed, ship geometry and local bathymetry [43]. In [2], several measurements of wave heights from Kelvin wakes are presented. Typically, the wave heights did not exceed $0.2\,$m. However, these measurements were performed about $200\,$m perpendicular to the sailing line. Although wave heights will be larger near the ship, the length of the Kelvin wake is typically in the order of several kilometers. It is therefore expected that in most cases, the average wave height in the Kelvin wake will be small enough such that linear wave theory is appropriate.

5.2. Estimation error

In this section, errors introduced during the estimation process are quantified. In Section 5.2.1 the uncertainties in V_{SOG} and θ_{COG} are quantified. The errors in V_{STW} and θ_{CTW} are estimated in Section 5.2.2. Subsequently, in Section 5.2.3, the individual errors are propagated into the final current estimates using a first-order Taylor series expansion.

5.2.1. Variables derived from AIS data

In this section, the uncertainty in V_{SOG} and θ_{COG} is assessed. As mentioned in Section 4.2, V_{SOG} and θ_{COG} are computed by taking their median values over all AIS data points spatially contained within the Kelvin wake. The median was chosen over the mean as there were many instances where time series of θ_{COG} showed a constant level and a course change. As can be seen in Figure 5.4, the course changes drag the mean away from the constant level while the median is able to extract the constant level. The orientation of the Kelvin wake is a product of all ship courses along the length of the Kelvin wake. The relevant ship course corresponds to the dominant orientation of the Kelvin wake, which is the ship course at which most of the Kelvin has been generated at. Hence, this corresponds to the constant levels shown in Figure 5.4.

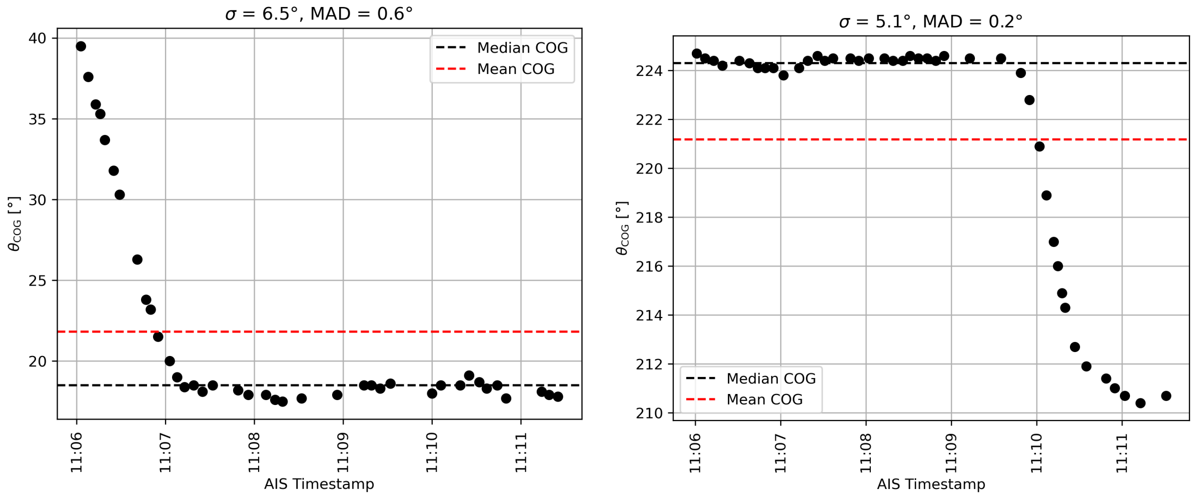

Figure 5.4: Two examples of time series of θ_{COG}. The dashed red lines indicate the mean, while the dashed black lines denote the median level.

To compute the uncertainty in the AIS variables, the standard deviation over all data points could be taken. However, this suffers from the same problem as the mean, since outliers can greatly increase the standard deviation. Therefore, an alternative is to take the Median Absolute Deviation (MAD), which is computed as

$$\text{MAD}(x) = \text{median}(|x_i - \text{median}(x)|). \tag{5.3}$$

In Figure 5.4, it can be seen that indeed the standard deviation is much larger than the MAD due to the course changes. However, these standard deviations do not accurately reflect the uncertainty in the constant level. Therefore, the MAD seems to be more appropriate. Though, to fill the covariance matrix Σ_x in Equation 5.11, estimates for $\sigma^2_{V_{\text{SOG}}}$ and $\sigma^2_{\theta_{\text{COG}}}$ are required. By definition, the median $\pm$ 1 MAD covers 50% of the probability density in a random variable. The mean $\pm$ 1 standard deviation covers about 68% of probability density. Therefore, to use the MAD as an estimator for the standard deviation, this effect has to be corrected for. To that end, it is assumed that at the constant level, V_{SOG} and θ_{COG} are normally distributed random variables. Then, the MAD and standard deviation are related following [40]

$$\sigma \approx 1.4826 \cdot \text{MAD}. \tag{5.4}$$

Hence, by computing the MAD in V_{SOG} and θ_{COG}, the related standard deviations in V_{SOG} and θ_{COG} can be found. In Figure 5.5, the distributions of these standard deviation per study area are shown. It can be seen that the uncertainty in both variables is larger in the Strait of Gibraltar than in the North Sea study area. This indicates that ships in the Strait of Gibraltar are showing more variation in ship speed and ship course than ships in the North Sea study area. The median standard deviations in V_{SOG} in the two study areas are $0.05\,\mathrm{m\,s^{-1}}$ and $0.13\,\mathrm{m\,s^{-1}}$ respectively. The median standard deviations in θ_{COG} in the two study areas are $0.3\,°$ and $0.7\,°$ respectively.

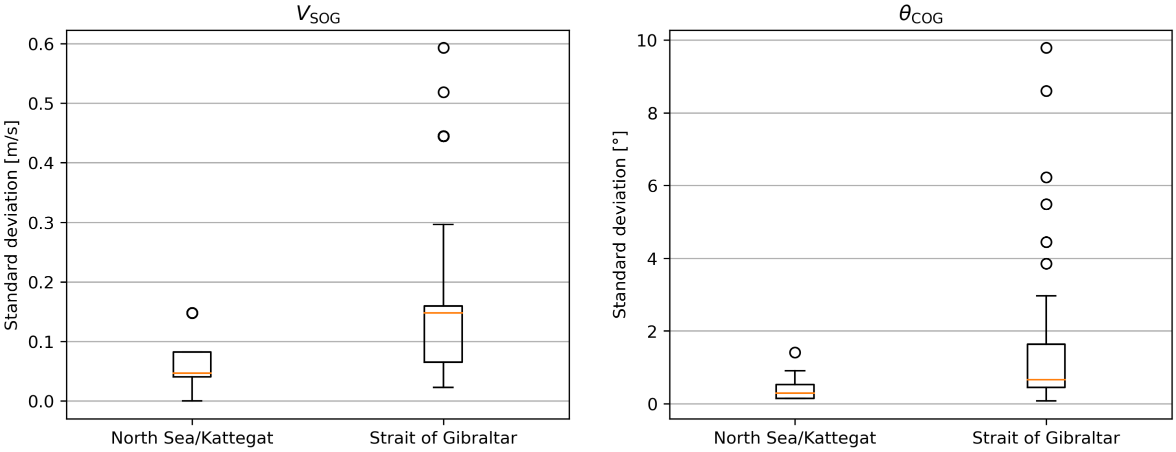

Figure 5.5: a) Distribution of standard deviations in V_{SOG} per study area. b) Distribution of standard deviations in θ_{COG} per study area.

5.2.2. Variables derived from optical imagery

In this section, the uncertainty in V_{STW} and θ_{CTW} is assessed. To that end, the parameter domain obtained after fitting the spectral Kelvin wake model will be useful (see Section 3.2). Intuitively, a well-defined peak in the parameter domain represents a high degree of certainty that the model fit is robust. In contrary, if the peak is more diffuse, the fitted parameters may be quite uncertain. This is illustrated in Figure 5.6, where the figure on the left contains a narrow peak while the figure on the right contains a broad band of parameters that provide a decent fit.

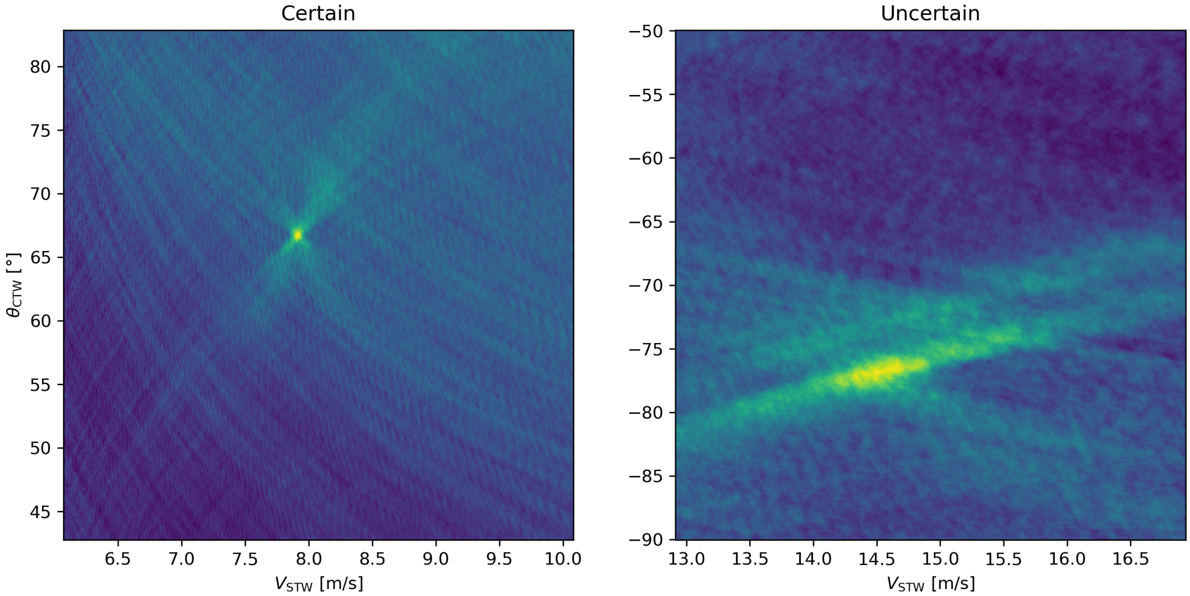

Figure 5.6: Two examples of parameter domains obtained after fitting the spectral Kelvin wake model.

To make the intuitive idea presented above more rigorous, suppose the parameter domain is rescaled such that it represents a log-likelihood function. Assume that $\hat{p}$ is a maximum-likelihood estimator for $p = (V_{\text{STW}}, \theta_{\text{CTW}})$. Then, by Theorem 5.9 in [5], under some regularity conditions, it follows that as the sample size tends to infinity

$$\hat{p} \sim \mathcal{N}(p, I^{-1}(p)), \tag{5.5}$$

where $I(p)$ is the Fisher information for p. The Fisher information can be estimated using the observed Fisher information $\hat{I}(\hat{p})$, which is the same as the negative Hessian of the log-likelihood function evaluated at $\hat{p}$, i.e.,

$$\hat{I}(\hat{p}) = -H(\hat{p}) = -\begin{bmatrix} \frac{\partial^2 l(\hat{p})}{\partial V^2}(\hat{p}) & \frac{\partial^2 l(\hat{p})}{\partial V \partial \theta}(\hat{p}) \\ \frac{\partial^2 l(\hat{p})}{\partial \theta \partial V}(\hat{p}) & \frac{\partial^2 l(\hat{p})}{\partial \theta^2}(\hat{p}) \end{bmatrix}, \tag{5.6}$$

where $H(\cdot)$ denotes the Hessian matrix and $l(\cdot)$ represents the log-likelihood function.

To estimate the Hessian, numerical differentiation of the parameter domain could be performed. However, due to the non-smoothness of the parameter domain and the fact that numerical differentiation amplifies noise, the resulting estimate for the Hessian is unreliable. Therefore, a workaround is to first fit a curve through the parameter domain and use the analytical derivative of the fitted curve instead. However, the typical cross-shaped feature found in the parameter domain does not have a trivial analytical representation. Therefore, the parameter domain is first projected into two one-dimensional domains, one for V_{STW} and one for θ_{CTW}. This is done by taking the maximum along each column and row of the parameter domain, respectively. Subsequently, these projected versions of the parameter domain are rescaled such that their area is 1 to represent a likelihood function. Thereafter, the logarithm is taken to derive the log-likelihood functions as presented in Figure 5.7.

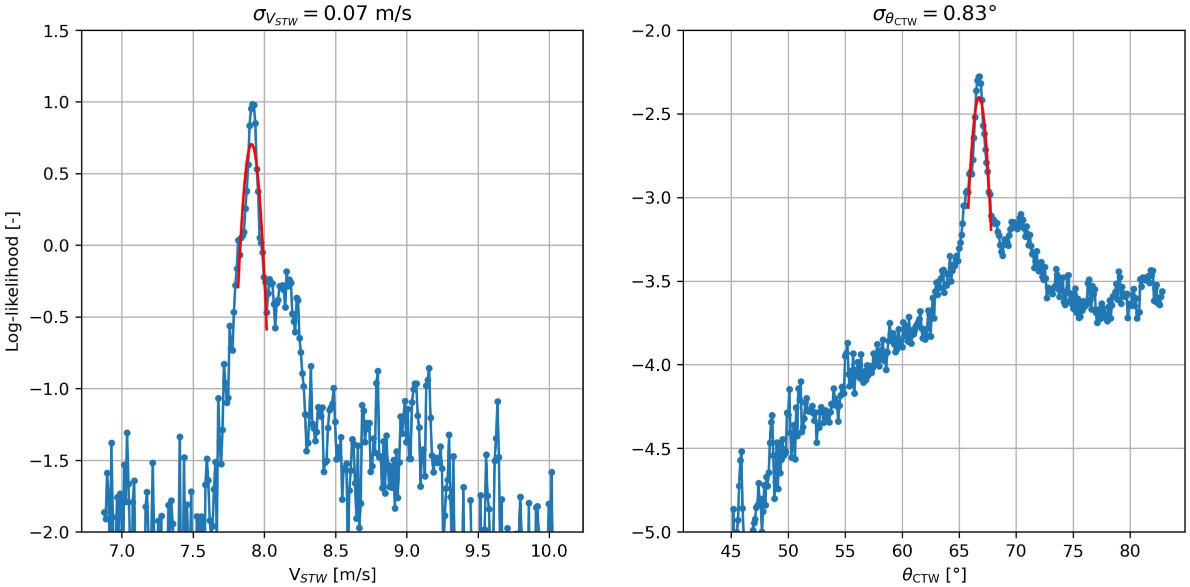

Figure 5.7: One-dimensional projections from the parameter domain in Figure 5.6a. The left figure is obtained by taking the maximum of each column, while the right figure is obtained by taking the maximum of each row. Both figures are rescaled such that they resemble a log-likelihood function. The red lines denote least squares fits of Equation 5.7 to 21 point intervals centered on the fitted parameters $\hat{V}_{\text{STW}}$ and $\hat{\theta}_{\text{CTW}}$.

Subsequently, the following quadratic functions are fitted to 21 point intervals centered on the maximum likelihood estimates:

$$\begin{aligned} l(V_{\text{STW}}) &= a \cdot V_{\text{STW}}^2 + b \cdot V_{\text{STW}} + c, \\ l(\theta_{\text{CTW}}) &= d \cdot \theta_{\text{CTW}}^2 + e \cdot \theta_{\text{CTW}} + f, \end{aligned} \tag{5.7}$$

where a, b, c, d, e and f are constants fitted using ordinary least-squares. The second derivatives of the above equations are given by $2a$ and $2d$, respectively. A large absolute value of a or d indicates that the curvature in the log-likelihood function is large. This corresponds to a well-defined peak. Therefore, the fitted parameter should be more certain. A quantification of the uncertainty follows from one-dimensional equivalents of Equation 5.6, i.e.,

$$\begin{aligned} \sigma_{V_{\text{STW}}} &= \sqrt{-\left(\frac{\partial^2 l(\hat{V})}{\partial V^2}\right)^{-1}} = \sqrt{-\frac{1}{2a}}, \\ \sigma_{\theta_{\text{CTW}}} &= \sqrt{-\left(\frac{\partial^2 l(\hat{\theta})}{\partial \theta^2}\right)^{-1}} = \sqrt{-\frac{1}{2d}}. \end{aligned} \tag{5.8}$$

In Figure 5.8 the distributions of estimated standard deviations per study area are shown. It can be seen that there is one large outlier where $\sigma_{\theta_{\text{CTW}}} = 15.1°$. This corresponds to a data point where no good parabolic fit was possible, as shown in Figure 5.8c. The median standard deviations in V_{STW} in the two study areas are $0.10\,\text{m}\,\text{s}^{-1}$ and $0.15\,\text{m}\,\text{s}^{-1}$ respectively. The median standard deviations in θ_{CTW} in the two study areas are $1.1\,°$ and $1.3\,°$ respectively.

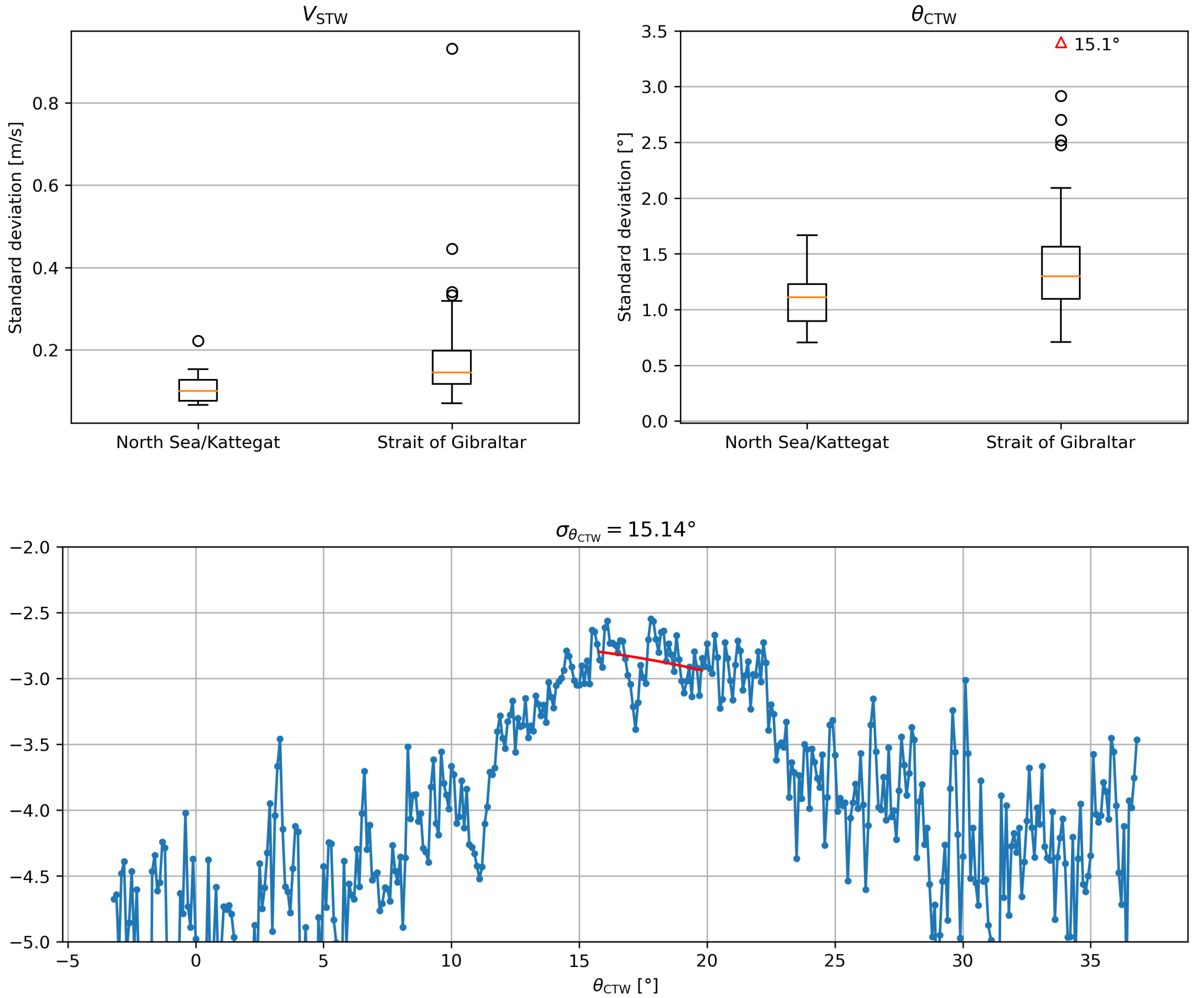

Figure 5.8: a) Distribution of standard deviations in V_{STW} per study area. b) Distribution of standard deviations in θ_{CTW} per study area. The red triangle represents an outlier of 15.1°. c) One-dimensional projection of parameter domain for the data point that produced the largest $\sigma_{\theta_{\mathrm{CTW}}}$.

5.2.3. Surface current uncertainty

In this section, the estimated standard deviations from the previous sections are propagated into the current estimates. The equations relating the two ship speed vectors to the surface current vector (Equations 1.1 and 1.2) are non-linear. A method to compute how the uncertainty propagates from the ship speed vectors to the surface current vector starts by linearizing the equations using a first-order Taylor series expansion, i.e.,

$$U \approx U_0 + Jx, \tag{5.9}$$

where $U = [U_{\text{along}}, U_{\text{across}}]^T$, $x = [V_{\text{SOG}}, \theta_{\text{COG}}, V_{\text{STW}}, \theta_{\text{CTW}}]^T$, U_0 denotes the evaluation of U at $x = 0$ and J represents the Jacobian matrix given by

$$J = \begin{bmatrix} \cos(\theta_{\text{CTW}} - \theta_{\text{COG}}) & V_{\text{SOG}} \sin(\theta_{\text{CTW}} - \theta_{\text{COG}}) & -1 & -V_{\text{SOG}} \sin(\theta_{\text{CTW}} - \theta_{\text{COG}}) \\ \sin(\theta_{\text{CTW}} - \theta_{\text{COG}}) & -V_{\text{SOG}} \cos(\theta_{\text{CTW}} - \theta_{\text{COG}}) & 0 & V_{\text{SOG}} \cos(\theta_{\text{CTW}} - \theta_{\text{COG}}) \end{bmatrix}. \tag{5.10}$$

The uncertainty in U can now be computed following

$$\Sigma_U = J \Sigma_x J^T, \tag{5.11}$$

where Σ_U and Σ_x denote the covariance matrices of U and x respectively. It will here be assumed that all errors in the two ship speed vectors are independent. In that case, Σ_x reduces to the following diagonal matrix:

$$\Sigma_x = \begin{bmatrix} \sigma^2_{V_{\text{SOG}}} & 0 & 0 & 0 \\ 0 & \sigma^2_{\theta_{\text{COG}}} & 0 & 0 \\ 0 & 0 & \sigma^2_{V_{\text{STW}}} & 0 \\ 0 & 0 & 0 & \sigma^2_{\theta_{\text{CTW}}} \end{bmatrix}. \tag{5.12}$$

The estimated standard deviations from the previous sections can be used to fill the covariance matrix Σ_x. Subsequently, evaluation of Equation 5.11 yields estimates for the uncertainty in the two components of the surface current vector.

The distributions of estimated standard deviations for the surface currents per study area are given in Figure 5.9. In general, the estimated uncertainties are larger in the Strait of Gibraltar study area. The median standard deviations in the along-ship surface currents in the two study areas are $0.13\,\mathrm{m\,s^{-1}}$ and $0.22\,\mathrm{m\,s^{-1}}$ respectively. The median standard deviations in the across-ship surface currents in the two study areas are $0.20\,\mathrm{m\,s^{-1}}$ and $0.30\,\mathrm{m\,s^{-1}}$ respectively.

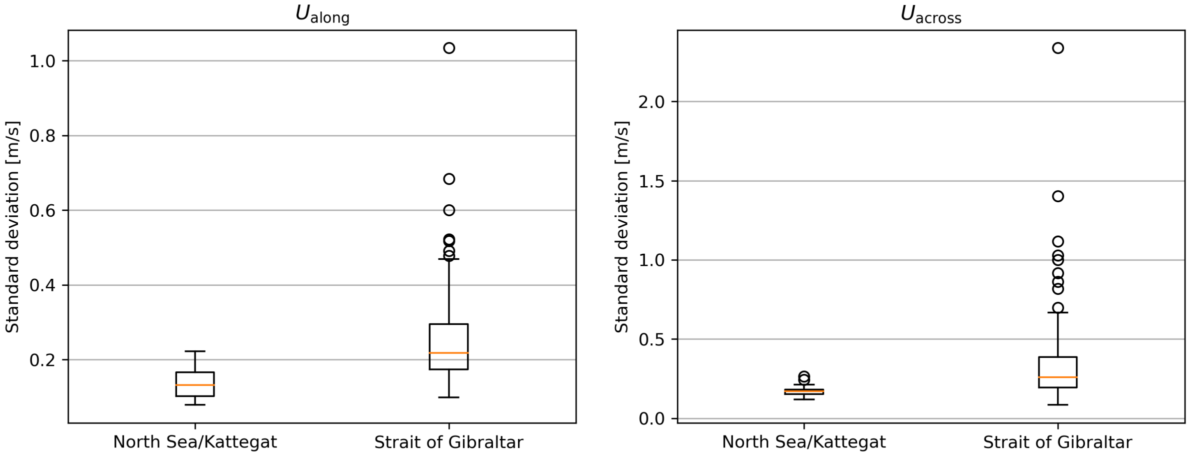

Figure 5.9: Distribution of estimated standard deviations for each of the surface current components.

In Figure 5.10 the estimated standard deviations are compared with the observed error with respect to the HFR dataset. If the estimated standard deviations are accurate, they should be able to predict to some extent the observed errors. Of course, an estimated standard deviation of e.g. $0.20\,\mathrm{m\,s^{-1}}$ does not guarantee an error of $0.20\,\mathrm{m\,s^{-1}}$, even if the HFR data would be perfect. However, on average, larger uncertainties should correspond to larger observed errors.

In Figure 5.10a, no such relationship can be found for the along-ship currents. Therefore, the error method developed in this section is not able to accurately distinguish accurate from inaccurate measurements. In Figure 5.10b it can be seen that for the across-ship currents, larger estimated standard deviations indeed tend to lead to larger observed errors. The factor that the error estimation works better for this component may be explained by the sensitivity of the across-ship currents to small variations in ship course. These variations are quantified by $\sigma_{\theta_{\mathrm{COG}}}$, which is taken into account in the error estimates.

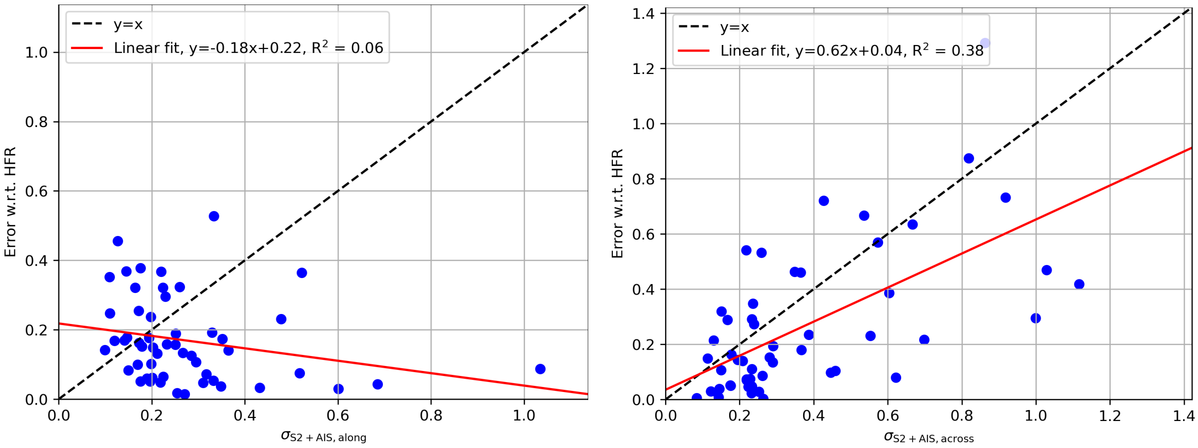

Figure 5.10: Correlations between estimated standard deviations and observed errors with respect to the HFR dataset. The left panel corresponds to along-ship currents, while the right panel corresponds to across-ship currents.

5.3. Triple collocation

In this section, an alternative method to the uncertainty quantification from the previous section is presented. In the Strait of Gibraltar, there were three independent datasets representing the same variable in space and time. For this exact situation, there exists a statistical technique to quantify the uncertainty associated to each individual dataset: Triple Collocation [44] [55] [22]. The method assumes that the three datasets can be represented as noisy linear transformations from the truth, i.e.,

$$y_i^n = \alpha_i + \beta_i x^n + \varepsilon_i, \tag{5.13}$$

where y_i^n represents the nth measurement of dataset i for $i \in \{1,2,3\}$, the α's and β's represent calibration coefficients, x^n denotes the unknown truth and the ε's represent additive Gaussian noise. It can be shown that [22, Eq. 6]

$$\sigma_{\varepsilon_1}^2 = \sigma_1^2 - \frac{\sigma_{12}\sigma_{13}}{\sigma_{23}} = \sigma_1^2(1 - \frac{\rho_{12}\rho_{13}}{\rho_{23}}), \tag{5.14}$$

$$\sigma_{\varepsilon_2}^2 = \sigma_2^2 - \frac{\sigma_{12}\sigma_{23}}{\sigma_{13}} = \sigma_2^2(1 - \frac{\rho_{12}\rho_{23}}{\rho_{13}}), \tag{5.15}$$

$$\sigma_{\varepsilon_3}^2 = \sigma_3^2 - \frac{\sigma_{13}\sigma_{23}}{\sigma_{12}} = \sigma_3^2(1 - \frac{\rho_{13}\rho_{23}}{\rho_{12}}), \tag{5.16}$$

where σ_i^2 is the total variance in dataset i for $i \in \{1,2,3\}$, σ_{ij} is the covariance and ρ_{ij} is the correlation factor between dataset i and j for $i, j \in \{1,2,3\}$ and $i \neq j$. By applying the above equations to the three datasets of along-ship currents in the Strait of Gibraltar, the following standard deviations are found

$$\begin{aligned} \sigma_{\text{S2+AIS,along}} &= 0.14\,\mathrm{m\,s^{-1}}, \\ \sigma_{\text{HFR,along}} &= 0.09\,\mathrm{m\,s^{-1}}, \\ \sigma_{\text{CMEMS,along}} &= 0.23\,\mathrm{m\,s^{-1}}. \end{aligned} \tag{5.17}$$

The standard deviation for the S2+AIS dataset is smaller than the median standard deviation of $0.22\,\mathrm{m\,s^{-1}}$ from the error analysis in the previous section. The standard deviation of the difference between S2+AIS and HFR is given by

$$\sigma_{\text{diff,along}} = \sqrt{\sigma_{\text{S2+AIS,along}}^2 + \sigma_{\text{HFR,along}}^2} \tag{5.18}$$

$$= \sqrt{0.14^2 + 0.09^2} \tag{5.19}$$

$$= 0.16\,\mathrm{m\,s^{-1}}. \tag{5.20}$$

This value is similar to the observed standard deviation between the two datasets of $0.18\,\mathrm{m\,s^{-1}}$ as given in Table 4.1.

For the across-ship currents, the triple collocation is performed before and after filtering for ships with $\sigma_{\theta_{\text{COG}}} < 2°$. Therefore, the first column below presents the resulting uncertainties when all data points are included, while the second column shows the results after filtering.

Table 5.1: Estimated standard deviations for across-ship surface currents before and after filtering for datapoints with $\sigma_{\theta_{COG}}$ < 2°.

Dataset	Standard deviation [$\mathrm{m\,s^{-1}}$]	
	Before filtering	After filtering
S2+AIS	0.30	0.16
HFR	0.16	0.16
CMEMS	0.28	0.29

The median standard deviation of $0.30\,\mathrm{m\,s^{-1}}$ derived in the previous section also took all ships into account. Hence, in this case, the two methods seem to agree on the magnitude of the uncertainty. After filtering, the standard deviation is reduced to $0.16\,\mathrm{m\,s^{-1}}$. This shows that indeed, the quality of the across-ship surface currents is sensitive to variations in ship course. The standard deviation of the difference between S2+AIS and HFR is given by

$$\sigma_{\text{diff,across}} = \sqrt{\sigma^2_{\text{S2+AIS,across}} + \sigma^2_{\text{HFR,across}}} \tag{5.21}$$

$$= \sqrt{0.16^2 + 0.16^2} \tag{5.22}$$

$$= 0.23\,\mathrm{m\,s^{-1}}. \tag{5.23}$$

This value is similar to the observed standard deviation between the two datasets of $0.24\,\mathrm{m\,s^{-1}}$ as given in Table 4.2. Therefore, the Triple Collocation seems to produce reasonable estimates for the uncertainties. The downside of Triple Collocation is that it treats all datasets as being homoscedatic, i.e., it assumes that all measurements within a dataset have the same variance. Therefore, it cannot be used for quality control of individual measurements.

Also note that the sample sizes were only 53 datapoints before filtering and 41 after. In [55] it is estimated that the relative error in the estimated standard deviations is equal to $\sqrt{\frac{5}{N}}$, with N the sample size. For $N = 53$, this yields a relative error of 0.31. Therefore, the estimated standard deviations are still quite uncertain themselves. For a relative error of less than 0.1, a sample size of 500 datapoints would be required.

6

Reflectance model

Even in the absence of cloud cover, a ship's Kelvin wake is not always visible on optical satellite imagery. The visibility of the Kelvin wake will depend on many variables including ship geometry, oceanic and atmospheric conditions, and viewing geometry. In this chapter, the influence of the viewing geometry on the visibility of a Kelvin wake will be assessed. Section 6.1 presents a reflectance model to simulate the expected reflectance of a Kelvin wake. This model is used to reconstruct observed Kelvin wakes in Section 6.2. Thereafter, the reflectance model is used to attempt to predict the optimal ship direction given a fixed viewing geometry in Section 6.3.

6.1. Reflectance model

Optical satellite imagery depends on the reflectance of solar radiation at the Earth's surface. In this section, a reflectance model originally presented in [28] is given. First, it is assumed that direct solar radiation is the only light source. Hence, reflectance of ambient skylight is neglected. Furthermore, it is assumed that the only mechanism of reflection is specular reflection on the water surface. In specular reflection, incoming light is reflected into a single direction, as opposed to diffuse reflection. Moreover, for specular reflection, the angle of reflection is equal to the angle of incidence.

The orientation between the light source, the target object and the imaging platform is here called the viewing geometry. To describe the viewing geometry, four angles are introduced. The zenith angle describes the angular distance between an object and a local vertical line. In Figure 6.1a the definition of the source and receiver zenith angles is visualized. The azimuth angle describes the angular position of an object in the north-south plane. Figure 6.1b visualizes the source and receiver azimuth angles.

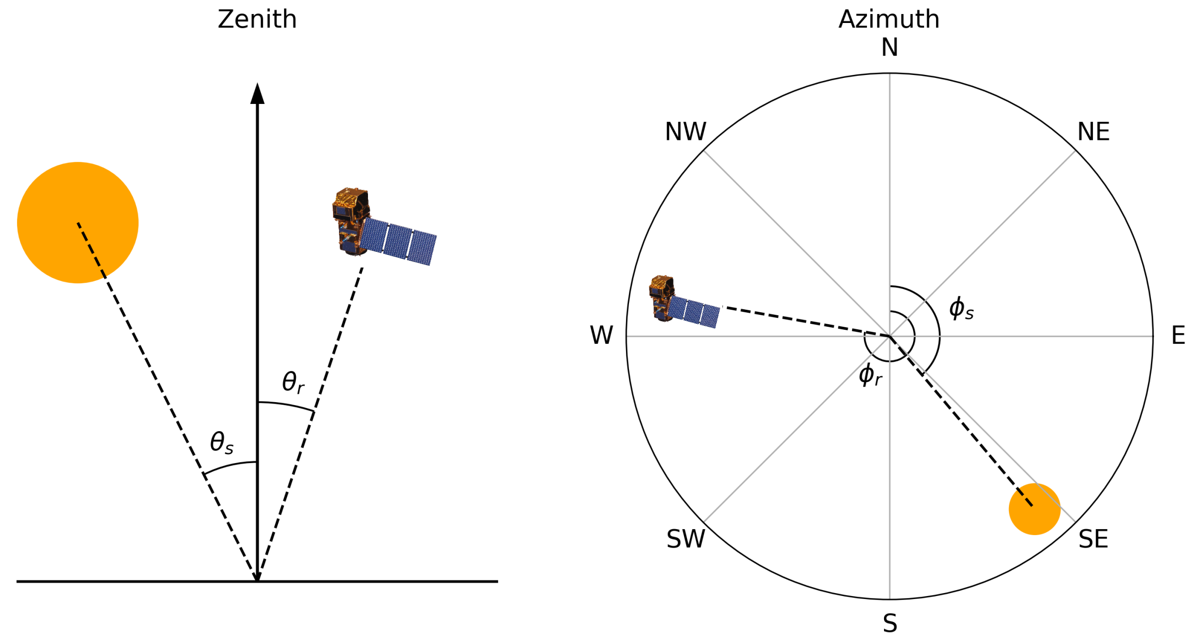

Figure 6.1: a) Definition of source and receiver zenith angles (θ_s, θ_r). b) Definition of source and receiver azimuth angles (ϕ_s, ϕ_r).

In general, the solar and satellite zenith angles will not be equal. Therefore, if the sea surface would be perfectly flat, specular reflection of sunlight would not reach the satellite. However, in reality the sea surface is irregular and adopts a range of surface slopes. The surface slope that is required for direct specular reflection between a source and a receiver can be computed following [52, Eqs. A7, A8]

$$\zeta_{x,\text{specular}} = -\frac{\sin(\theta_s)\cos(\phi_s) + \sin(\theta_r)\cos(\phi_r)}{\cos(\theta_s) + \cos(\theta_r)}, \tag{6.1}$$

$$\zeta_{y,\text{specular}} = -\frac{\sin(\theta_s)\sin(\phi_s) + \sin(\theta_r)\sin(\phi_r)}{\cos(\theta_s) + \cos(\theta_r)}, \tag{6.2}$$

where θ_s and ϕ_s represent the solar zenith and azimuth angles. The receiver zenith and azimuth angles are denoted by θ_r and ϕ_r respectively.

The waves in the Kelvin wake also modify the sea surface slopes. The wave elevations produced in a Kelvin wake are simulated using the spatial model derived in Section 2.3. Subsequently, the x and y derivatives of these simulations are taken to compute the surface slopes generated in the Kelvin wake. These surface slopes will generally not be equal to the required surface slopes for specular reflection. The difference in surface slopes may need to be provided by wind waves. Using superposition of waves, the required surface slopes for the wind waves can be computed as

$$\zeta_{x,\text{wind}} = \zeta_{x,\text{specular}} - \zeta_{x,\text{Kelvin}}, \tag{6.3}$$

$$\zeta_{y,\text{wind}} = \zeta_{y,\text{specular}} - \zeta_{y,\text{Kelvin}}. \tag{6.4}$$

To estimate the probability of a given surface slope, the Cox-Munk model is used. The Cox-Munk model defines a probability density function for the sea surface slopes at a given wind speed. The model is derived from airborne imagery of the sea surface. It is given by [11]

$$p(\zeta_x, \zeta_y, W) = \frac{1}{2\pi\sigma_u\sigma_c} \exp\left[-\frac{1}{2}\left(\frac{\zeta_x^2}{\sigma_u^2} + \frac{\zeta_y^2}{\sigma_c^2}\right)\right], \tag{6.5}$$

$$\sigma_u^2 = 0.00316W, \tag{6.6}$$

$$\sigma_c^2 = 0.00192W, \tag{6.7}$$

where σ_u^2 and σ_c^2 are the variances in the surface slopes ζ_x, ζ_y respectively; and W represents the wind speed.

Given the probability of the required background surface slopes, the expected reflectance of the Kelvin wake can be computed. The reflectance of the sea surface is defined as the ratio between the outgoing and incoming radiation. It can be approximated by [11, Eq. 9]

$$R = \frac{\rho p(\zeta_{x,\text{wind}}, \zeta_{y,\text{wind}}, W) \sec^4(\theta_n)}{4\cos(\theta_r)}, \tag{6.8}$$

where ρ is the Fresnel reflectivity factor at the air-sea interface, and θ_n is the zenith angle of the normal to the surface at which specular reflection occurs. It can be computed using [52, Eq. A5]

$$\tan^2(\theta_n) = \frac{\sin^2(\theta_s) + \sin^2(\theta_r) + 2\sin(\theta_s)\sin(\theta_r)\cos(\phi_s - \phi_r)}{(\cos(\theta_s) + \cos(\theta_r))^2}. \tag{6.9}$$

The Fresnel reflectivity factor is computed following

$$\rho = \frac{1}{2}\left(\rho_s + \rho_p\right), \tag{6.10}$$

$$\rho_s = \left| \frac{n_1\cos(\theta_i) - n_2\cos(\theta_r)}{n_1\cos(\theta_i) + n_2\cos(\theta_r)} \right|^2, \tag{6.11}$$

$$\rho_p = \left| \frac{n_1\cos(\theta_r) - n_2\cos(\theta_i)}{n_1\cos(\theta_r) + n_2\cos(\theta_i)} \right|^2, \tag{6.12}$$

where ρ_s and ρ_p denote the reflectivity factors for p and $s-$polarized light; n_1 is the refractive index of air and n_2 is the refractive index of seawater.

Evaluation of Equation 6.8 at every point in the Kelvin wake now yields a 2-dimensional expected reflectance pattern.

6.2. Reconstruct observed Kelvin wakes

In this section, several observed Kelvin wakes are simulated to assess to what extent the reflectance model can be used to explain observed Kelvin wake visibility patterns. In order to do so, three images of Kelvin wakes were picked as they contained asymmetrical visibility features. These images were rotated to have the ship travel from east-to-west, which matches the ship direction from the forward model. Subsequently, the zenith and azimuth angles of the sun and satellite were extracted from the Sentinel-2 metadata. The solar and receiver azimuth angles were corrected for the image rotation. The wind speed was set at $8\,\mathrm{m\,s^{-1}}$. It was observed that changing the wind speed yielded different magnitudes for the reflectance, however, the general visibility pattern was preserved. Moreover, only the case in which the dominant wind direction was aligned with the sailing line was considered.

In Figure 6.2 the resulting comparisons between observed and simulated Kelvin wakes are shown. In the top two observed figures, the bottom cusp waves are brighter than the top cusp waves. This features is also produced by the model. Similarly, in the bottom figure only the top cusp waves are visible. Although the model does show the bottom cusp waves, they are much less bright. Therefore, it can be concluded that the reflectance model from the previous section is indeed able to explain certain visibility patterns of Kelvin wakes.

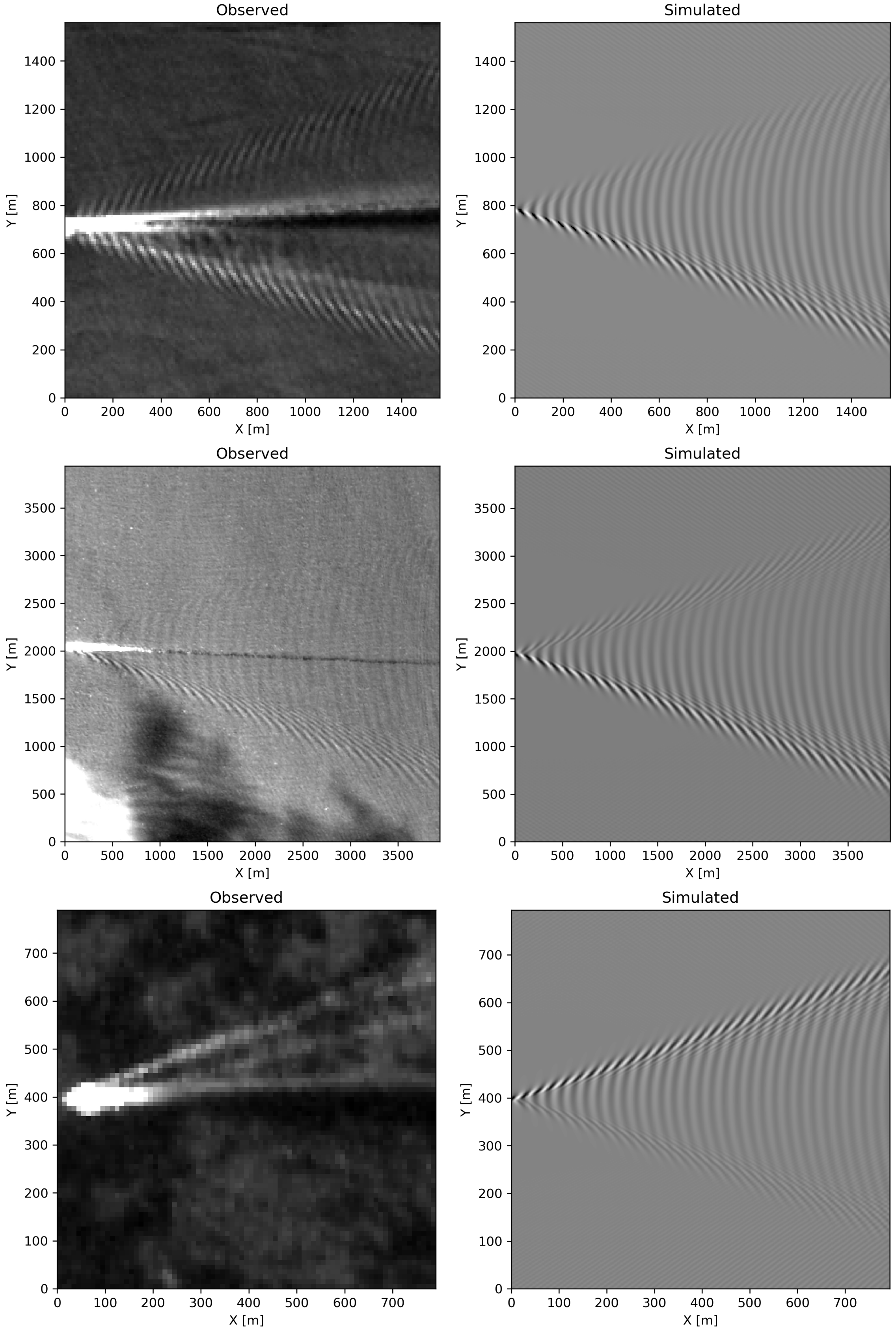

Figure 6.2: Comparison between observed and simulated Kelvin wakes by taking the viewing geometry into account.

6.3. Predict optimal ship direction

In the previous section, it was shown that the viewing geometry explains part of the visibility of a Kelvin wake. Possibly, the ship direction relative to the viewing geometry is a factor that influences whether a Kelvin wake is visible or not. Hence, it is interesting to assess whether an optimal ship direction for a given viewing geometry can be found.

Suppose a viewing geometry is fixed. Then, the reflectance model can be used to compute the average expected reflectance over the Kelvin wake. After performing this for a range of different Kelvin wake orientations, the orientation with the largest average simulated reflectance suggests an optimal ship direction. Subsequently, this predicted optimal ship direction can be compared to the directions of observed Kelvin wake images to assess whether there is a correlation.

The approach above is performed for the study area in the Strait of Gibraltar. All datapoints in the Strait of Gibraltar were located in the same Sentinel-2 tile. However, these tiles were acquired during two different relative orbits. Between the two relative orbits, the viewing geometry is considerably different. Therefore, two viewing geometries were fixed for each of the relative orbits. The solar zenith and azimuth angles are reasonably constant within a tile, however they do vary with the time of the year. Therefore, solar angles were picked to represent the average conditions for the months of July and August over the Strait of Gibraltar. The receiver zenith and azimuth angles also show some variation within a tile. As an approximation, the receiver angles were averaged spatially to find representative values for each relative orbit. The final values for the viewing geometry for the two relative orbits are summarized in Table 6.1.

Table 6.1: Approximate viewing geometry for Sentinel-2 imagery in the Strait of Gibraltar for two different relative orbits. Definition of the four angles is given in Figure 6.1. The sample size of visible Kelvin wakes per relative orbit is given by N.

Relative orbit	$\theta_s [^\circ]$	$\phi_s [^\circ]$	$\theta_r [^\circ]$	$\phi_r [^\circ]$	N
094	25	132	9	104	19
137	25	138	7	278	62

In Figure 6.3 the resulting predicted reflectances for the two viewing geometries are given. The solid black lines represent the average reflectance over the Kelvin wake for a given ship direction. In both cases, ships sailing northwest or southeast are predicted to be most likely to produce a visible Kelvin wake. However, the green dots in both figures indicate the ship directions of the actual observed Kelvin wakes. Clearly, the observed ship directions do not agree with the predicted optimal directions. Therefore, it can be concluded that the reflectance magnitude produced by the model cannot be used to predict visibility of a ship's Kelvin wake.

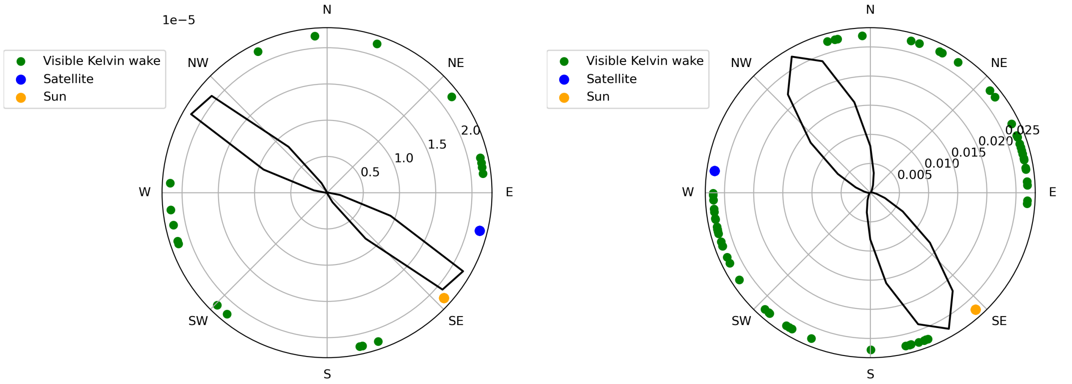

Figure 6.3: Predicted reflectance of Kelvin wakes by ship direction. The left subfigure is computed for Sentinel-2 imagery from relative orbit 094, while the right subfigure represents the viewing geometry from relative orbit 137. The green dots denote the ship directions of actual observed Kelvin wakes. The sample sizes are 19 and 62 datapoints respectively. The blue and orange dots denote the azimuth angles of the satellite and sun respectively.

In Figure 6.4 the distribution of ship courses over the Sentinel-2 tile in the Strait of Gibraltar is given. There, it can be seen that the northwest-southeast direction does have the least amount of traffic. This partially explains why no visible Kelvin wakes were found along that direction. However, the abundance of observed Kelvin wake directions that were orthogonal to the predicted optimal direction indicates that the reflectance model is not sufficiently accurate for predicting favorable ship directions in a given area of interest. Still, the predicted spatial pattern of the reflectance matches observed patterns as shown in the previous section.

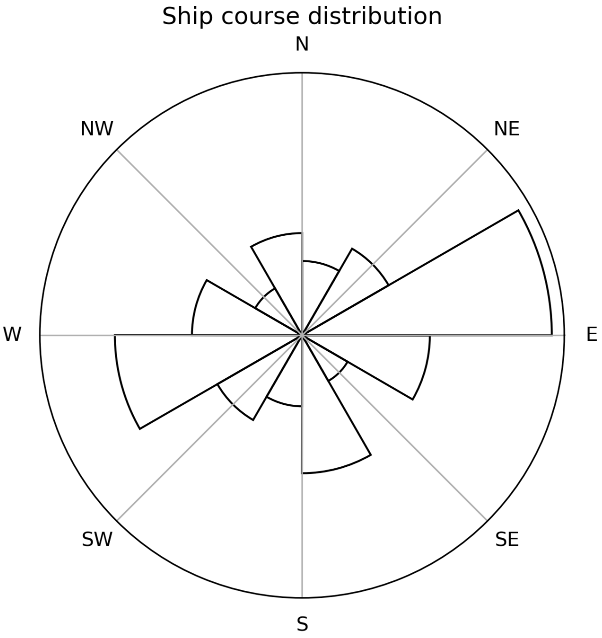

Figure 6.4: Ship course distribution in Strait of Gibraltar derived from AIS samples in July and August 2021.

7

Number of data points

In order to gain insight into the applicability of the estimated surface currents, it is desirable to know how many data points could be expected per unit of time and space. To that end, this chapter presents a rough estimate for the number of data points that could be acquired if all Sentinel-2 imagery over European open waters would be processed. The methodology is given in Section 7.1. The resulting estimate is presented in Section 7.2.

7.1. Methodology

The European open waters were divided into grid cells of $1\,\text{km} \times 1\,\text{km}$. Subsequently, the number of observations was estimated using

$$N_{\text{obs}} = \mathbb{P}_1 \mathbb{P}_2 \sum_{i,j} \mathbb{P}_{3,ij} \rho_{ij} N_{\text{revisit},ij}, \tag{7.1}$$

where

- $\mathbb{P}_1$ denotes the fraction of ships sailing with sufficient speed for them to generate Kelvin waves with a wavelength of more than $20\,\text{m}$,
- $\mathbb{P}_2$ is the probability that the Kelvin wake of a ship with sufficient speed is visible on Sentinel-2 imagery,
- $\mathbb{P}_{3,ij}$ represents the probability of grid cell i, j being cloud-free,
- ρ_{ij} denotes the average instantaneous number of ships in grid cell i, j,
- $N_{\text{revisit},ij}$ is the number of Sentinel-2 images in a year covering grid cell i, j.

The following five sections cover the computational details of the five terms in the equation respectively.

7.1.1. Vessel density

The vessel density, ρ_{ij}, for European waters is obtained from [17]. The dataset provides the average number of monthly ship hours per grid cell in the year 2021, derived from AIS messages. The average number of monthly ship hours per grid cell were converted to the average number of instantaneous ships per grid cell by multiplying each data point with a conversion factor of $12/(365 \cdot 24)$, as proposed in [15]. The spatial resolution is $1\,\text{km} \times 1\,\text{km}$. The dataset is visualized in Figure 7.1. A summation over all grid cells now gives an estimate for the total number of instantaneous ships in European open waters, which yields a value of around $30\,000$ ships.

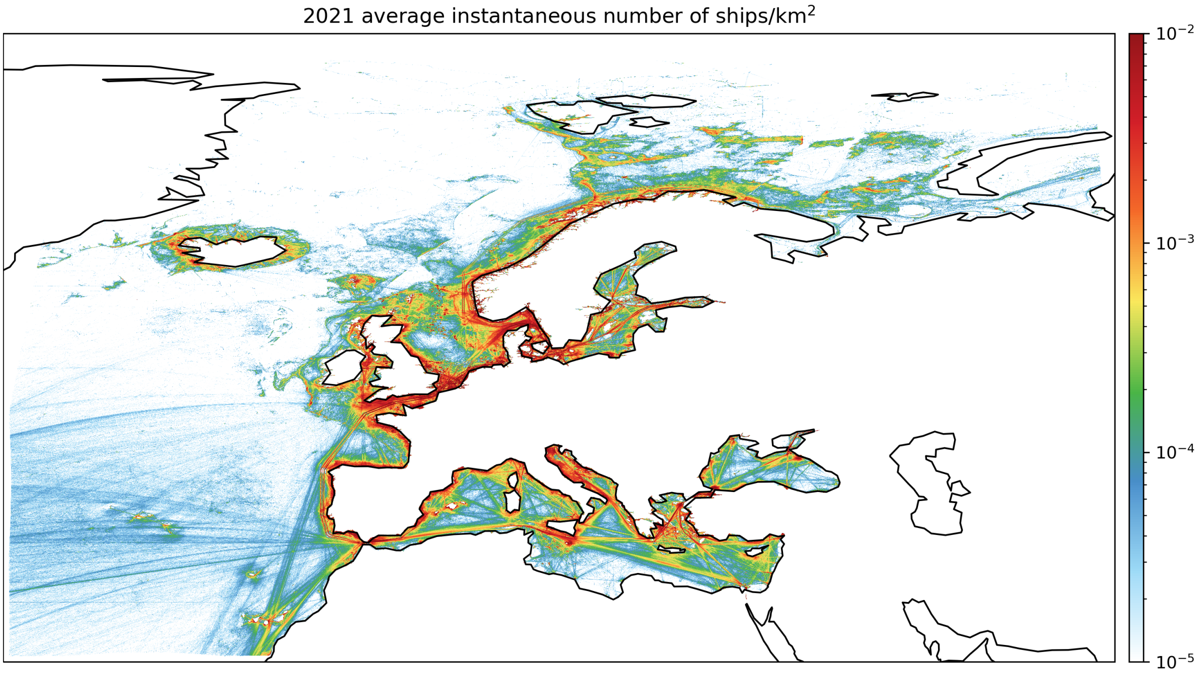

Figure 7.1: Map of average vessel density in European waters in 2021. The spatial resolution is 1×1 km.

7.1.2. Fraction of ships sailing sufficiently fast

Retrieval of a ship's speed from imagery of its Kelvin wake requires the Kelvin waves to be sufficiently long with respect to the spatial resolution of the image. In the case of Sentinel-2 imagery with spatial resolution up to 10 m, the Kelvin waves need to have a wavelength of at least 20 meters to satisfy the Nyquist criterion. The ship's speed through water is related to the the wavelengths in the Kelvin wake following

$$V_{\mathsf{STW}} = \sqrt{\frac{gL}{2\pi}}. \tag{7.2}$$

Plugging in a wavelength $L = 20$ m gives a minimum ship speed through water $V_{\mathsf{STW}} \approx 5.6\,\mathrm{ms}^{-1}$.

The probability that a random ship transmitting AIS messages exceeds this ship speed was estimated by taking samples of AIS messages from the Strait of Gibraltar. Ten samples consisting of $100\,000$ data points each were randomly extracted from the dataset. Subsequently, for each sample the fraction of data points having a V_{SOG} of over $5.6\,\mathrm{ms}^{-1}$ was computed. Thereafter, the average fraction over the 10 samples was taken which resulted in a probability of about 30%, hence $\mathbb{P}_1 = 0.3$. Of course, this value may be inaccurate outside of the Strait of Gibraltar, which would introduce an error in the total estimate.

7.1.3. Probability of visible Kelvin wake

In the previous section, the probability that a random ship is theoretically able to generate sufficiently long Kelvin waves was estimated. However, this does not guarantee the visibility of its Kelvin waves on satellite imagery. This could be due to a variety of factors such as dominating background waves, disadvantageous viewing geometry or unfavourable atmospheric conditions. To account for all these factors, another probability was empirically estimated by looking at two months of AIS data in the Strait of Gibraltar.

First, all ships sailing with a V_{SOG} of over $5.6\,\mathrm{ms}^{-1}$ during a Sentinel-2 overpass were counted. Then, the resulting 405 ships were manually checked on the corresponding imagery to assess the visibility of their Kelvin wakes in the spatial domain. Cloud cover prevented the visibility of 87 of these ships. Out of the remaining 318 ships, 81 had a Kelvin wake that was sufficiently visible for the algorithm to compute a surface current. Hence, the probability of a visible Kelvin wake was $\frac{81}{318} \approx 0.25$, hence $\mathbb{P}_2 = 0.25$. This value is in agreement with figures between 19 and 27% reported by [27]. A flow chart summarizing the counting procedure described above is given in Figure 7.2.

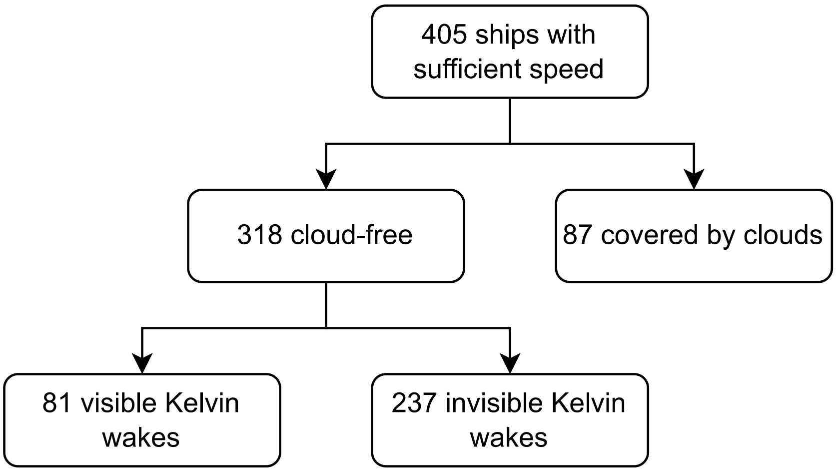

Figure 7.2: Flowchart describing the probability of a visible Kelvin wake for 405 candidate ships corresponding to two months of AIS data in the Strait of Gibraltar.

7.1.4. Cloud cover

Subsequently, the effect of cloud cover was incorporated using data from [49]. The dataset provides an annual mean cloud cover percentage on a near-global grid of 1×1 km, derived from 15 years of Moderate Resolution Imaging Spectroradiometer (MODIS) satellite imagery. The cloud cover dataset was linearly interpolated to the grid of the vessel density dataset. Figure 7.3 shows the interpolated dataset. The white indent over the Atlantic Ocean is due to missing data.

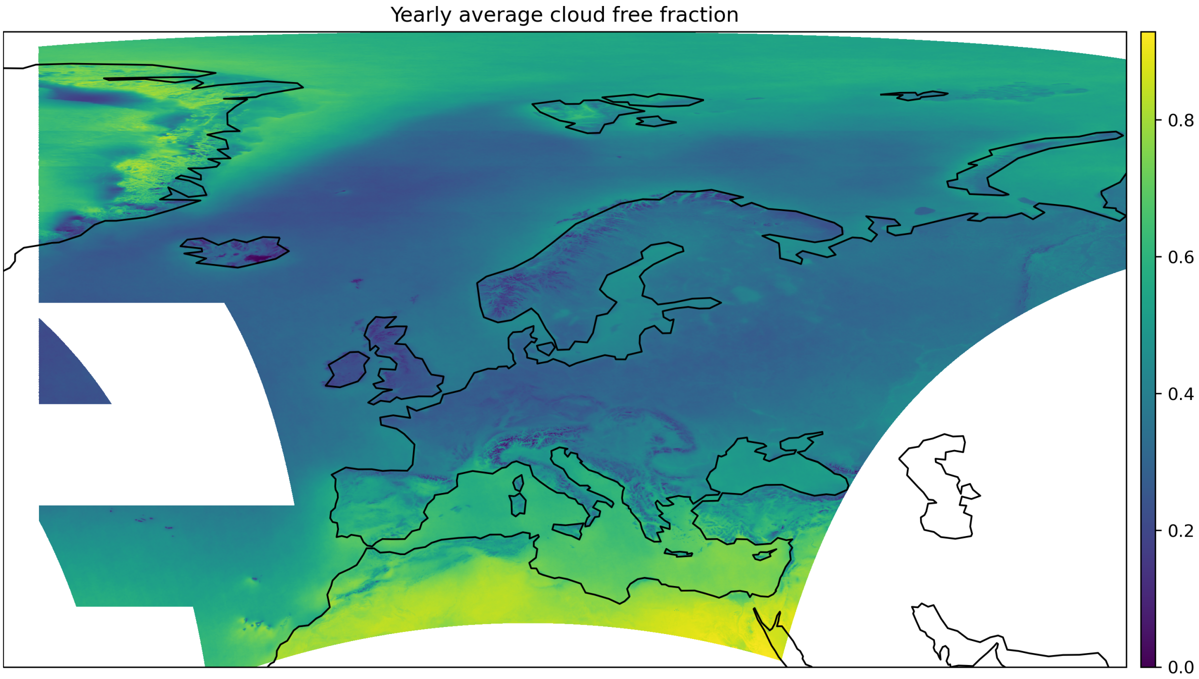

Figure 7.3: Map of yearly average cloud free fraction over Europe. The spatial resolution is 1×1 km.

7.1.5. Revisit times

Finally, the number of images in a year is required. However, Sentinel-2 revisit times differ with geographical location. The vessel density dataset consisted of about 50 million grid cells. It was computationally too expensive to check the number of yearly Sentinel-2 images at each grid point individually. Hence, the vessel density bounding box was divided into $10\,000$ grid cells with equal spacing in longitude and latitude. For each of these grid cells, the number of Sentinel-2 images covering its center point in 2021 was determined by computing the size of the corresponding image collection in the Google Earth Engine. However, as Sentinel-2 tiles may slightly overlap, the center point could be contained in multiple images on the same date. Hence, in order not to overestimate the number of revisit times, the number of unique days in 2021 with a Sentinel-2 image covering the center point was counted instead. Finally, each vessel density grid point was assigned to the revisit time grid cell in which it is contained. The resulting map of Sentinel-2 revisit times in 2021 is shown in Figure 7.4.

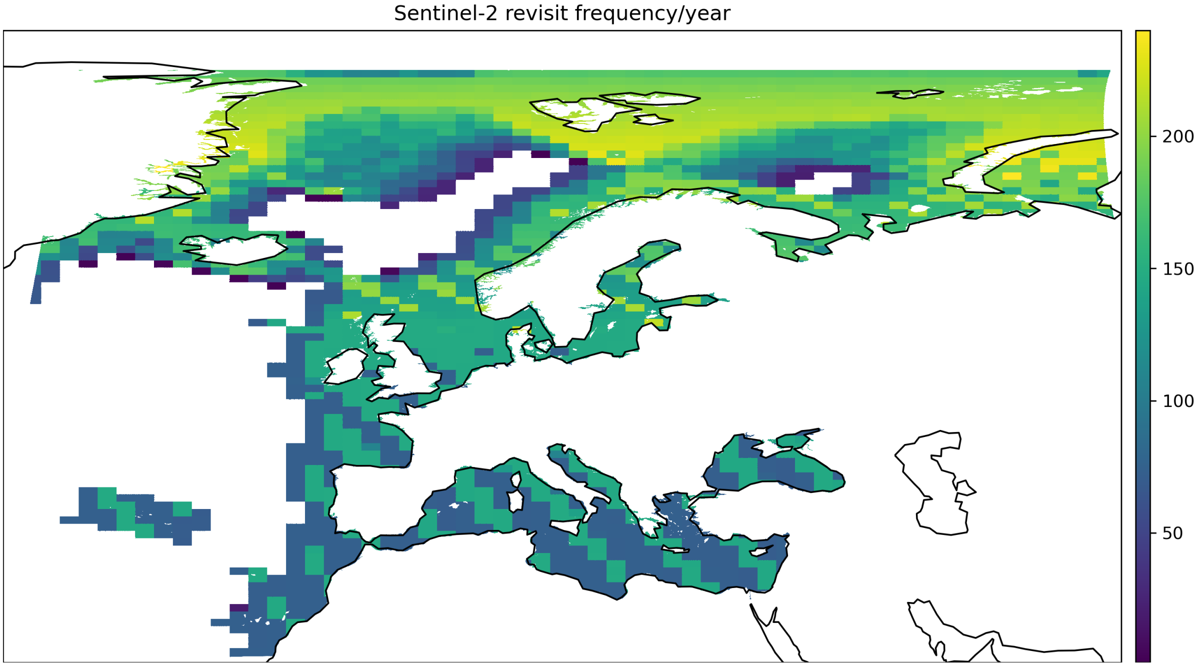

Figure 7.4: Map of Sentinel-2 revisit times over European opean waters in 2021.

7.2. Results

By multiplying each of the factors from the previous sections, an estimate for the number of yearly potential measurements in a grid cell was produced. In Figure 7.5 the spatial distribution of these estimates is shown. A summation over all grid cells yields an estimated $120\,000$ potential measurements in European open water per year.

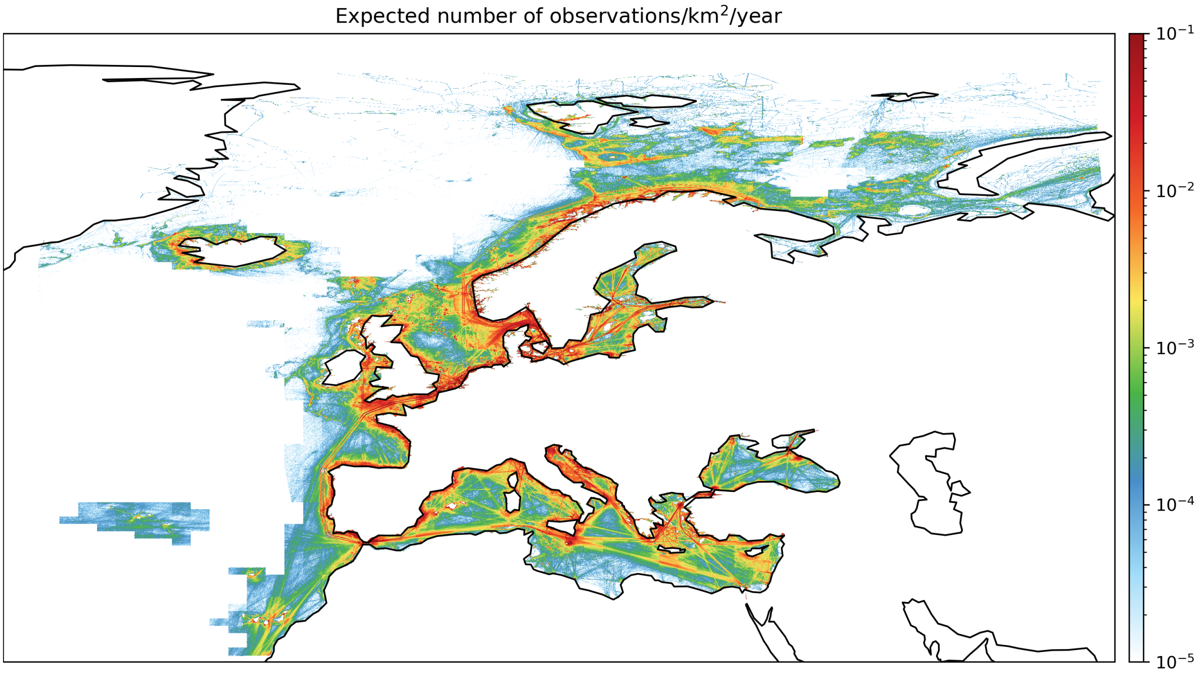

Figure 7.5: Map of estimated number of potential measurements per year over European waters. The total summation yields an estimate of $120\,000$ data points per year.

In order to provide a sanity check of the estimated magnitude, the number of data points extracted from 2 months of AIS data in the Strait of Gibraltar (Figure 7.2) was compared with the predicted figure. In Figure 7.6 the estimated yearly potential number of measurements is shown for the Strait of Gibraltar, with the bounding box roughly corresponding to the Sentinel-2 tile limits. A summation over all grid cells yields an expected 680 data points per year in the Strait of Gibraltar. In the Strait of Gibraltar case study, 81 data points were found for two months of AIS data. Extrapolating this figure to an entire year, a value of 486 measurements per year in the Strait of Gibraltar is found. Hence, the actual number of measurements is smaller than the predicted number of measurements, but both values are in the same order of magnitude. This gives some credibility to the total estimate of $120\,000$ data points over all European waters in a given year. It should be noted that the factors $\mathbb{P}_1$ and $\mathbb{P}_2$ were estimated using AIS data from the Strait of Gibraltar. The estimated values need not be representative for all European open waters.

As a comparison, the Argo float network has accumulated about 2 million velocity measurements at a depth of 1 km over the past twenty years [50]. Hence, the network produces about $100\,000$ velocity measurements per year. Thus, the expected number of observations for Sentinel-2+AIS is on the same order of magnitude. It should be noted that the Argo floats are distributed more homogeneously over the oceans, while the Sentinel-2+AIS measurements are mostly contained in coastal regions. Moreover, Argo floats also provide measurements of other variables such as salinity and temperature. Another comparison for the order of magnitude can be made with the HFRs in the Strait of Gibraltar. During the two months of the case study performed in this thesis, the radars produced about $700\,000$ current measurements. This would amount to roughly 8 million measurements per year, which is considerably more than the Sentinel-2+AIS currents. Still, the number of measurements may be increased significantly if imagery from other satellites, such as SPOT-6/7, WorldView-3/4 or Landsat-8/9 is also used.

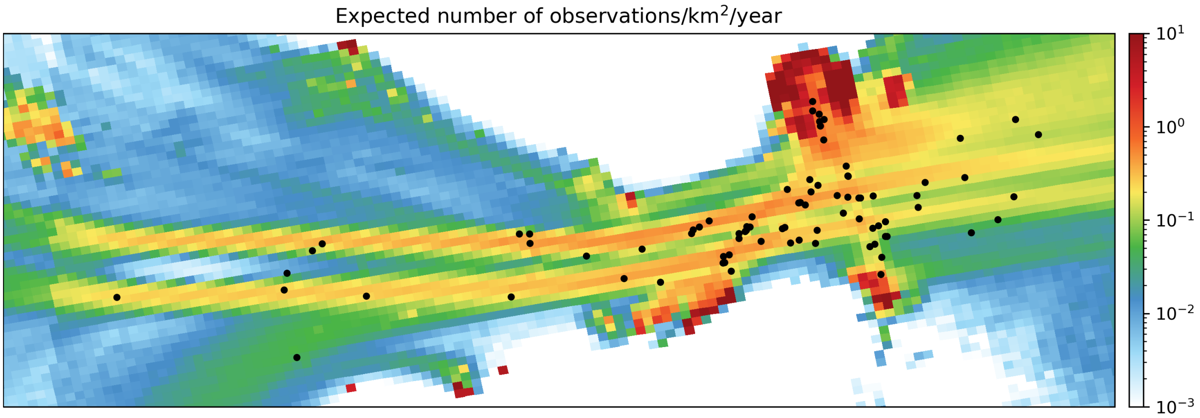

Figure 7.6: Expected number of observations per year for the Strait of Gibraltar. Black dots represent the locations of observed Kelvin wakes acquired in a case study covering two months of Sentinel-2 imagery in this area.

8

Conclusion

This thesis aimed to examine the feasibility of a novel measurement principle to estimate sea surface currents using optical satellite imagery of Kelvin wakes and AIS data. It has been shown that the proposed methodology is successful at estimating surface currents with uncertainties between 0.14 and $0.3\,\mathrm{m\,s^{-1}}$. The across-ship component of the currents was generally less accurate than the along-ship component due to its increased sensitivity to variations in ship course.

The success of the methodology is a consequence of the sharp Kelvin wake signal in the spectral domain, whose shape and location were shown to be insensitive to variations in ship hull geometry. Moreover, it was shown that in many cases, even a partially visible Kelvin wake provided sufficient spectral signal to estimate surface currents. Therefore, provided that a Kelvin wake is visible on imagery, the retrieval algorithm is robust.

In this thesis, only Sentinel-2 imagery was considered. The spatial resolution of Sentinel-2 sets a lower bound on the ship speed through water of approximately $6\,\mathrm{m\,s^{-1}}$. In the Strait of Gibraltar, about 30% of AIS data points exceeded this ship speed. By using higher resolution optical satellite imagery, such as imagery acquired by SPOT-6/7 or WorldView-3/4, the lower bound on the ship speed will be reduced. This may increase the number of Kelvin wakes visible on imagery, although slower-sailing ships generate smaller waves which can in turn reduce the likelihood of Kelvin wake visibility. Moreover, ships in inland waterways also sail at a lower speed. Therefore, higher-resolution imagery may enable the application of the retrieval algorithm to Kelvin wakes in inland waterways. In such shallower waters, it should be noted that the local water depth needs to be taken into account if the depth-to-wavelength ratio decreases below 0.4. This requires an additional data source which may increase uncertainty.

A disadvantage of using optical satellite imagery is that it is hindered by cloud cover. Therefore, the applicability of the developed algorithm also depends on the geographical location of interest. It is potentially interesting to study whether the algorithm can also be successfully applied to Synthetic Aperture Radar (SAR) imagery, since radar waves penetrate clouds. However, this may prove challenging as the speckle noise in SAR imagery hinders the detection of waves on the sea surface. Therefore, the signal-to-noise ratio of the Kelvin wake signal on spectra derived from SAR imagery is likely reduced. Another limitation of the developed methodology is that it depends on AIS data. In general, AIS data is not open access. Therefore, it would have to be acquired from commercial providers which reduces accessibility and potentially increases expenses.

Specular reflection was shown to explain the reflectance pattern of observed Kelvin wakes. However, it was not sufficient to explain whether a Kelvin wake would be visible on satellite imagery. Therefore, a better understanding of the influence of ship geometry, oceanic and atmospheric conditions to Kelvin wake visibility is desired.

Finally, using vessel density and cloud cover data, it was estimated that by applying the algorithm to all Sentinel-2 imagery over European open waters, approximately $120\,000$ measurements could be acquired yearly. This number could be increased by using imagery from multiple satellite missions. Further research is needed to study the spatiotemporal distribution of measurements, which dictates the potential areas of application.

References

[1] European Space Agency. *Sentinel-2 User Handbook*. `https://sentinel.esa.int/documents/247904/685211/sentinel-2_user_handbook`. Accessed: 2022-03-20.

[2] B. Almström, D. Roelvink, and M. Larson. “Predicting ship waves in sheltered waterways – An application of XBeach to the Stockholm Archipelago, Sweden”. In: *Coastal Engineering* 170 (2021), p. 104026. ISSN: 0378-3839. DOI: `https://doi.org/10.1016/j.coastaleng.2021.104026`. URL: `https://www.sciencedirect.com/science/article/pii/S037838392100171X`.

[3] W. Appel. *Mathematics for Physics and Physicists*. Princeton University Press, 2007.

[4] Danish Maritime Authority. *Historical AIS data*. `http://web.ais.dk/aisdata/`. Accessed: 2022-03-20.

[5] F. Bijma, M. Jonker, and A. van der Vaart. *An Introduction To Mathematical Statistics*. Amsterdam University Press, 2017.

[6] Konstantinos Christodoulou, Herodotos Herodotou, and Michalis P. Michaelides. “Estimation of Sea Surface Current Velocities using AIS Data”. In: *2022 23rd IEEE International Conference on Mobile Data Management (MDM)*. 2022, pp. 407–412. DOI: `10.1109/MDM55031.2022.00090`.

[7] E. Clementi et al. “The new Mediterranean Sea analysis and forecasting system including tides: description and validation”. In: *EGU General Assembly 2021* (2021).

[8] CMEMS. *Mediterranean Sea Physics Analysis and Forecast*. `https://doi.org/10.25423/CMCC/MEDSEA_ANALYSISFORECAST_PHY_006_013_EAS7`. Accessed: 2023-02-05.

[9] A.C. Copeland, G. Ravichandran, and M.M. Trivedi. “Localized Radon transform-based detection of ship wakes in SAR images”. In: *IEEE Transactions on Geoscience and Remote Sensing* 33.1 (1995), pp. 35–45. DOI: `10.1109/36.368224`.

[10] *Copernicus Open Access Hub*. `https://scihub.copernicus.eu/dhus/#/home`. Accessed: 2022-03-20.

[11] C. Cox and W. Munk. “Statistics of the sea surface derived from sun glitter”. In: *Journal of Marine Research* 13 (1954), pp. 198–227.

[12] F.S. Crawford. “Elementary derivation of the wake pattern of a boat”. In: *American Journal of Physics* 52 (1984), p. 782.

[13] A. Darmon, M. Benzaquen, and E. Raphaël. “Kelvin wake pattern at large Froude numbers”. In: *Journal of Fluid Mechanics* 783 (2014), R3. DOI: `10.1017/jfm.2013.607`.

[14] *Discrete Fourier Transform*. `https://numpy.org/doc/stable/reference/routines.fft.html`. Accessed: 2022-03-10.

[15] EMODnet. *EU Vessel density map, detailed method*. `https://www.emodnet-humanactivities.eu/documents/Vessel%20density%20maps_method_v1.5.pdf`. Accessed: 2022-08-24.

[16] EMODnet. *Strait of Gibraltar - Radar download*. `https://www.emodnet-physics.eu/Map/platinfo/piradar.aspx?platformid=14199`. Accessed: 2022-03-20.

[17] EMODnet. *Vessel density data*. `https://www.emodnet-humanactivities.eu/view-data.php`. Accessed: 2022-08-24.

[18] G. Gomit et al. “Spectral analysis of ship waves in deep water from accurate measurements of the free surface elevation by optical methods”. In: *Physics of Fluids* 26.12 (2014), p. 122101.

[19] M.D. Graziano, M. D’Errico, and G. Rufino. “Ship heading and velocity analysis by wake detection in SAR images”. In: *Acta Astronautica* 128 (2016), pp. 72–82.

[20] M.D. Graziano, M. D’Errico, and G. Rufino. “Wake Component Detection in X-Band SAR Images for Ship Heading and Velocity Estimation”. In: *Remote Sensing* 8.6 (2016).

[21] Made Smart Group. `https://www.madesmart.nl`. Accessed: 2022-03-20.

[22] A. Gruber et al. "Recent advances in (soil moisture) triple collocation analysis". In: *International Journal of Applied Earth Observation and Geoinformation* 45 (2016), pp. 200–211. DOI: `https://doi.org/10.1016/j.jag.2015.09.002`.

[23] L.H. Holthuijsen. *Waves in oceanic and coastal waters*. Cambridge University Press, 2007.

[24] V. Klemas. "Remote Sensing of Coastal and Ocean Currents: An Overview". In: *Journal of Coastal Research* 28.3 (Apr. 2012), pp. 576–586.

[25] Clément Le Goff et al. "Monitoring the Greater Agulhas Current With AIS Data Information". In: *Journal of Geophysical Research: Oceans* 126.5 (2021), e2021JC017228. DOI: `https://doi.org/10.1029/2021JC017228`.

[26] J. Lighthill. *Waves in fluids*. Cambridge University Press, 1978.

[27] Y. Liu and R. Deng. "Ship Wakes in Optical Images". In: *Journal of Atmospheric and Oceanic Technology* 35.8 (2018), pp. 1633–1648.

[28] Y. Liu, R. Deng, and J. Zhao. "Simulation of Kelvin wakes in optical images of rough sea surface". In: *Applied Ocean Research* 89 (2019), pp. 36–43.

[29] Y. Liu, J. Zhao, and Y. Qin. "A novel technique for ship wake detection from optical images". In: *Remote Sensing of Environment* 258 (2021), p. 112375.

[30] P. López-Dekker et al. "Harmony: an Earth Explorer 10 Mission Candidate to Observe Land, Ice, and Ocean Surface Dynamics". In: (2019), pp. 8381–8384. DOI: `10.1109/IGARSS.2019.8897983`.

[31] P. Lorente et al. "The High-Frequency Coastal Radar Network Operated by Puertos del Estado (Spain): Roadmap to a Fully Operational Implementation". In: *IEEE Journal of Oceanic Engineering* 42.1 (2017), pp. 56–72.

[32] C.L. Luengo Hendriks et al. "The generalized Radon transform: Sampling, accuracy and memory considerations". In: *Pattern Recognition* 38.12 (2005), pp. 2494–2505. ISSN: 0031-3203. DOI: `https://doi.org/10.1016/j.patcog.2005.04.018`. URL: `https://www.sciencedirect.com/science/article/pii/S0031320305002128`.

[33] International Maritime Organization. *AIS transponders*. `https://www.imo.org/en/OurWork/Safety/Pages/AIS.aspx`. Accessed: 2022-03-20.

[34] International Maritime Organization. *Resolution MSC.74(69)*. `https://wwwcdn.imo.org/localresources/en/OurWork/Safety/Documents/AIS/Resolution%20MSC.74(69).pdf`. Accessed: 2022-03-20.

[35] P. Osborne. *The Mercator Projections*. 2013.

[36] K. Oumansour, Y. Wang, and J. Saillard. "Multifrequency SAR observation of a ship wake". In: *IEE Proceedings - Radar, Sonar and Navigation* 143 (4 1996), pp. 275–280.

[37] M. Rabaud and F. Moisy. "Ship wakes: Kelvin or Mach angle?" In: *Physical Review Letters* 110 (21 2013), p. 214503.

[38] E. Raphaël and P.-G. de Gennes. "Capillary gravity waves caused by a moving disturbance: Wave resistance". In: *Phys. Rev. E* 53 (4 1996), pp. 3448–3455. DOI: `10.1103/PhysRevE.53.3448`. URL: `https://link.aps.org/doi/10.1103/PhysRevE.53.3448`.

[39] M.T. Rey et al. "Application Of Radon Transform Techniques To Wake Detection In Seasat-A SAR Images". In: *IEEE Transactions on Geoscience and Remote Sensing* 28.4 (1990), pp. 553–560. DOI: `10.1109/TGRS.1990.572948`.

[40] P.J. Rousseeuw and C. Croux. "Alternatives to the Median Absolute Deviation". In: *Journal of the American Statistical Association* 88.424 (1993), pp. 1273–1283. DOI: `10.1080/01621459.1993.10476408`.

[41] SEOS. *Spectral signatures*. `https://seos-project.eu/classification/images/spectral_signatures.jpg`. Accessed: 2022-03-20.

[42] M. Song et al. "Modeling Kelvin wake imaging mechanism of visible spectral remote sensing". In: *Applied Ocean Research* 113 (2021), p. 102712.

[43] R.M. Sorensen. *Prediction of Vessel-Generated Waves with Reference to Vessels Common to the Upper Mississippi River System*. Tech. rep. Department of Civil and Environmental Engineering, Lehigh University, Dec. 1997.

[44] Ad Stoffelen. “Toward the true near-surface wind speed: Error modeling and calibration using triple collocation”. In: *Journal of Geophysical Research: Oceans* 103.C4 (1998), pp. 7755–7766. DOI: `https://doi.org/10.1029/97JC03180`. eprint: `https://agupubs.onlinelibrary.wiley.com/doi/pdf/10.1029/97JC03180`. URL: `https://agupubs.onlinelibrary.wiley.com/doi/abs/10.1029/97JC03180`.

[45] Y. Sun, P. Liu, and Y. Jin. “Ship Wake Components: Isolation, Reconstruction, and Characteristics Analysis in Spectral, Spatial, and TerraSAR-X Image Domains”. In: *IEEE Transactions on Geoscience and Remote Sensing* 56.7 (2018), pp. 4209–4224. DOI: `10.1109/TGRS.2018.2828833`.

[46] W. Thomson. “On the Waves produced by a Single Impulse in Water of any Depth, or in a Dispersive Medium”. In: *Proceedings of the Royal Society of London* 42 (1887), pp. 80–83.

[47] J.K.E. Tunaley. “The estimation of ship velocity from SAR imagery”. In: *IGARSS 2003. 2003 IEEE International Geoscience and Remote Sensing Symposium. Proceedings (IEEE Cat. No.03CH37477)*. Vol. 1. 2003, pp. 191–193.

[48] G.B. Whitham. *Linear and nonlinear waves*. Wiley, 1999.

[49] A.M. Wilson and W. Jetz. “Remotely Sensed High-Resolution Global Cloud Dynamics for Predicting Ecosystem and Biodiversity Distributions”. In: *PLOS Biology* 14 (3 2016), pp. 1–20.

[50] Annie P. S. Wong et al. “Argo Data 1999–2019: Two Million Temperature-Salinity Profiles and Subsurface Velocity Observations From a Global Array of Profiling Floats”. In: *Frontiers in Marine Science* 7 (2020). ISSN: 2296-7745. DOI: `10.3389/fmars.2020.00700`. URL: `https://www.frontiersin.org/articles/10.3389/fmars.2020.00700`.

[51] Lucas J. Yiew and Allan R. Magee. “Deriving tidal currents from AIS data”. In: *Journal of Physics: Conference Series* 2311.1 (July 2022), p. 012003. DOI: `10.1088/1742-6596/2311/1/012003`. URL: `https://dx.doi.org/10.1088/1742-6596/2311/1/012003`.

[52] C.R. Zeisse. “Radiance of the ocean horizon”. In: *Journal of the Optical Society of America* 12.9 (Sept. 1995), pp. 2022–2030. URL: `https://opg.optica.org/josaa/abstract.cfm?URI=josaa-12-9-2022`.

[53] F. Zijl, M. Verlaan, and H. Gerritsen. “Improved water-level forecasting for the Northwest European Shelf and North Sea through direct modelling of tide, surge and non-linear interaction”. In: *Ocean Dynamics* 63 (2013), pp. 823–847.

[54] G. Zilman, A. Zapolski, and M. Marom. “The speed and beam of a ship from its wake’s SAR images”. In: *IEEE Transactions on Geoscience and Remote Sensing* 42.10 (2004), pp. 2335–2343. DOI: `10.1109/TGRS.2004.833390`.

[55] S. Zwieback et al. “Structural and statistical properties of the collocation technique for error characterization”. In: *Nonlinear Processes in Geophysics* 19 (2012), pp. 69–80. DOI: `https://doi.org/10.5194/npg-19-69-2012`.

A

Derivation frequency shift moving observer

Consider a one-dimensional setting in which two frames of reference are distinguished. First, one with a fixed origin with coordinate x. Second, a frame of reference moving with constant speed V and coordinate $x' = x + Vt$. Let $h(x,t)$ denote the wave height of an arbitrary sinusoid with wavenumber k and angular frequency ω, i.e.,

$$h(x,t) = \text{sin}(kx - \omega t) \tag{A.1}$$

In the second frame of reference, this gives

$$\begin{aligned} h(x',t) &= \text{sin}(kx' - \omega t) && \text{(A.2)}\\ &= \text{sin}(k(x + Vt) - \omega t) && \text{(A.3)}\\ &= \text{sin}(kx - (\omega - Vk)t) && \text{(A.4)}\\ &= \text{sin}(kx - \omega' t). && \text{(A.5)} \end{aligned}$$

Hence, the apparent angular frequency in a frame of reference moving with speed V is given by

$$\omega' = \omega - Vk. \tag{A.6}$$